Mathematical Modeling of Extended Interface During Gravity Drainage With Application to CO_2 Sequestration

by

Farshad Arfaei Malekzadeh

A thesis

presented to the University of Waterloo

in fulfillment of the

thesis requirement for the degree of

Doctor of Philosophy

In

Civil Engineering

Waterloo, Ontario, Canada, 2013

I hereby declare that I am the sole author of this thesis. This is a true copy of the thesis, including any required final revisions, as accepted by my examiners.

I understand that my thesis may be made electronically available to the public.

Abstract:

Removal of CO_2 directly from anthropogenic sources (capture) and its disposal in geological formations can take place for medium-term time periods (storage), or it can be permanent (sequestration), with the CO_2 eventually becoming dissolved in the aqueous phase. The latter is the main subject of this dissertation.

Carbon dioxide sequestration covers a wide range of strategies and alternatives. The main objective of CO_2 sequestration alternatives is secure disposal of carbon in large amounts and for a lengthy time scale (typically 1000 years). Injection of CO_2 into subsurface formations is generally considered as the main option for CO_2 sequestration. Geological sequestration through injection covers a broad variety of target formations: disposal in depleted oil and gas reservoirs, trapping in oil reservoirs, replacing CH_4 in coal bed methane recovery processes, trapping in deep aquifers, and salt cavern placement are the major CCS alternatives in geologic formations.

In this thesis, hydrogeologic interaction between the injectant (CO_2) and the host fluid (saline water) during injection is the main subject of the project. Because of the density and viscosity contrast of displacing and displaced fluids, the pattern of saturation progression is complicated. A set of semi-analytical solutions is developed for quick estimation of the position of isosats (contours of saturation) during primary injection in homogenous cases with simple geometry. All of the mathematical solutions are developed based on two assumptions; incompressible fluids and rocks and vertical equilibrium (capillary-gravity condition) for geometries with large aspect ratio ($L >> H$).

First, a series of analytical solutions for primary drainage for a set of linear relative permeability functions is developed. The first analytical solution is based on the assumption of locally linearized Leverett-J functions, and by using the method of characteristics, a

formulation for the isosats' geometry is obtained. A semi-analytical solution is then proposed for calculation of the position of isosats with linearized relative permeability functions and arbitrary capillary-saturation correlation. The analytical solution is extended to incorporate a specific form of nonlinearity of the relative permeability function. Nonlinear relative permeability functions are also incorporated in another semi-analytical solution, and the positions of the isosats for any arbitrary Leverett-J function and relative permeability functions are developed. Sequential gas-saline injection is also modeled in that chapter.

For approximate verification of the analytical solutions, a FEM numerical model is developed and the results of the analytical solutions are compared with the numerical solutions. These new analytical solutions provide powerful tools for prediction of saturation distribution during injection in vertical and horizontal wells, as well as for carrying out stochastic assessments (Monte Carlo simulations) and parametric weight assessment. The domain of applications of the new solutions go far beyond the limited question of CO2 sequestration: they can be used for injection of any less viscous fluid into a reservoir, whether the fluid is lighter or denser than the host fluid (gas injection, water-alternating gas injection, water injection into viscous oil reservoirs, solvent injection).

Acknowledgments

I would like to thank my supervisors, Professor Maurice B Dusseault and Professor Leo Rothenburg for their patience, guidance and financial support. I would like to thank Terralog Technologies Inc. for financial support of the research project.

I am also grateful of the suggestions of the committee members, Professor Giovanni Cascante, Professor Mario Ioannidis, Professor Yuri Leonenko.

Table of Contents

List of Figures:

List of Tables:

1. Introduction

1.1 CO_2 sequestration:

Anthropogenic carbon dioxide (CO_2) emissions have resulted in a considerable increase of atmospheric carbon dioxide concentration. The major consequence of this abrupt increase is enhancement of the atmospheric greenhouse effect, which consequently leads to an increase in atmospheric temperature. Because of inherent complexity involved with mechanisms of climate change, there is no definite and accepted explanation for the coupling of the carbon cycle and atmospheric temperature, but there is a general agreement that industrial and personal CO_2 emissions are the major source of global warming, and mitigating action is considered by many to be an urgent need.

If the world economies, population and level of technology grow as have been predicted, and also if we include the probable development of cleaner technologies and more efficient energy policies, the concentration of CO_2 will be eventually reach five times what it is now; the concentration may double before 2100 (1). This means that the total accumulation of CO_2 emission from fossil fuel combustion in the next 100 years could be more than 9,000 Gt (1). According to the United Nations Framework Convention on Climate Change, total CO_2 emissions should not exceed 2,600 to 4,600 Gt (1) in order to avoid serious (albeit ill-defined) climate change effects. To decrease significantly the amount of CO_2 emitted, the way energy is produced and consumed should change appreciably.

Global warming happens as a consequence of an increasing concentration of green-house gases in the atmosphere, and CO_2 emissions apparently have the most significant contribution. Carbon dioxide emission may become one of the major constraints on recoverable fossil energy consumption in the future, and Carbon Separation and Sequestration (CCS) is an immediate and potentially viable answer to the problem. It seems

CO_2 sequestration could become a powerful solution as it is capable of reducing the amount of anthropogenic CO_2 emissions to the atmosphere, which was the gist of the commitments undertaken in the Kyoto Protocol signed in 1990 (2).

Carbon Separation and Sequestration is a candidate method to reduce Green House Gases (GHG) effects and stabilize the CO_2 concentration in the atmosphere. CCS targets the CO_2 from flue gases and other point sources, generally the gaseous products of fossil fuel combustion (usually coal). Capturing the CO_2 component in a reasonably pure form, compression and transportation of the CO_2, and finally depositing it in a secure subsurface formation, are the general parts of various CCS systems.

Each of the aspects of CCS technology must be evaluated from technical, economical and environmental points of views. The fate of the injected gaseous mixture in different temporal scales is the major issue of this technical investigation.

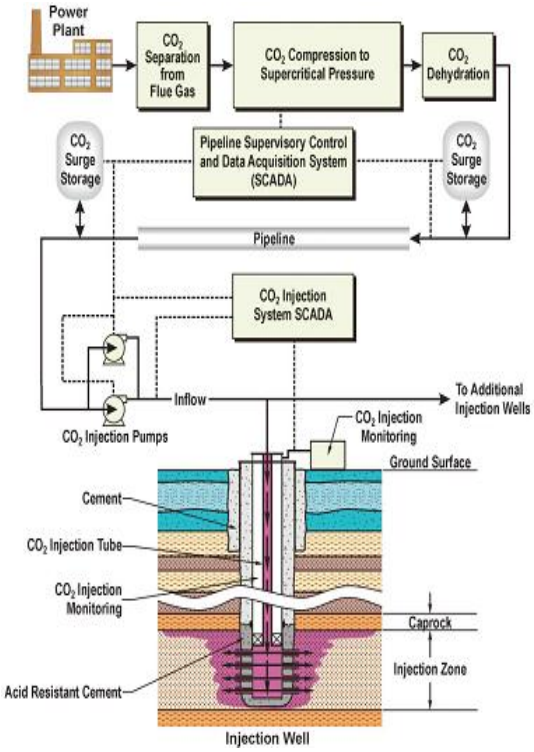

Fig 1-1 Different stages of CCS technology, from capture to injection (Dooley 2006)

1.2 Capture:

Separation of CO_2 from amongst the different components of flue gases and compression of the purified CO_2 is called capture. The technology exists and is applied in several coal and natural power plants. The produced CO_2 has different industrial uses and it is considered as an international commodity, but nowhere near the scale required for any impact on climate change.

Capture of CO_2 is considered as the most expensive part of CCS technology, and purification of carbon dioxide is usually done only at a small scale. Capture technologies must be improved considerably to provide the required amount of pure CO_2 at a reasonable cost for massive sequestration. This part of CCS technology will remain an attractive and rich area of future research for methods that could drive down the cost of capture.

1.3 Transport:

Transportation of purified CO_2 to injection sites is necessary for CCS, and currently little infrastructure exists for this purpose. One of the advantages of CCS technology is generally

close distances between concentrated CO_2 sources and favorable geological formations for sequestration. This fact decreases the transportation length considerably, resulting in significant reduction of operation and maintenance costs. (Fig 1.2)

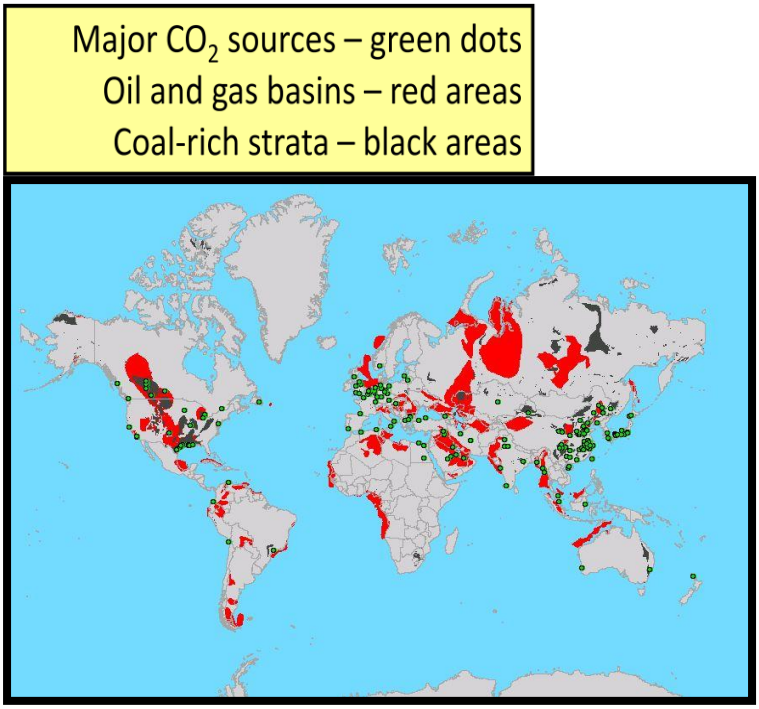

Fig 1-2 distribution of major sources of CO2 emission and Oil and gas basins (IEA GHG)

1.4 Injection in deep geological formations:

Injection in deep geological formations is considered to be the most viable method for massive sequestration of CO_2. Technology for deep injection of gaseous or supercritical components exists in oil and gas industries, although optimization of injection processes by help of horizontal wells, pulsing and smart injection are still considered as subjects for future research.

Several different types of geologic formations are considered as potential candidates for sequestration of CO_2, including saline aquifers, depleted oil and gas reservoirs, and deep unmineable coal seams. Another application of CCS could be to use CO_2 injection as an EOR

(Enhanced Oil Recovery) agent to increase oil recovery from old fields. Coal bed methane replacement and recovery is also another possibility for CO_2 use in coal deposits (3).

Each geologic formation has its inherent capacity, as well as its physical and geographical advantages and disadvantages. An ideal formation for CO_2 sequestration is a permeable formation with high porosity overlain and sealed by impermeable cap rock to prevent any leakage and escape of the disposed CO_2 (in gaseous, supercritical or dissolved form). Volume of reservoir, integrity of cap rock and permeability of the target sediment are considered as the major parameters in the evaluation of formations for injection, and secondary parameters such as depth, thickness, dip and other properties are also important.

Although the contributions of different parts of CCS technology to the final cost depends on many factors and may change with developments, their ratios are roughly similar from one approach to another at the present time, and the most significant portion of the costs is allocated to separation. Purification of flue gas to the required degree to easily generate a supercritical fluid phase has the largest direct influence on the price of pure CO_2. After separation, carbon dioxide is usually compressed to above its supercritical pressure (p_{SC} = 7.39 MPa @ 31.1°C). The density of supercritical CO_2 at the supercritical point (0.469 g/cm^3) is much higher than the density in its gaseous state, but still much lower than the density of the pore fluid in the target host strata (1.05 to 1.2 g/cm^3 for deep saline aquifers).

1.5 Scope of the dissertation:

The approach in this dissertation emphasizes the interfacial interaction of gaseous mixtures (e.g. pure CO_2, or CO_2-enriched flue gas) in saline aqueous liquids for different characteristics of the aquifer, different relative permeability relationships, and different characteristics of the Leverett-J function. These topics have not been sufficiently discussed in the literature to allow them to be fully understood in an integrated (coupled) context for CO_2 sequestration. Reasonable modeling of solubility trapping of the gaseous mixture at high

pressures and temperatures requires a compositional simulator equipped with a realistic EOS (Equation of State for the gas or gas mixtures). The onset of natural convection is a significant factor in determining the rate of the mixing process, and there are different theories describing the initiation of natural convection in liquid-saturated formations (4), (5). The rate of mixing after the onset of density-driven circulation is also a matter of discussion (6). One of the major problems with natural convection is its characteristic time scale, which is too long for any experimental measurement. That makes the verification of the theoretical analysis of natural convection impossible.

Many analytical and numerical solutions are available for simulation of different stages of geologic sequestration of CO_2, and a brief review will be presented in the background section. Because of complexity of processes from different aspects, both numerical and analytical solutions are applicable for the prediction of the fate of injected CO_2 in subsurface formations. Numerical approaches provide a more flexible model for compositional simulations; however, analytical solutions function better in scaled computations and stability analysis, for quick assessments, and for stochastic evaluation and parametric weight determination.

This dissertation will focus on the mathematical simulation of gravitational segregation (override in the case of CO_2 injection) and evolution of the capillary transition zone. The term "gas" is employed throughout; it refers in this thesis to the buoyant phase.

This technical field is extended and complicated, and specification of objectives is important. The following section describes the physical processes during and after injection, and it should be noted that they are interactive and simultaneous. The final target of the injection process is a complete and secure mixing of the injected gaseous mixture for an extended time (e.g. 1000 yr). Each of the processes has its contribution in its own effective timescale.

1.6 Components and outline of the study

The dissertation is organized as follows: Chapter two reviews the relevant literature on geological disposal of CO_2. The Chapter includes the relevant background study of coupled physical phenomena of CO_2 injection in porous media, categorized in three sections: fluid dynamics, thermodynamics and mass transfer. After the background study, another section reviews the CO_2 injection literature, focusing on the gravity-free and gravity drainage (injection) literature.

1.6.1 Semi analytical solutions for linearized relative permeability functions

In Chapters 3 and 4, a series of analytical solution is presented for prediction of the position of isosats (surfaces of equal saturation in a 2-phase fluid system). First a semi-analytical solution is proposed using a linearized Leverett-J function for determining the location of the interface of the transition zone. Afterwards a series of fitting functions are used to approximate the saturation distribution for arbitrary Leverett J functions.

In Chapter 4, a generalized version of the conservation equation is introduced, and the structure of the saturation transition waves is developed for gravity drainage. Afterwards, by forcing the position of isosats to honour the conservation equation, it is shown that the equation can be reduced to a 1-D steady-state case. The solution must also be extended to non-linear relative permeability relationships, which are more realistic.

1.6.2 Semi analytical solutions for non-linear relative permeability functions

Chapter 5 introduces two analytical and semi-analytical solutions for primary drainage in the case of nonlinear relative permeability functions. The analytical solution is only applicable for specific but important cases of nonlinearity, and in this case the dimensionality of the problem is mathematically reducible to 1-D. For generality, a semi-analytical solution is developed using fitting function approximations to estimate the saturation distribution and the

position of isosats. Secondary imbibition is also modeled in Chapter 5, using front tracking methods.

1.6.3 Numerical model

To verify or compare the results of the analytical or semi-analytical solutions, a high resolution FEM model is developed for immiscible two phase flow with fluid density contrast. The numerical discretization is straightforward, and to stabilize the saturation, an upwind weighting method is used. This method is presented in Appendix A.

2 Background and literature review

2.1 Introduction:

During and after injection, there are a number of physical phenomena of interest that will take place in the subsurface. These processes are interactive (coupled) and from a mathematical point of view they are highly nonlinear. In order to give a clear understanding of the phenomena, the relevant physical description has been narrowed down to consider each as a separate process.

Gravitational override and viscous displacement of saline water: during and after injection of a gas (or a lighter liquid or super-critical phase) from a horizontal or vertical well, the gas is less dense than the host liquid; because of the buoyancy effect, the gaseous plume rises vertically and disperses laterally. The eventual configuration of the gas and the liquid pore fluid after great time is as a thin gas cap on the top of the permeable reservoir if none of the gas entered solution (Fig (2.1)).

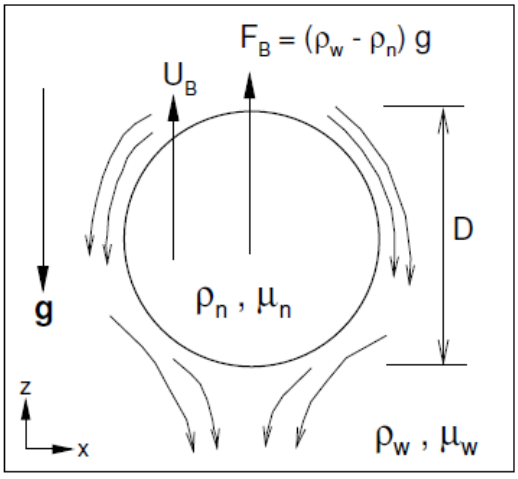

Fig 2-1 Schematic motion of gaseous plume and viscous fluid resulting from a density difference (Riaz 2008)

Evolution of capillary transition zone: During injection of an immiscible non-wetting phase, a non-wetting front invades the pores of the porous medium and drains much of the wetting phase. However, a gas entry pressure is required for invasion of a pore to overcome the capillary forces generated at the interface of the phases. This gas entry pressure is

different for different pores, and the specific value of gas entry pressure in a single pore depends on the size of the pore, the wetting state of the rock (generally wet by the saline host water), and the interfacial tension between the phases. Because of this variability at the pore scale, the drainage front does not remain stable and a transition zone evolves (7), a processes called capillary fingering. Because of the substantially lower viscosity of the injected gas compared to the host saline fluid associated with the buoyancy effect, viscous fingering also develops, and a two-phase transition zone evolves and grows with respect to time. This will be discussed in detail in this thesis.

Evolution of the gas cap: The eventual configuration of a low density immiscible gas/liquid pore fluid is the generation of a thin gas/liquid cap on the top of reservoir.

Capillary trail: A limited portion of the CO_2 is trapped in the trail of the mobile CO_2 front. In this formation, residual gas remains behind as discontinuous bodies of gas, and the equilibrium between buoyancy and capillary forces stabilizes the configuration (Fig (2.2)) once the viscous driving forces dissipate.

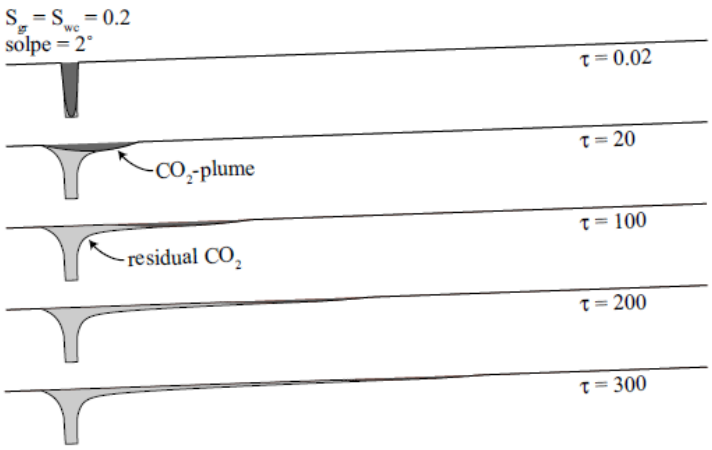

Fig 2-2 Evolution of gas cap and residual trapping zone (Riaz 2006)

Dissolution: Because of local thermodynamic equilibrium across the two sides of the phases' interface, there will be an imposed concentration of different components on the liquid side of the boundary. The imposed concentration gradient triggers a mass transfer from the gaseous to the aqueous phase: the CO_2 becomes dissolved in the water, eventually reaching an equilibrium level, perhaps at the maximum saturation value for the conditions. Within the saline water phase, CO2 in dissolved state can diffuse outward in the direction of the concentration gradient (non-advectively driven diffusive mixing is an extremely slow process in porous media).

Natural convection: after partial mixing of CO_2 and the host saline water, the CO_2-rich saline aqueous phase becomes denser than the original saline aqueous phase, and when the density difference becomes sufficient over an appropriate length, gravitational instability ensues, and dense fingers move downward, with less dense fingers of the saline water moving upward. This phenomenon is called natural (density-driven) convection and it tends to accelerate mixing by increasing the surface area, ameliorating the rate of mass transfer into the saline water, and bring new aqueous phase material into contact with the overlying CO_2 phase.

Several of these physical phenomena happen simultaneously, and they are coupled. These processes have different time scales, and their time scales are closely dependent on the characteristics of the reservoir and the constitutive relationships that govern flux processes in the specific porous medium. In particular, important aspects include the porosity and absolute permeability of the formation, the relative permeability and the Leverett-J functions of the media, as well as the injection specifications (rate, T, composition) and the phase state behavior and dissolution behavior of the fluids. Time scale seems to be the most important factor in CCS technology, and is closely related to the rate of injection that can be achieved and the characteristics of the porous medium. CCS technology will be practical if it is

capable of secure disposal of millions of tonnes of CO_2 in a reasonable time period, but if the formation fails to accommodate a reasonable amount of CO_2 in a requisite time, the CCS system will not be efficient.

These processes are complicated and rigorous mathematical simulation of them is accordingly complex as well. It should be noted here that in such a complex system, developing of analytical solutions requires that the effects of many second-order phenomena be neglected, including the heat effect (heat of mixing and heat of expansion of injected gas) and geochemical effects (e.g. altering pH and potential dissolution or precipitation of minerals). Furthermore, to make the problem tractable in this research project, factors such as anisotropy and heterogeneity of formations, etc., are ignored or simplified.

This research will be dedicated to mathematical modeling of innovative injection methods, with special emphasis on those that lead to accelerated solubility trapping (solubility trapping is inherently more secure than supercritical fluid placement). These topics include gaseous mixture injection (e.g. enriched flue gas instead of purified CO_2), natural convection prediction and rate of mixing during the dynamic circulation within the host saline aquifer.

2.2 Problem Statement:

It is apparent that physical modeling of each component of the process is complicated, and extends into different branches of computational physics. Hydrodynamics of liquid and gas in a subsurface porous media (5), (4), thermodynamics of dissolution, and mixing of the gaseous components in a host liquid and its interaction with regional fluid flow have been the subject of several investigations (8).

Because of the buoyancy effect, the less dense injectant eventually migrates to the top of the aquifer. After evolution of the gas cap on top of the aquifer, even if it is overlain by cap rock formations, the interface is not stationary: dissolution continues and convection is initiated.

Natural convection is considered as an important part of the mixing process, simply because it accelerates the mixing process. The mechanism for natural convection is simple; small amounts of CO_2 dissolve into the saline aqueous phase and increasing concentration of CO_2 changes the density of the liquid. If this density difference exceeds a certain limit, gravitational instability occurs (9), (5). The mechanism is similar to density-driven instability of an impulsively heated lower boundary of a stationary fluid (10), such as the convective flux observed in a pot of water being heated.

Immobile CO_2 trapping in a capillary trail is another method of sequestration. Residual micro-trapping is considered to be capable of isolating the gaseous mixture for geologic timescales, based on equilibrium between the buoyancy forces and capillary forces. This area is interesting for research and will likely remain an area of intense CCS research for the future.

Injection of a gaseous mixture (CO_2 and N_2) instead of pure CO_2 and simulation of the rates of components' mass transfer is another objective of this research. The EOS for real gas behavior at high pressures and high temperatures and its solubility in the saline aqueous phase should be studied as well.

The onset of natural convection because of induced density gradients is another important subject that should be studied. Both linear and nonlinear stability analyses based on a variety of analytical and numerical methods exist for internal and external gravitational instability. The density gradient limit that triggers the instability and the rate of mixing after onset of the instability for different boundary conditions are also objectives for detailed study.

Generally a multiphase multicomponent model for simulation of gaseous injection in saline aquifers is required for better understanding and predicting. The model should be capable of modeling fluid flow and thermodynamics of dissolution and diffusion. Numerical modeling

of some of these processes is expensive (time-consuming), therefore analytical and semi-analytical models are very important as well (11). Such models can allow rapid examination of simple cases, integration into higher-order models (as kernel functions for example), and development of a good conceptual appreciation of the physical processes. The analytical solutions have important practical applications. First, they can be used for partial verification of numerical formulations for this class of problems. Second, because a solution at any time is obtained instantly, they are useful for a "quick look" at different scenarios. Third, because there is no time-stepping involved, the solutions can be used for long time period estimations where numerical dispersion may arise in numerical formulations. Fourth, these solutions may be used in probabilistic evaluations (e.g. Monte Carlo simulations) and risk analyses which might involve thousands of realizations, an impractical task with numerical simulators. Finally, this solution may be used as the basis for other mathematical or numerical developments where additional physical aspects are added (e.g. dissolution, capillarity…) or non-linearities introduced, either analytically or semi-analytically. Practical applications of solutions such as these presented herein include injection of gas, light hydrocarbon liquids, or supercritical CO_2 into saline aquifers, and even the injection of low viscosity dense phases such as water into an oil reservoir or chlorinated hydrocarbon leakage into an aquifer.

2.3 Trapping mechanisms:

As introduced above, there are several physical trapping mechanisms, and each of them functions in a characteristic time scale and provides a different level of security. CO_2 can be disposed in depleted oil and gas reservoir by stratigraphic and structural trapping mechanisms, in oil reservoirs and aqueous formations by solubility trapping, in unmineable coal beds by adsorption trapping, and in salt cavern by simple immobilization (12).

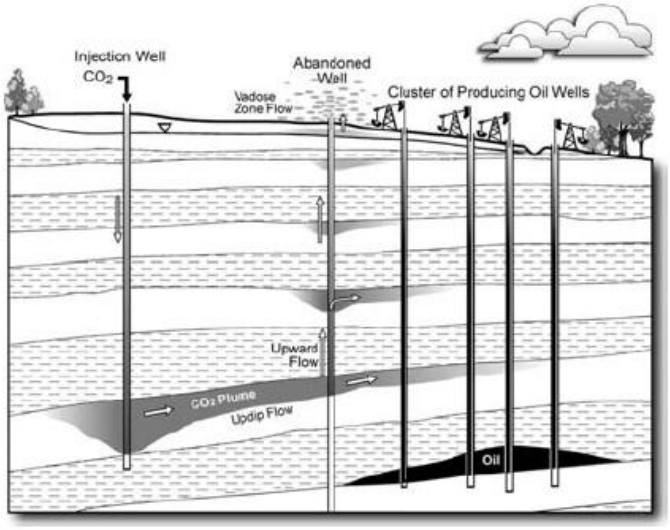

Fig 2-3 Different alternatives for CO2 sequestration (Flett 2004)

Fig (2.4) represents a comparison between contributions of different physical mechanisms in total trapping. It is apparent that the least secure method, structural and stratigraphic trapping of supercritical CO_2, has the greatest potential contribution in the short term. Conversely, as the level of security goes higher for different mechanisms with longer effective time scales, the engineering potential of these processes is less clear. The following is a brief introduction to the different trapping mechanisms and their advantages and disadvantages.

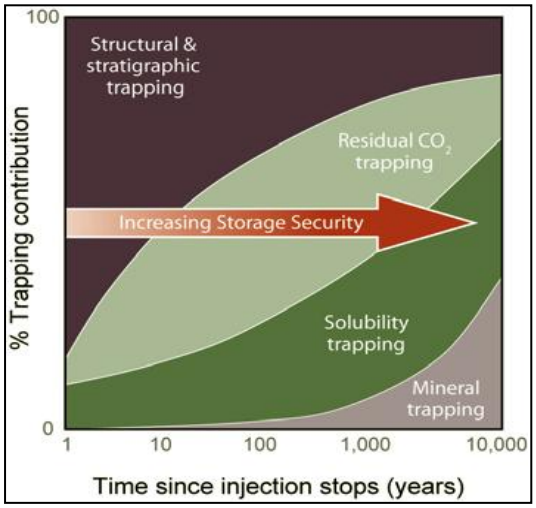

Fig 2-4 Contribution of trapping mechanism (Benson 2008)

2.3.1 Structural trapping mechanism:

The injected CO_2 both in supercritical and gaseous form has a significant lower density than the host saline liquid. Because of the buoyancy effect, gaseous or supercritical CO_2 plumes can migrate upward directly or laterally up-dip. Trapping of CO_2 under an impermeable layer that is geometrically sealed (e.g. an anticline) or fault sealed is called structural trapping. This trapping could be in a closed non-migrating system or one may also envision an open but very slowly migrating system (hydrodynamic trapping) (13).

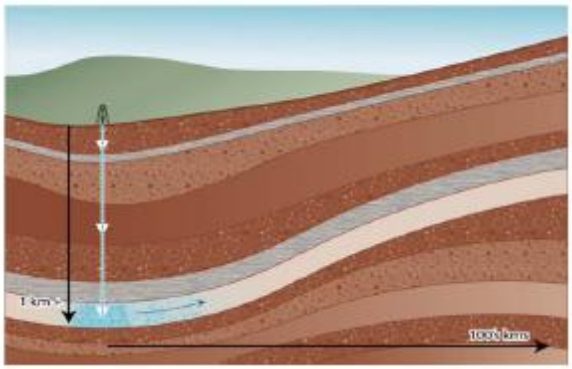

Fig 2-5 Structural trapping mechanism (Dooley 2006)

Advantages of this trapping mechanism are its large contribution at small time scales. Cap rock integrity is very critical in this mechanism, and this factor should be considered carefully. The mechanism of cap rock closure is based on its high capillary force due to the fine porous structure of the rock (small diameter pore throats).

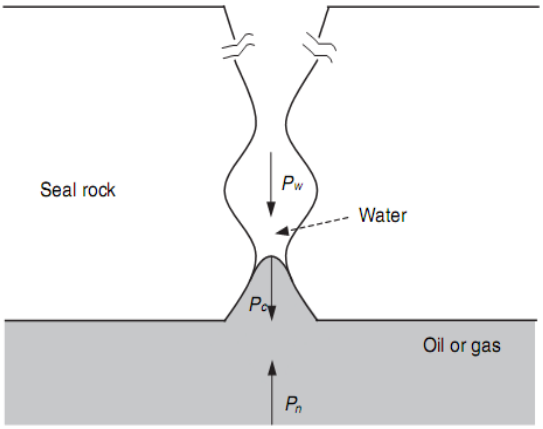

Fig 2-6 Sealing mechanism of cap rock (Plug and Bruining 2007)

The generated pressure in the subsurface may control the capacity of the structural trapping mechanism. In the other words if the pressure exceeds the cap rock capacity, leakage will take place and the sealing mechanism fails to isolate the stored fluid. This is a major constraint for the mechanism, and limits the storage capacity and injection rate. If the CO_2 is stored as a supercritical fluid under typical conditions (ρ = 0.6 – 0.8 g/cm^3), there is the additional problem of miscibility of water and CO_2, therefore the integrity of a capillary seal is further drawn into question over long time scales.

2.3.2 Residual (capillary) trapping mechanism:

A separated fraction of CO2 distributed through the porous medium in a stable configuration comprises another trapping mechanism. Because of separated fractions of gaseous mixture, there is no significant permanent excess pore pressure being generated as a result of injection (11). Therefore the capacity of this mechanism is not limited by the integrity of the cap rock with respect to buoyancy forces.

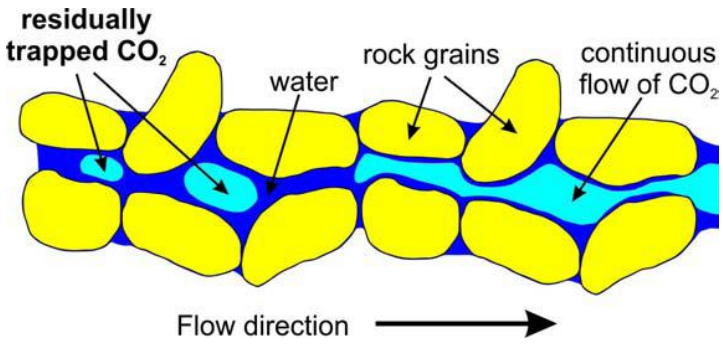

Fig 2-7 Capillary trapping (Dooley 2006)

Residual trapping is considered as an effective trapping mechanism, but thorough understanding of the physical mechanism demands pore scale investigations of media because of possible anisotropy and nonhomogenity. Long term geochemical effects, wettablity alteration and natural groundwater flow can connect the separated fractions and mobilize them if their connected height becomes great enough so that the buoyancy forces exceed the capillary forces. Perhaps the greatest issue is the limits on volume stored that can be achieved by capillary residual trapping in the gaseous form; it is not likely to be of sufficient magnitude.

2.3.3 Solubility trapping mechanism:

Dissolution of CO_2 into in-place saline water or hydrocarbon liquids is supposed to be the most secure trapping mechanism other than precipitation of a solid, CO_2-rich mineral phase (11). Dissolved CO_2 becomes isolated, immobile and non-reactive for a long period of time and there is no rise of pressure as the result of dissolution happening in the formation. The main problem with this trapping mechanism is its slow rate to achieve a fully CO_2-saturated liquid, and the limited capacity of the mechanism in terms of volume stored (~8% by mass CO_2 can dissolve into water at 15 MPa and 40°C).

Careful investigation of solubility-based mixing of gaseous mixtures and pore fluid requires a comprehensive knowledge of fluid flow hydrodynamics including dispersion and convection (6), thermodynamics of dissolution and diffusion (8) and finally possible geomechanical

effects. The main concepts are presented briefly in the following section. This main target of this project is clarification, scale estimation, simulation and generally feasibility assessment of this trapping mechanism in a porous formation.

2.3.4 Mineralization:

Geochemical binding of CO_2 to the rock is considered the most secure trapping method, although this method is not considered effective in most of the investigations because of the lengthy time-scale (14).

Beside the aforementioned trapping mechanisms, there are other alternatives like hydration (12), temporary disposal (storage) of CO_2 in salt caverns (15), ocean sequestration (16), etc.

In the two following sections, the required basis for these two processes is introduced, including the assumptions involved, the temporal and spatial scale issues, the approach to formulation, and solution strategies.

2.4 Background Study:

2.4.1 Fluid Mechanics:

Examining the principles of fluid flow in porous media, including single phase and multiphase flow, mass and heat transfer, and so on, it is apparent that typical treatments do not have the scientific depth that is required for the applications to be considered. Based on the application and nature of the physical phenomena, certain assumptions suffice for some cases but not for others. Spatial and temporal scales are used for single- and double-continuum treatments, and scales depend on the mean velocity, the pressure gradient, the permeability, and also the field representative length (Table 2.1).

There are three different scales for description of fluid flow in a porous medium; the molecular scale (scale at which the molecular diffusion is occurring), the pore scale (wherein continuum equations are valid), and finally the Darcy scale (hundreds to thousands of pores

forming a representative elementary volume – REV – within which Darcy's law is valid) (17). One might also consider a megascale where effects of heterogeneity, anisotropy, and geological stratification are introduced.

Table 2-1 Different temporal and spatial scales for porous media (Kaviany 1999)

BRINKMAN SCREENING DISTANCE	PORE SIZE (OR PARTICLE SIZE)	REPRESENTATIVE ELEMENTARY VOLUME	LINEAR DIMENSION OF SYSTEM
LENGTH SCALES			
$K^{1/2}$	d	ℓ	L
$K^{1/2} \ll d$	$d < \ell$	$\ell \ll L$	
$10^{-12} - 10^{-3}$ m	$10^{-10} - 10^{-2}$ m	$10^{-8} - 1$ m	$10^{-6} - 10^{2}$ m
TIME SCALES			
$K^{1/2}$	d	ℓ	L
0	$\frac{d^2}{\alpha_e}$, $10^{-15} - 10$ s	$\frac{\ell^2}{\alpha_e}$, $10^{-11} - 10^{5}$ s	$\frac{L^2}{\alpha_e}$, $10^{-7} - 10^{7}$ s
$\frac{K^{1/2}}{u_0}$†, $0 - 10^{3}$ s	$\frac{d}{u_0}$, $0 - 10^{4}$ s	$\frac{\ell}{u_0}$, $10^{-3} - 10^{6}$ s	$\frac{L}{u_0}$, $10^{-1} - 10^{8}$ s

However, in most of the approaches, when averaged macro formulation of molecular mass transfer is sufficient, only pore and Darcy scales are studied. There are many approaches towards the modeling of dispersion and fluid flow in porous media for both one phase and multiphase cases.

Here, we are limited to creeping flow with negligible effect of inertial force (no dynamic effects). For low Reynolds numbers, Darcy's law is considered as a base for the other formulations in one and two phases, and also for coupling of flow problems with geomechanics issues. In contrast to other governing physical equations like the conservation equations (mass, momentum, energy), Darcy's law is empirical and it is not considered necessary to invoke any strong physical proof of its validity. This is because the valid scale of the dimensions for Darcy's law (Darcy scale) is much larger than the scale at which

continuum mechanics is valid (the pore scale), and up-scaling is not easy due to unstructured and irregular pores (hence the REV concept).

The main concept of upscaling is developing a mathematical scheme which is capable of capturing the physics at the fine scale and providing some simple governing equation for large scale description of the spatial domain. These mathematical methods are usually based on some assumptions which simplify the physics of porous media, and it is important that these assumptions be shown to be robust for the processes considered.

The scientific literature is rich in articles on mathematical up-scaling from the pore to the macro scale, and most of them are based on mathematical averaging in random or periodic media. Ene and Sanchez-Palencia used the theory of homogenization for seepage flow in rigid porous media (18). They assumed the macro scale domain as a series of identical periodic cells of grain and fluid in a micro scale and used an asymptotic approximation for micro-scale continuum-based momentum conservation and derived macro-scale permeability coefficients. This method was used by Mei and Lee for derivation of permeability and dispersivity of a solute in a periodic porous medium (19).

The theory of homogenization for two phase flow has been used for multiphase flow but to a much less degree than the theories that were considered in the previous configuration (20). Defining a cell problem in micro scale appears not to be tractable for spatial variations of saturations, and up-scaling based on cell formulations are not considered to be physically applicable to this case.

2.4.1.1 Multiphase flow:

Seepage phenomena involving multiphase fluids within a framework of continuum mechanics is based on the local averages of variables. The scale of averaging should not be

much larger than the pore scale but not less than it either (21). Similarly, the results of the continuum-based simulations are not contrasted in scale smaller than pore scale.

The principal descriptive parameters of two-phase immiscible fluids in porous media are usually saturations and velocities of each fluid, but pressure-based approaches are possible (22). These characteristic approaches are equivalent, based on one-to-one mapping of saturation, capillary pressure and relative permeabilities (23).

Velocity of the fluids is a vector characteristic equal to the averaged velocity of the phase in the particular spatial coordination. Based on the continuum mechanics approach, the velocity field and saturation field are continuous inside one phase domain. The boundaries between phases are combination of several curved segment areas with radii of curvature comparable to the characteristic pore diameter. The curved interfaces stabilized by surface tension lead to a jump in the pressure across the interface, which is described by the capillary phenomena equation given by the Laplace formula:

$$p_c = \alpha\left(\frac{1}{R_1}+\frac{1}{R_2}\right) \tag{2.1}$$

Here, R_1 and R_2 are the mean curvature of the interface and α is the interfacial tension. R_1 and R_2 are on the order of $\left(k/\varphi\right)^{1/2}$, where k is the permeability and m is the porosity of the porous formation (21). For instance in a sandstone with typical permeability of 0.1 μm^2 and porosity of 0.1 - 0.2, characteristic pore size diameter is 5-10 μm. Interfacial tension for water and carbon dioxide is 27 mN/m (24)(25). Consequently, the capillary pressure at the boundary is on order of tens of kPa. This significant capillary pressure becomes very important in residual trapping and will be discussed later.

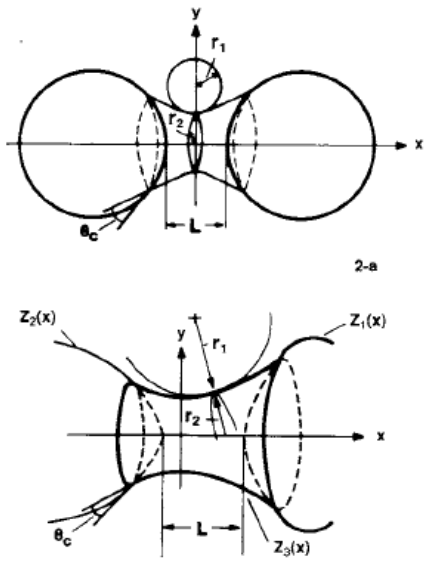

Fig 2-8 Capillary configuration (Kaviany 1999)

Capillary pressure can be measured from a core sample, and it depends on the interfacial tension between the wetting and non-wetting phases and the wettablity (contact angle) of the mineral phases. In order to write the capillary pressure only as a function of saturation and contact angle, and ignore the effect of random structure of pore channels, the Leverett function is proposed in Eq (2.2) (21). This formulation is based on an analogy of randomly shaped capillaries with circular cylindrical shapes.

$$p_c = \alpha\left(\frac{\varphi}{K}\right)^{1/2} \cos\theta\, J(S) \tag{2.2}$$

For a mobile continuous phase, pressure is defined as the average of its value in a Representative Elementary Volume (REV).

Water-rich and gas-rich zones are separated by a transition area, and the length of this transition area may vary from the pore scale (abrupt interface) to hundreds of meters (26).

2.4.1.1.1 Hydrostatic equilibrium of two phase flow:

In the static condition, there is no inertial effect and all the phases are in mechanical equilibrium. For two fluids with different densities, gravitational and capillary forces are present and must enter the general statement of equilibrium. The vertical gradient of each fluid's pressure is equal to the unit weight of the fluid, and consequently the gradient of capillary pressure is equal to the difference of the densities of the phases.

$$\frac{dp_1}{dz} = -\rho_1 g;\ \frac{dp_2}{dz} = -\rho_2 g \tag{2.3}$$

$$\frac{d(p_2 - p_1)}{dz} = \frac{dp_c}{dz} = (\rho_1 - \rho_2)g = \gamma_1 - \gamma_2 \tag{2.4}$$

There are many correlations between capillary pressure and relative saturation in the literature, extending from unsaturated soils work to oil-water production applications in the petroleum industry. Schematically, the variation of saturation versus capillary pressure is shown in Figure (2.10). There are two important parameters in the figure; the first is the residual saturation, and the second is the different drainage and imbibition fluid retention curves. The residual saturation is the saturation of the immobile fractions of the wetting phase in the pore space, and is also called irreducible saturation. This saturation occurs at an infinite capillary pressure for the wetting phase and at a zero capillary pressure for the non-wetting phase. This value is critical for estimation of residual trapping mechanism capacity in CO_2 sequestration, quantification of the volume of immobile oil ganglia in reservoirs subjected to water flooding, and in remediation analyses for contaminant removal from underground water aquifers.

Similar to Figure (2.11), the effect of hysteresis is important in the water retention curve, and it represents different curves for drainage (dewatering) and imbibition (increasing water

saturation). This subject will be discussed in the next section. Vertical equilibrium is a key assumption in the developed solutions for primary drainage problems, and it has been justified several times.

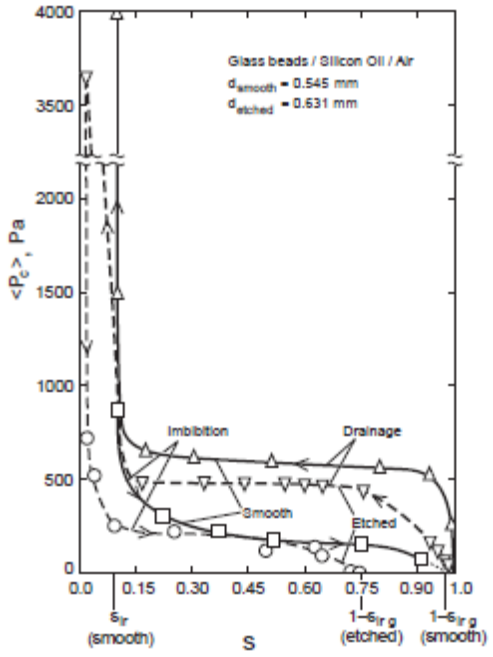

Fig 2-9 Capillary and saturation correlation (Kaviany 1999)

2.4.1.1.2 Motion of two-phase flow in porous media:

A quasi-static assumption is usually made for physical interpretation of saturation variation and flow in multiphase porous media; this involves only slow pushing aside of a displacing fluid with no inertial effects. Static equilibrium is assumed to be valid, and this assumption for rapid variation of saturation is not reasonable (21). Effects of inertial and drag forces are usually ignored in this assumption, but the dominant forces, which are viscous, gravitational and capillary forces, are all considered.

The effect of saturation hysteresis on relative permeability is similarly described, and it has a different path for imbibition and drainage. The slight differences are explained by the existence of this hysteresis which arises because of inherent geometrical complexities of the

pore structure. One of the pore scale complexities is variation of pore channel diameter in a capillary "channel", combined with the fact that imbibition occurs as displacement of a contiguous wetting phase. However, during drainage, a trail of immobile fractions of the wetting phase is left behind. Therefore in a capillary pressure relationship, the saturation of the wetting phase after drainage is higher than it is after imbibition (21).

Fig (2.10) presents the variation of relative permeability versus saturation. Table (2.2) is a collection of correlations between saturation and relative permeabilities. Rigorous calculation of relative permeabilities through the process is important, especially in gravity drainage or gravitational override of a gaseous plume.

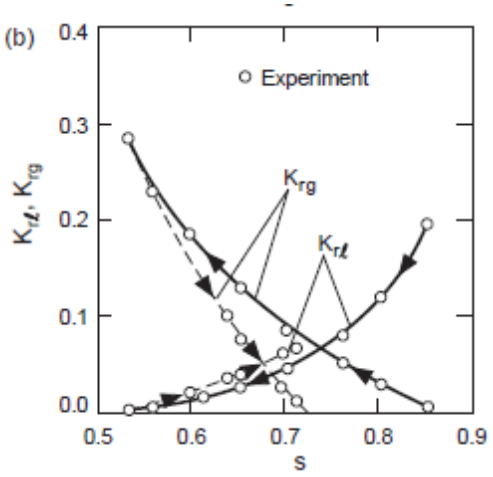

Fig 2-10 relative permeability versus saturation (Kaviany 1999)

There are several instability mechanisms involved in multiphase flow, especially when the wetting and non-wetting phases are much different in density and viscosity. Significant difference in viscosities causes evolution of viscous fingering, and channeling also occurs as a consequence of heterogeneity and anisotropy. Consequently, the actual distribution of saturation will be totally different from that predicted the Darcy equations alone (27).

Rigorous modeling of viscous fingering, gravitational segregation, channeling, formation of isolated ganglia and other instabilities requires a pore-scale approach to capture small-scale perturbations and local propagation of instabilities.

Table 2-1 Different correlations for relative permeabilities

Porous Media	Correlation
Sandstone and lime stone (oil water) (23)	$K_{rl}=S^4$, $K_{rg}=(1-S^2)(1-S^2)$
Nonconsolidated sand (well sorted) (28)	$K_{rl}=S^3$, $K_{rg}=(1-S)^3$
Nonconsolidated sand (poorly sorted) (29)	$K_{rl}=S^{3.5}$, $K_{rg}=(1-S^2)(1-S^{1.5})$
Cemented sandstone, limestone, rocks (28)	$K_{rl}=S^4$, $K_{rg}=(1-S^2)(1-S^2)$
Sandstone, oil-water (30)	$K_{rl}=S^3$, $K_{rg}=1-1.11S$
Soil-water-gas (31)	$K_{rl}=(1-S_r-S_{rg}-S)^{1/2}\{(1-S^{1/m})^m-[(1-(1-S_r-S_{rg}-S)^{1/m}]^m\}^2$ Parameter m comes from experiments
Consolidated sandstone (Saline-CO_2) (32)	$K_{rl}=S_e^{\alpha}$, $K_{rg}=\beta(1-S_e)^{\alpha}$ Parameters α and β come from experiments

2.4.1.1.3 Mathematical formulation of multiphase flow:

In this section, we introduce the governing formulation of laminar two-phase fluid flow in porous media. The most straightforward form of the governing equation is parabolic. The main unknowns are pressures of the wetting and non-wetting phases. Saturation of wetting phase and relative permeabilities are considered functions of capillary pressure

$$S_w = S_w(P_c) = S_w(P_g - P_w) \tag{2.5}$$

S_w is the reverse correlation between capillary pressure and saturation, which exists only if saturation decreases with capillary pressure monotonically, which can be the case for a monotonic injection process (i.e. no reversal in flow direction).

$$\begin{cases} q_w = \dfrac{k_{rw}\rho_w}{\mu_w} k(\nabla p_w + \gamma_w \tilde{e}_z) \\ q_n = \dfrac{k_{rn}\rho_n}{\mu_n} k(\nabla p_n + \gamma_n \tilde{e}_z) \end{cases} \tag{2.6}$$

In these relationships, q is mass flow (volume flow), k_{rn} is relative permeability of the nonwetting phase, and μ is viscosity. Mass conservation for both phases is expressed as

$$\begin{cases} \nabla.(q_w) = \nabla.(\lambda_w(\nabla p_w + \gamma_w \tilde{e}_z)) = \dfrac{\partial \rho_w S_{(p_c)}}{\partial t} \\ \nabla.(q_n) = \nabla.(\lambda_n(\nabla p_n + \gamma_n \tilde{e}_z)) = -\dfrac{\partial \rho_n S_{(p_c)}}{\partial t} \end{cases} \tag{2.7}$$

$$\lambda_w = \frac{k_{rw}\rho_w}{\mu_w}, \quad \lambda_n = \frac{k_{rn}\rho_n}{\mu_n} \tag{2.8}$$

Equations are the base equations of the method called the "simultaneous solution method" in the petroleum literature. The equations are coupled and nonlinear and reduce to zero capillary pressure for single-phase flow.

Equations in parabolic form can be written based on different unknowns (33), but the most simple one is the classical Muskat equation for multiphase flow (34), if the two phases are considered incompressible and with zero capillary pressure.

$$\begin{cases} \nabla.\left[\left(\lambda_n+\lambda_w\right)\left(\nabla p+\gamma\nabla z\right)\right]=q_n+q_w \\ \nabla.\left[\lambda_n\left(\nabla p+\gamma\nabla z\right)\right]=-\varphi\dfrac{\partial S}{\partial t}+q_n \end{cases} \tag{2.9}$$

A hyperbolic form of flow equation is more applicable in CO_2 sequestration application because it is well-suited to the Riemann equation formulation (35). This form of equation was first used by Fayers and Sheldon (36), and if one neglects the effect of capillary pressure, this equation reduces to the equation from Buckley-Leverett theory (37). If we assume the fluids are incompressible, which is reasonable for deep injection of CO_2 (little Δp and ΔT), one can write

$$-\nabla\cdot u_w=\phi\frac{\partial}{\partial t}\left(S_w\right)+q_w \tag{2.10}$$

$$\nabla\cdot u_n=\phi\frac{\partial}{\partial t}\left(S_w\right)+q_n \tag{2.11}$$

Here, u_n and u_w are volumetric velocities of fluid phases, and q_n and q_w are volumetric sources of wetting and non-wetting phases.

$$\nabla\cdot u_t=-\left(q_w+q_n\right)=-q_T \tag{2.12}$$

$$u_l=-\lambda_l\left(\nabla p_l-\gamma_l\nabla z\right) \qquad \lambda_l=\frac{kk_{rl}}{\mu_l} \quad l=w,n \tag{2.13}$$

The symbol λ is called the mobility of phase l, and u_t is the total flow. Water velocity can then be written as

$$u_w=mu_n+\lambda_w\left(\nabla p_c+\Delta\gamma\nabla z\right) \tag{2.14}$$

Here, M is called the mobility ratio and defined as $m=\frac{\lambda_w}{\lambda_n}$ and $\Delta\gamma_{=}\gamma_w-\gamma_n$

$$u_n=\frac{1}{1+m}\left[u_T-\lambda_w\left(\nabla p_c+\Delta\gamma\nabla z\right)\right] \tag{2.15}$$

If Eq (2.14) is substituted into Eq (2.16), one can obtain

$$\nabla \cdot \left[f_n u_T - \bar{\lambda} \left(\nabla p_c + \Delta\gamma \nabla z \right) \right] = \phi \frac{\partial S_w}{\partial t} - q_n \tag{2.16}$$

Where f_n and f_w are the fractional flows of wetting and non-wetting phases.

$$f_n = \frac{\lambda_n}{\lambda_n + \lambda_w} \qquad f_w = \frac{\lambda_w}{\lambda_n + \lambda_w} \tag{2.17}$$

$$\bar{\lambda} = \frac{\lambda_n \lambda_w}{\lambda_n + \lambda_w} \tag{2.18}$$

Eq (2.16) is still a parabolic representation of two-phase porous media flow, but if any variation of capillary pressure is neglected, the equation becomes a hyperbolic type equation.

Application of injection of a gaseous mixture into a saline aquifer is reduced to two important one-dimensional flows. The gravity-driven vertical rise of a gaseous plume, associated with the downward viscous movement of the host saline water, is reduced to a case of 1D multiphase countercurrent flow. This application is important for estimation of gravitational override time scaling.

$$u_w + u_n = 0 \tag{2.19}$$

By substituting equation Eq. (2.11) in Eq. (2.9)

$$\frac{\partial(\phi s)}{\partial t} = -\frac{\partial}{\partial z}\left(\bar{\lambda} \left(\frac{\partial p_{c(s)}}{\partial z} + \Delta\gamma \right) \right) \tag{2.20}$$

And by substituting the Leverett equation for capillary pressure

$$\frac{\partial s}{\partial t} = -\frac{\partial}{\partial z}\left(\bar{\lambda}_{(s)}\left(J'(s)\frac{\partial s}{\partial z} + \Delta\gamma \right)\right) \tag{2.21}$$

The equation has two terms on the right side, a capillary term and a gravitational term. Silin *et al.* (35) proposed asymptotic analytical solutions for different scales of $\frac{\bar{\lambda}}{\Delta\gamma}\acute{J}_{(s)}$.

If $\left|\frac{\bar{\lambda}}{\Delta\gamma}\acute{J}_{(s)}\right| \gg 1$ the flow can be characterized by Ryzhike's self-similar solution (38). This represents an abrupt change in saturation, for instance flow of a gaseous plume against impermeable cap rock. The second case is $\left|\frac{\bar{\lambda}}{\Delta\gamma}\acute{J}_{(s)}\right| \sim 1$ which is the case where both capillary and gravitational force are important, which suits the case of thick and permeable aquifers. Finally for the case of a negligible saturation gradient, $\left|\frac{\bar{\lambda}}{\Delta\gamma}\acute{J}_{(s)}\right| \ll 1$, the equation reduces to the Buckley-Leverett approximation.

$$\phi\frac{\partial(s)}{\partial t} = -\frac{\partial}{\partial z}\left(\bar{\lambda}_{(s)}\Delta\gamma\right) \tag{2.22}$$

This turns out to be similar to the Riemann equation with shock and rarefaction waves. The other important application of a 1D assumption is lateral dispersion of injected CO_2 in a confined reservoir. This type of formulation has been addressed in several investigations, and the solutions are based on the assumption that all flux is horizontal, so the sets of equation reduce to a 1D equation.

$$\frac{b(r,t)}{B} = \frac{1}{\lambda_n - \lambda_w}\left[\sqrt{\frac{\lambda_n\lambda_w V_{(t)}}{\varphi\pi B r^2}} - \lambda_w\right] \tag{2.23}$$

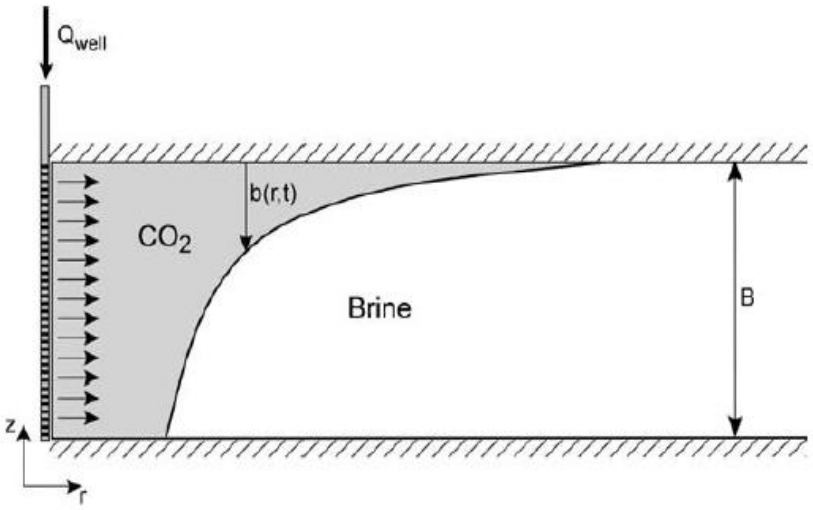

Fig 2-8 Lateral dispersion of CO2 during injection process (Nordabotten, Celia and Bachu 2005)

In this equation, $V_{(t)}$ is the total volume of injected CO_2 which is a function of time, B is the zone thickness, and λ_n and λ_w are mobility coefficients for the wetting and non-wetting fluids. After injection of CO_2 there are two transient propagations which start simultaneously, first pressure propagation and second, displacement of the CO_2 front. The first one is propagation of the outer boundary condition for pressure distribution, and the second one is leakage velocity of the CO_2 front away from the injection well. It has been shown that both of the propagation processes are proportional to $\sqrt{t}$. (39)

2.4.2 Drainage-Injection process with application of CO_2 injection:

Theoretical solutions for multiphase flow problems in the presence of viscosity and density contrasts have been a subject of much research for many decades. The specific application that is interesting for this thesis is the CO_2 injection process, and the physical process can be simulated by injection of a light non-wetting fluid into a single-phase saturated medium, where the non-wetting phase is (CO2) and the aqueous wetting phase (saline water) fluids are partially soluble but immiscible (40). This physical phenomenon is called primary drainage. Here, mathematical treatments for the primary drainage process are presented in the two major categories; gravity-free drainage and gravity drainage (41).

In the special case when wetting and non-wetting fluids have equal densities and vertical gravity head is zero (i.e. velocities are only horizontal) the drainage process can be (42) modeled by a 1D flow equation. This problem is called the gravity-free drainage process and possible application of such equations are EOR methods using injection of a solvent with densities close to oil density (e.g. water flooding), or attempts to water-flood heated heavy oil where the densities are almost equal. In the Eq (2.21), the generalized formulation of gravity free drainage was presented.

However, when the displacing and the displaced fluids have a significant density difference, gravity forces becomes important and must be coupled with the viscous forces. The combination of the effective forces results in a complicated saturation distribution. Gravity drainage is defined as vertical displacement of the wetting phase by the non-wetting phase of different density. There are numerous applications for gravity drainage applications including air sparging (42), acid gas injection (43), CO2 sequestration, geothermal energy extraction and a number of different oil recovery schemes such as steam-assisted gravity drainage, vapor-assisted gravity drainage, and water flooding of conventional oil of lower density in a partially oil-wet reservoir.

The governing equations for saturation conservation in a homogeneous porous medium are well established (44). By rearranging the equations, they can be decoupled into two equations for saturation and pressure where the equation for the saturation distribution is convective-diffusive, but the convective component is generally dominant. The convective term comes from the velocity of the fluid imposed by the rate of injection, and the diffusion coefficient is then proportional to the capillary pressure. By assuming a small capillary number, the saturation equation is reduced to a hyperbolic (convective) equation ((21)). Several analytical solutions of the governing equations for symmetric geometries and linearized conditions have been published (45), (46)(47)(48).

2.4.2.1 Gravity free injection:

As discussed in the introduction section, influence of the capillary term can be significant or negligible, depending on the Leverett-J function. In gravity-free conditions, when there is no density contrast, inclusion of capillary pressure makes the sharp front diffused, and a continuous but steep function represents the saturation distribution versus radius. This problem has been treated by Hussain et al (48), Norbotten (49), Barenblatt (41) and others.

By ignoring the capillary term, the equation is reduced to a strictly hyperbolic one, and possible analytical solutions are continuous or discontinuous functions, or a combination of them (41). The type of solution depends on the initial saturation, the fractional flow function, and the distant (farfield) boundary condition. In primary drainage of water-wet formations such as saturated sandstones, the saturation profile is a combination of shock and rarefaction waves; more specifically, the saturation profile is a shock wave representing a step jump in saturation followed by a rarefaction wave which describes a zone of continuous saturation variation.

In a primary drainage process, a continuous rarefaction wave evolves because of the faster penetration of the larger saturations; i.e., the fractional flow function is partly convex. Conversely, a concave fractional flow function always creates a shock wave. By plotting a tangent line to the fractional flow function that passes through (S,F(S))=(1,1), the far right boundary condition, the extent of the shock wave is obtained. Labeling the saturation at the tangent point Sc, the interval of the shock wave is $[S_c, 1]$ ((41),(50)). If one assumes that the residual water saturation behind the shock wave is smaller than Sc, the saturation front profile is not continuous, Fig (2.13). In this case, a sharp interface assumption will be justified, but if the residual saturation is smaller than S_c, a continuous trail of saturation variation appears and grows over time. This condition has been associated with a strongly water-wet condition (51);(3), and the saturation profile is a continuous function that trails a discontinuous front. In

the second case, the saturation distribution of the injected gas is totally different from widely accepted assumptions.

At a smaller scale, through inclusion of the capillary force, even in the presence of a shock wave the variation of saturation is not discontinuous. Evolution of the capillary fringe makes the discontinuous transition into a steep but continuous transition function (41);(49). Inclusion of the capillary fringe has been addressed previously (52), (49), but to our knowledge the continuous saturation profile behind the shock wave has not been treated rigorously.

The degree of non-linearity of the relative permeability functions is proportional to the value of S_c, and for a lower degree of nonlinearity, the value of S_c approaches 1. The extreme condition arises when the relative permeability functions are assumed to be linear; in that case Sc is equal to 1. In other words, for a set of linear relative permeability curves there is no shock wave and the saturation profile is a fully continuous rarefaction wave between S = 0 and S =1. A linear relative permeability assumption is generally a poor approximation for porous formations with significant capillary pressure effects, but for fractures or very coarse-grained strata, they are reasonably realistic (32).

$$\begin{cases} k_{rw} = \left(\dfrac{S - S_{rw}}{1 - S_{rw}} \right)^{\alpha} \\ k_{rg} = \beta \left(1 - \dfrac{S - S_{rw}}{1 - S_{rw}} \right)^{\alpha} \end{cases} \tag{2.24}$$

Parameters in these relative permeability functions are determined by interpolation of laboratory measurements. For a primary drainage process, according to core analysis of Ellerslie sandstone, the best fit is often chosen as $\alpha = 2$ and $\beta \approx 0.8$ (32). The suggested formulations for the capillary pressure in the literature are generally discontinuous, but this

work is addressing primary drainage only with no hysteretic cycles of saturation (i.e. no cyclic injection and production).

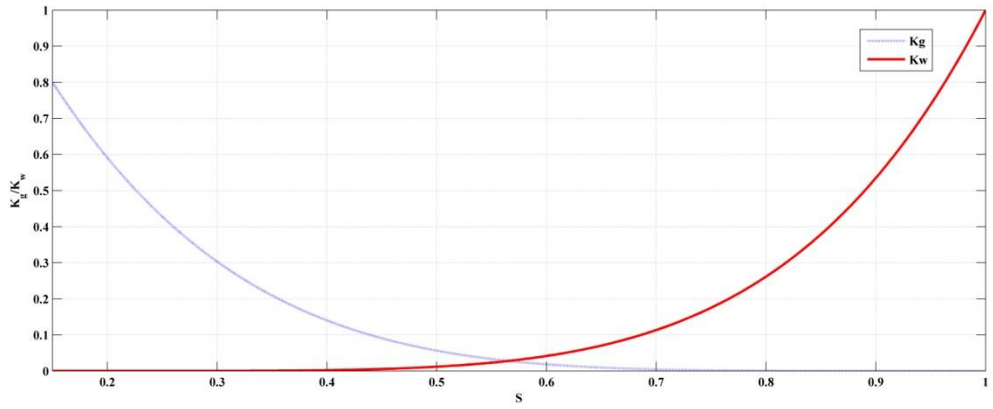

Fig 2-9 Second-order relative permeability function

2.4.2.2 Gravity Drainage:

The effect of gravity and the different hydrostatic pressure (gravity head) distributions of columns of fluids of different density complicate the pattern of saturation progression during injection. Injection of a gas (or a lighter supercritical fluid or a solvent) into a water-saturated formation is called "primary drainage" (53), and the density contrast generates a vertical capillary pressure effect. The vertical part (function of z) of capillary pressure is assumed to be constant and equal to $\Delta\gamma = \gamma_w - \gamma_n$, an assumption stipulated from the vertical equilibrium assumption of fluids and the condition of negligible vertical velocity (which is realistic for large-scale rapid injection into tabular flat-lying reservoirs). The vertical equilibrium assumption has been discussed and justified several times (51), (40). The vertical part (function of z) of the capillary pressure associated with a radial capillary pressure calculated as the vertically averaged saturation leads to wedge-shaped contours of equal saturation (isosats). Lateral progression of the non-wetting phase saturation is faster on the top compared to the bottom because of the lower initial pore pressure of the host fluid on the

top of the aquifer (the different hydrostatic pressure distributions). Formulation of the positions of the isosats is necessary for two-dimensional analytical solutions for the saturation in the transition zone. Combining the radial and the vertical part of capillary pressure, a global functional for the capillary function is obtained and stipulation of the capillary pressure contours, which are equivalent to the saturation contours, then becomes possible.

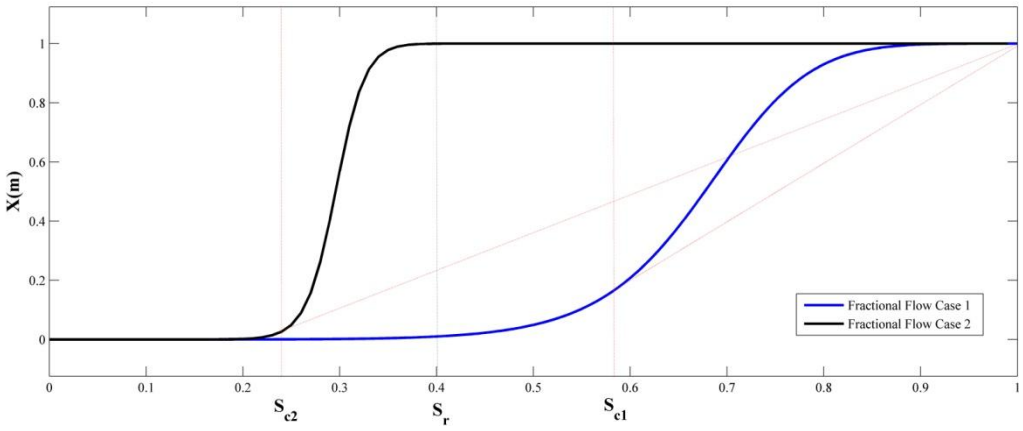

Fig 2-10 Case 1 is the strongly wet formation with minimal transition zone; in Case 2 the transition zone grows over time.

.

Post injection spreading of the injected CO_2 under the assumptions of sharp interface and vertical equilibrium has been studied by Hesse et al. (54) and a series of self-similar solution are developed. Early time drainage of the light nonwetting is proportional to $t^{1/2}$ when the injectate fills the thickness of the aquifer. This is called early time self similar solution and has been solved by Hupert et al. (55).

After substantial time, the gravity driven component of velocity increases and the gaseous plume becomes a thin layer of gas spreading underneath the cap rock. Late time propagation of is still self similar and proportional to $t^{1/3}$ (54).

In a confined horizontal tabular formation, the injectant invades the pore space and pushes the host wetting liquid away from the injection zone. In an unconfined configuration, the flow

of ambient fluid is negligible as the less-dense fluid can rise in a largely unconstrained manner. In the first case, the ratio of viscosities is a key parameter in estimating the size of the transition zone. Nordbotten et al. (39), (49), (56) derived an analytical solution assuming a sharp interface between the host liquid and the trailing completely drained zone and the total gas content at any radius is lumped only at the top of the aquifer. Juanes et al. [(57)] extended this solution to a secondary imbibition process and estimated the magnitude of the residual trapping mechanism for the host fluid. Sloping aquifers (inclined geometries) and the effect of a capillary fringe were studied in later works (58), (21). In most of these works, the effect of permeability and the type of relative permeability function chosen are not discussed. For instance, in (57) the intrinsic permeability of the formation is not mentioned, nor in (39). Although the residual saturation in the fully drained zone is incorporated in the solution procedure, the appropriate type of relative permeability functions does not enter the solutions. Similar approach for gaseous propagation in a half space geometry is also presented by Lyle et al. (59).

Gravity flow in porous media has been the subject of many studies. Huppert and Wood (1995) derived an analytical solution for gravity flow in sloping aquifers by assuming flux of a continuous plume with a density different than the host fluid density. The ratio of the plume depth over the aquifer thickness ($\frac{h}{H}$) is stated as the unknown of the problem for the steady-state condition (55). Golding et al. extended the same methodology and derived a similarity solution and included the effect of the capillary fringe in their analytical solution (60). The fundamental assumption for both these solutions is that the aquifer is unconfined ($h \ll H$) and therefore the viscosity of the host fluid (generally taken to be water) is not important. Nordbotten et al. (56),(61) derived an axisymmetric analytical solution for gravity override including an inclined geometry, and later also included the capillary fringe effect (49),(58).

They also included the effect of a viscosity contrast and relaxed the assumption of aquifer confinement.

Gasda et al. (62),(63) used the concept of vertical capillary/gravity equilibrium; by assuming pseudo-linear relative permeability functions, the governing equations reduced to a 1D horizontal set of equations. The effect of solubility trapping of CO2 was also included. Juanes et al. (57) used a similar problem statement and derived the shape of the gaseous plume over time, eventually including cases of sloping aquifers and capillary trapping in their published work (64). Numerical modeling of CO_2 sequestration has been studies extensively as well, but time scale of the process makes the numerical analysis very expensive (65)(66).

The approaches of these authors are all similar. First, an interface is assumed that separates the pore space into a fully drained zone and an intact water zone; this is analogous to progression of a shock wave (a leading discontinuous front) where the zone behind the shock wave is completely stripped of mobile water and the saturation is everywhere equal to the residual saturation. This approximates only the case of strongly water-wet formations where, by inclusion of a capillary pressure, a transition zone with an abrupt variation of saturation will appear. Second, this interface configuration is applied to the mass conservation equation for an incompressible injectant, and analytical solutions for the interface position are thus derived.

In the absence of capillary forces, the transition becomes small enough to be assumed as a sharp interface. This is proved by Nordbotten et al. (58) using a large scale capillary pressure approach. From physical point of view, vertical equilibrium condition is only the case when the capillary force is equal to the buoyancy forces. In the other words, theoretically negligible capillary pressure and vertical equilibrium assumptions are not consistent.

The main postulate in these works is the assumption of a discontinuous (shock) drainage front that serves as a discrete border between the intact host liquid and the less dense phase in the completely drained zone, and the total absence of a transition zone of varying saturations. The discontinuous saturation transition is also known as the Rankine-Hugoniot jump condition (67), (50). Similar to Fig (2.13), if a discontinuous saturation transition (i.e. a shock wave) is dominant, the sharp interface assumption is a reasonable approximation, and this may be an acceptable postulate if the viscosity of the injectant is substantially greater than that of the host liquid. But, as shown in Fig (1b), depending on the relative permeability functions and the residual water saturation (S_r), the profile of drainage can range from a continuous transition to a combination of a continuous transition and a discontinuous jump Fig (2.13), or even an approximately sharp jump. It is apparent and indeed observed in all real cases where the injectant viscosity is substantially lower than that of the host wetting liquid, development and evolution of a continuous transition zone (i.e. a rarefaction wave) takes place (21).

The continuous transition of saturation behind the shock wave is important from different point of views. The growing extended transition zone provides a huge surface contact area between the host fluid and the injectant. This accelerates diffusively-dominated chemical interactions such as dissolution of the injectant into the host liquid, vaporization of water and precipitation of salt, and mineral interactions with fluids such as stripping of the adsorbed water from the surfaces of silicate minerals or the dissolution of carbonates in the presence of weak carbonic acid under pressure. Additionally, if one ignores the existence of the continuous trail of saturation, the effect of relative permeability functions is not even considered in the breakthrough of the gas, yet, the set of applied relative permeability functions has a significant effect on the saturation distribution.

Analytical treatment of the transition zone is complicated and little has been achieved for realistic conditions. For one-dimensional and cylindrical geometries, the Buckley-Leverett solution was developed (68)(41)(69). However, this solution can be extended to any arbitrary shape of isosat, and by forcing the shape of isosat to the general mass conservation equation, a hyperbolic governing equation can be recovered. This is explained in the following section.

2.4.3 Mass transfer:

Mass transfer mechanisms in CO_2 sequestration are important from two points of view, to provide an estimation of the rate of mixing (time scaling), and to calculate an ultimate capacity of the saline aquifer for disposal of CO_2 in its dissolved form. Diffusion coefficients for a multicomponent system are reported based on experimental measurements, and also the formulations have been presented based on irreversible thermodynamics (26)(70) and kinetic theory (71)(72).

In this case, a rigorous physical model is required for modeling the mass transfer of components through different phases. Multicomponent diffusion results from the gradient of concentration, the pressure (because of capillary pressure) and the temperature (thermal diffusion). If the field is supposed to be stagnant (no significant phase velocities), all the mass transfer is considered to be diffusive. However, there are several sources of motion in the bulk liquid.

Gravitational override is a faster phenomenon compared to diffusion of CO_2 from the interface, and this provides a CO_2-free interface for the gas-rich domain. Consequently the mass transfer because of diffusion increases appreciably. The other source of bulk flow velocity is natural convection resulting from induced density gradients. The latter phenomenon is also expected to accelerate mixing processes significantly (9).

Diffusive and advective fluxes exist throughout all domains in the porous medium, both in liquid-rich and in gas-rich regions. Although the molecular diffusion coefficient in liquid is much larger than in a gas mixture, because of the higher molar density of liquid, the rate of diffusive mass transfer in both is of the same order of magnitude (73).

Molecular diffusion is a slow process, and therefore it is not feasible (in a practical sense) to rely on the process for mixing of the injected gas and the host liquid, but the onset of natural convection, density-driven motion, and other induced velocity fields (e.g. thermal convection effects) could provide significantly better environments for the mixing process.

As has been discussed previously, multicomponent diffusion can be described based on two models, the first of which is based on molecular kinetics. In order to clarify the molecular diffusion from the kinetics point of view, each molecule is considered as an individual particle. The particles are in continuous motion, and the mean free path (MFP) of the particle represents the concentration of the molecules. In multicomponent systems, particle collisions could be between a pair of unlike molecules, a pair of similar type molecules and finally between molecules and the porous wall.

The Stefan-Maxwell equation describes the momentum transfer of particles when the collision between unlike molecules is dominant. Based on the different velocities of molecules of the different chemical components, the concentration gradient is

$$\nabla\left(\frac{p}{RT}x_i\right)=\sum_j \frac{N_j x_i - N_i x_j}{D_{ij}} \tag{2.24}$$

In this equation, i and j represent the chemical components and D_{ij} represents the binary diffusion coefficient. In the absence of a global pressure gradient, the Stefan-Maxwell formula is valid (71).

If the MFP of molecules is much larger than mean pore diameter, the frictional force between molecules and solid matrix becomes important. This phenomenon is called the Knudsen effect (72)

$$\nabla\left(\frac{p}{RT}x_i\right)=\frac{N_i}{D_i^k} \tag{2.25}$$

Here, D_i^k represents the MFP of molecules and average pore diameter of the media. Finally, the effect of momentum transfer results from intra-molecular viscous friction forces and is dominant in systems with pore diameters larger than the MFP.

$$N_i=-\frac{x_i B_o p}{\mu_i RT}\nabla p \tag{2.26}$$

B_o is a variable representing the porous medium and μ is the viscosity of the i^{th} component. If all the mentioned effects are present in the process, the total mass flux will be

$$N_i=N_i^V+N_i^D \tag{2.27}$$

$$N_i^V=-\frac{x_i B_o p}{\mu_i RT}\frac{\partial p}{\partial z} \tag{2.28}$$

and

$$\frac{1}{RT}\frac{\partial\left(px_i\right)}{\partial z}=\sum_j\frac{N_j^D x_i-N_i^D x_j}{D_{ij}}-\frac{N_i^D}{D_i^k} \tag{2.29}$$

The first term represents the advective component of mass transfer and the second term is the diffusive component of mass transfer.

From a totally different point of view, diffusion of mass components is a phenomenon arising from nonequilibrium conditions for two components, and this nonequilibrium condition could arise because of gradients of concentration, temperature and pressure. There are several approaches towards multicomponent diffusion found in the literature (70) (26), and most of them derive the diffusion coefficients based on entropy production.

Irreversible thermodynamics approaches to diffusive mass flux are formalized in the following manner

$$J_i = -c\left(\sum D_{ij}^M \nabla x_j + D_i^p \nabla p + D_i^T \nabla T \right), \qquad i = 1, \quad ..., \; n-1 \tag{2.30}$$

This expression includes all molecular, pressure and thermal diffusion terms.

A mixing process is a combination of a diffusion dominated part and a convective flux dominated part, and their ratio is called the Sherwood number. Sherwood number (Sh) is the ratio of convective mass transfer coeficient to diffusive mass transfer coefficient, and modified Sherwood number is total mixing (advective plus diffusive) to the mixing achieved by pure diffusion alone (74) (4). As discussed before, the mixing process may start from pure diffusion, and after the onset of natural convection from the generation of density differences, the mixing process becomes convectively dominated.

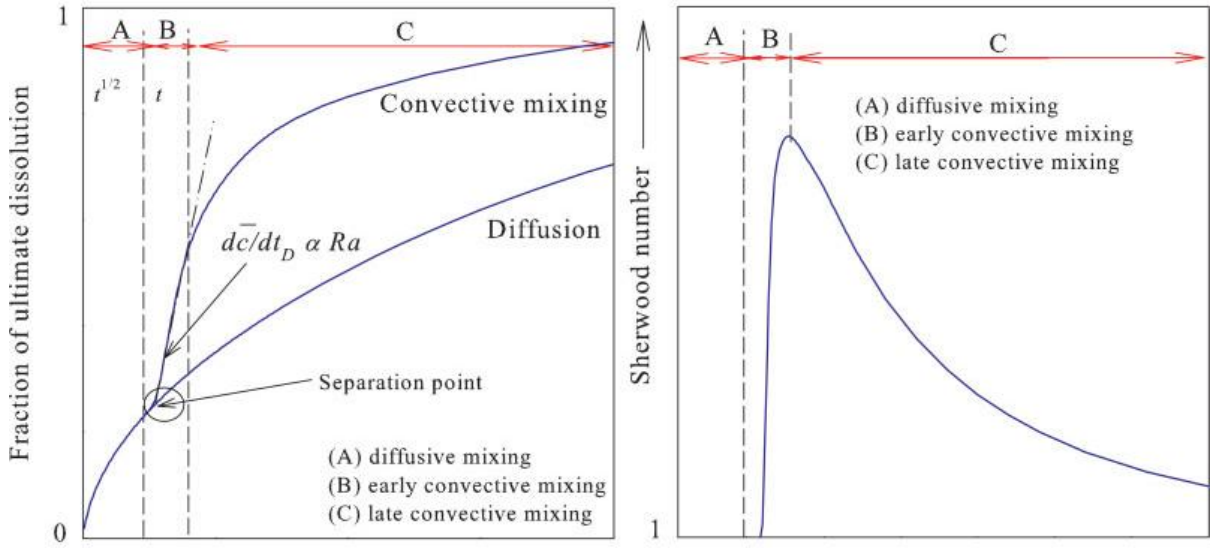

Fig 2-11 a) Diffusive and convective mechanisms' contribution for mixing b) Sherwood number versus time (Hassanizadeh, The Effect of Natural Flow of Aquifers and associated dispersion on the onset of buoyancy-driven convection in a standard porous media 2009)

2.4.3.1 Multiphase system:

Interfacial mass transfer flux is proportional to the surface contact area in the two phase zone, and surface contact area is a pore-scale quantity and is randomly distributed in the pore structure. To present the mass flux using macro scale quantities, different strategies can be taken. One is local thermodynamic equilibrium and the other is kinetic description based on some (linear) relationship. In the local thermodynamic equilibrium approach it is assumed that equilibrium concentration is reached everywhere in averaging volume. In the case of primary drainage, this approach assumes that in a two phase point (saturation is not equal to one), the concentration of the injectant component in the wetting phase is reached its equilibrium concentration. This assumption is physical only when the rate of the mass transfer is much faster than rate of phase partitioning, for instance fast mass transfer or slow drainage-imbibition rate. However if large flow velocity occurs, such as during air sparging or CO_2 injection, the local thermodynamic assumption results in an incorrect answer (74).

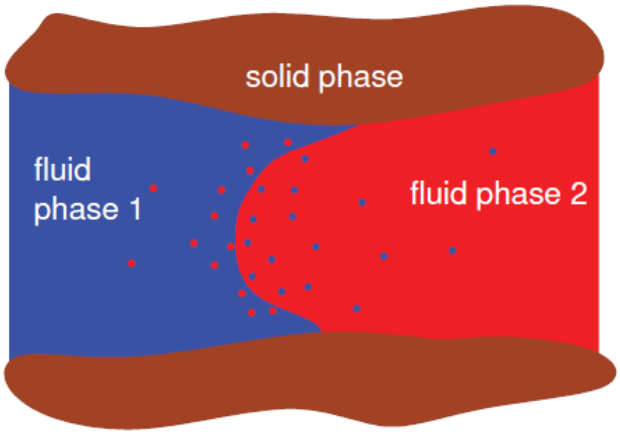

Fig 2-15 Mass transfer process (evaporation, dissolution, condensation) imply transfer of component cross the fluid-fluid interface (Niessner 2011)

Conversely, the kinetic mass transfer approach presents the mass transfer flux as proportional to the difference of equilibrium and actual concentration. Large differences in the actual and equilibrium concentrations results in fast mass transfer. In the case that the actual concentration is equal to the equilibrium concentration, the mass flux is zero. This special case is the thermodynamic equilibrium case, and local equilibrium is used in most commercial mathematical simulators (75) (74).

$$Q_{\alpha\to\beta}^{\kappa} = k_{\alpha\to\beta}^{\kappa}\left(C_{\beta,s}^{\kappa} - C_{\beta}^{\kappa}\right) \tag{2.31}$$

In Eq (2.46), k represents the kinetic mass transfer, and it can be quantified based on different excremental data. $C_{\beta,s}^{\kappa}$ is the equilibrium concentration component β in phase κ and C_{β}^{κ} is the actual concentration of component β in phase κ. Commonly it is related to the modified Sherwood number as

$$k = Sh\frac{D_m}{d_{50}^2} \tag{2.32}$$

Where D_m is the molecular diffusion coefficient of phase κ and d_{50} is the mean size of grains. Sherwood number is related to Reynold's number and non-wetting saturation.

$$Sh = p\,\mathrm{Re}^{q}\,S_n^{r} \tag{2.33}$$

Where p, q and r are fitting parameters.

The kinetic approach provides more realistic mathematical basis for simulation of mass transfer in multiphase zone, but the kinetic coefficient for mass transfer is the challenge. Most of the kinetic mass transfer coefficients are estimated based on Sherwood number, and other thermodynamic state variables (e.g. temperature, pressure and composition) are not correlated to the mass transfer coefficient.

The equilibrium based approach usually overestimates the mixing rate (dissolution, vaporization,…) and since the local equilibrium is assumed for each grid or element (in numerical method), the meshing should be adoptive to the rate of mass transfer.

3 Prediction of Interface position in a linear relative permeability system

3.1 Introduction:

We now will extend considerably the physical conditions for such solutions to more closely represent real behavior in porous media where a continuous transition zone is always generated if a lower viscosity phase is injected. Specifically, the transition zone of continuous saturation distribution in the presence of gravity in a tabular confined horizontal porous formation is studied. There are two important constitutive equations which are influential on the saturation distribution: relative permeability functions and the Leverett-J function. Also, inclusion of density contrast changes the saturation distribution drastically. First we assume the relative permeabilities are linear as that is the simplest possible case, and only focus on the influence of different Leverett-J functions.

In gravity-free conditions, by assuming linear relative permeability functions, the fractional flow function will be strictly concave and the transition zone is thus completely continuous. In gravity-drainage, linear relative permeabilities provide a continuous transition zone, but the size of the transition zone tends to zero for negligible capillary pressures. Here, an analytical solution is proposed for set of linear relative permeabilities for an arbitrary Leverett-J function. The important contribution of the analytical solution is the quantitative influence of the gas-entry capillary pressure on the size of the transition zone. Linear relative permeability assumptions are not physical for most practical cases, and that will be relaxed in the next chapter.

The assumptions of the analytical framework are

- Negligible buoyancy-driven (vertical) movement of the lighter fluid, i.e., radially (e.g. horizontal) dominant velocity of water and the lighter injectant. This assumption is discussed under the name of capillary/gravity condition or vertical equilibrium in various publications (40),(76),(51), and is addressed later.

- The fluids and the rock are incompressible (a robust assumption if constant pressure injection is used).
- The fluids are immiscible.

Families of isosats for three different but important injection geometries will be developed. To verify the analytical results, a 2D numerical model was written, and analytical results thereby compared with numerical solutions. The numerical discretization is explained in chapter four.

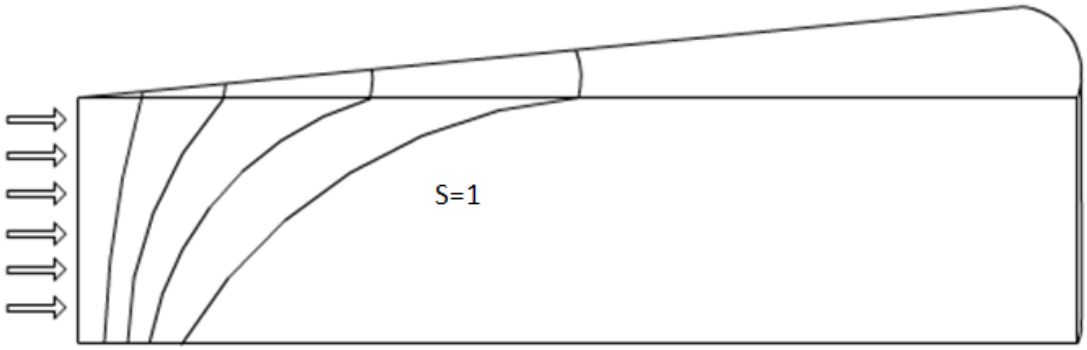

Fig 3-1 Schematic configuration of isosats for axisymmetric vertical source injection into a tabular aquifer

3.2 Vertical Equilibrium:

For a vertically confined, flat-lying and laterally infinite tabular aquifer, vertical equilibrium is the generally accepted assumption (76),(56). For the special case of gravity override of the injectant, the validity of this assumption is shown in several works (51),(40).

It is assumed that saturation progression is driven only by the imposed injection source and that velocity is therefore horizontal. Of course, this is correct only if the buoyancy-driven flux is negligible compared to pressure-driven flux and if the vertical pressure distribution remains hydrostatic, but these are reasonable assumptions for most realistic forced injection cases. The mass conservation for the incompressible system is

$$\nabla.\bar{u}_t = 0 \tag{3.1}$$

In Eq.(3.1), the bar indicates that the variable is vectorial. Because the horizontal length of the domain L is much larger than its height,

$$\frac{H}{L} = \varepsilon \langle\langle 1 \tag{3.2}$$

Consequently $u_l = \varepsilon u_v$, and vertical velocity is indeed far smaller than radial velocity (40).

3.3 Third order polynomial Leverett-J function:

In simple gravity-free geometries such as one-dimensional flow, centrally symmetric two-dimensional radial flow, or spherically symmetric flux, isosat positions are trivially known. However, in realistic applications like the vertical fully penetrating line source, the horizontal well much longer than thickness of the aquifer, or injection in the presence of non-negligible gravity forces, the isosat positions are complex and change with time. A capillarity-based approach will be introduced for the inclusion of the gravity force in the case where relative permeability functions are assumed to be linear.

Assuming negligible vertical velocity, the pressure has radial and gravitational parts expressed as

$$P_w = p_w(r) - \gamma_w z \tag{3.3}$$
$$P_n = p_n(r) - \gamma_n z \tag{3.4}$$

And therefore, for the capillary pressure

$$P_c = p_c(r) + \Delta\gamma z + C \tag{3.5}$$

Eq (3.5) is the analytical expression of capillary pressure decomposed into two parts: the first term - $p_c\,(r)$ - is only a function of r, and the second term - $\Delta\gamma z$ - is only a function of z. These are referred to as the radial and vertical components of the capillary pressure. Eq (3.5)

is valid for any value of r and z and even in the single phase wetting zone where the gas is not present. It seems ambiguous to define a pressure for a phase in the zone that the phase does not exist, but it should be noted that capillary pressure that is defined here is not the precise physical expression of the capillary pressure, but is an analytical formulation that correlates pressures to saturation (e.g. $S = J^{inv}(P_c)$).

In numerical schemes, the relationship is reversed, and saturation is correlated to capillary pressure, and in a more detailed description, the gaseous pressure is only defined in the two-phase zone when the gas content is non-zero (e.g. $P_c = J(S)$). Hence, in the approach that is taken in this work, the correlation is defined to be similar to physical concept of capillary pressure in the two-phase zone, but in the single phase zone (S=1), it is assumed that the pressure in the non-wetting phase is zero. This results in a negative capillary pressure that is less than the gas entry capillary pressure. Hence, in this formulation, a function is stipulated that gives the saturation for a capillary pressure larger than the gas entry pressure, and a saturation equal to one for any capillary pressure less than the gas entry pressure. This approach is also used by many others (49), (58) and (60).

P_c is the global capillary pressure function and p_c is the radial part of P_c. By averaging over the aquifer thickness ($\widetilde{T}_{(r)} = \frac{\int_0^H T_{(r,z)} dz}{H}$)

$$\widetilde{P}_c = p_c(r) - \frac{\Delta\gamma H^2}{2} + C = p_c(r) + D \tag{3.6}$$

C and D are constants in this equation, and by introducing the J-Leverett function

$$P_c = \frac{\cos(\theta) J(S)}{\gamma \left(\frac{\varphi}{K}\right)^{1/2}} = j(S) \tag{3.7}$$

Here, *j(S)* is a nonlinear function, therefore the averaged value of P_c is not a linear function of $\tilde{S}$. By linearization of the capillary function, the relationship between the vertically averaged capillary pressure and the vertically averaged saturation is obtained. A single linear approximation for the Leverett-J function for the entire range of saturation eliminates the variation in the slope of the curve and consequently leads to excessive error for realistic cases.

In order to find an appropriate formulation for correlation of saturation and capillary pressure, a third-order polynomial interpolation function is chosen. Most existing interpolation functions are discontinuous (23), and only fit to saturation values close to the residual saturation. In Fig. (3.2), the measured lab results of P_c versus S_w for the primary drainage (upper curve) and secondary imbibition (lower curve) at 8 bars and 28°C for injection of CO_2 with the rate of 0.5 ml/h is presented.

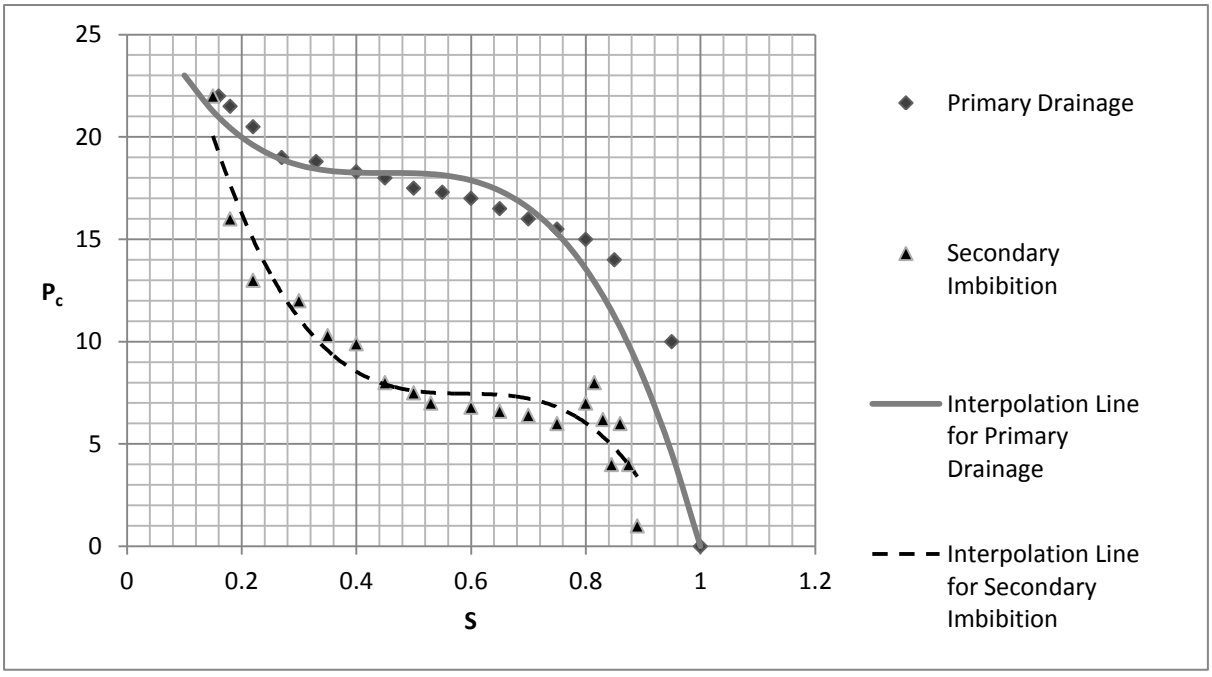

Fig 3-2 A third-order polynomial interpolation of Leverett-J function based on the data from (Plug and Bruining 2007)

The interpolation function for the primary drainage part is a third-order polynomial function.

$$P_c = P_{cm}\left(P_1 - P_2\left(S_e - S_1\right)^3\right) \tag{3.8}$$

$$P_1 = \frac{\left(1-S_1\right)^3}{\left(1-S_1\right)^3 + S_1^3} \tag{3.9}$$

$$P_2 = \frac{1}{\left(1-S_1\right)^3 + S_1^3} \tag{3.10}$$

In Eq. (3.8), P_{cm} and S_1 are the parameters of the capillary curve, indicating the maximum and the inflection point of the curve, and S_e is effective saturation

$$S_e = \frac{S - S_r}{1 - S_r} \tag{3.11}$$

where S_r is the residual saturation. The main advantage of this formulation over Corey's capillary function is the continuity of the function. This allows the use of Taylor series expansion and a truncation method to derive the linearized approximation of the Leverett-J function. This method is used to approximate the vertically averaged value of the capillary pressure.

A third-order interpolation function fits reasonably well, but nonlinearity of the function makes the averaging operation impossible, so a local linearization method is used. By using the Taylor expansion around different values of saturation, the linearization error is minimized. The linearized approximation of Eq. (3.12) around $S_e = S^*$ is

$$P_c = P_c^{s^*} + O\left(\left(S_e - S^*\right)^2\right) = P_{cm}(P_1 - P_2(S^* - S_1)^3) - 3P_2(S^* - S_1)^2\left(S_e - S^*\right) + O\left(\left(S_e - S^*\right)^2\right) \tag{3.12}$$

And by averaging Eq. (3.12),

$$\tilde{P}_c^{S^*} \approx E\left(S^*\right) - A_{s^*}\left(\tilde{S}_e - S^*\right) \tag{3.13}$$

3.3.1 Vertical well:

By employing a linear relative permeability relationship and averaging over the entire height of the aquifer, the two-dimensional problem is reduced to a one-dimensional problem.

$$\begin{cases} \bar{u}_w(r,z) = -\lambda_w(S_e)\nabla\left(p_w(r) - \gamma_w z\right) - \lambda_w\gamma_w\bar{e}_z \\ \bar{u}_n(r,z) = -\lambda_n(S_e)\nabla\left(p_n(r) - \gamma_n z\right) - \lambda_n\gamma_n\bar{e}_z \end{cases} \rightarrow \begin{cases} \tilde{\bar{u}}_w(r) = -\lambda_w(\tilde{S}_e)\nabla p_w(r) \\ \tilde{\bar{u}}_n(r) = -\lambda_n(\tilde{S}_e)\nabla p_n(r) \end{cases} \tag{3.14}$$

If the vertically averaged capillary pressure term is negligibly small, as can be proven by normalization, the classic Buckley-Leverett equation can be recovered.

$$\tilde{\bar{u}}_t = -\left(\lambda_n(\tilde{S}_e) + \lambda_w(\tilde{S}_e)\right)\nabla p \tag{3.15}$$

And by multiplying with the fractional flow function one obtains

$$\frac{F(\tilde{S}_e)Q_o}{2\pi r}\bar{e}_r = -\lambda_w(\tilde{S}_e)\nabla p = \tilde{\bar{u}}_w \tag{3.16}$$

Taking the divergence of both sides gives

$$\nabla\cdot\left(\frac{F(\tilde{S}_e)Q_o}{2\pi\varphi r}\bar{e}_r\right) = \frac{\partial\tilde{S}_e}{\partial t} \tag{3.17}$$

Which can be written as

$$\frac{\partial}{r\partial r}\left(\frac{F(\tilde{S}_e)Q_o}{2\pi\varphi}\right) = \frac{\partial\tilde{S}_e}{\partial t} \quad \rightarrow \quad \frac{F'(\tilde{S}_e)Q_o}{\pi\varphi}\frac{\partial\tilde{S}_e}{\partial r^2} = \left(1 - S_r\right)\frac{\partial\tilde{S}_e}{\partial t} \tag{3.18}$$

Using the linear relative permeabilities approximation, the fractional flow function is

$$F(\tilde{S}_e) = \frac{\tilde{S}_e}{m-(m-1)\tilde{S}_e} \rightarrow F'(\tilde{S}_e) = \frac{m}{\left(m-(m-1)\tilde{S}_e\right)^2} \tag{3.19}$$

By substituting equation (3.19) in (3.18) and simplifying, the following solution is obtained:

$$\widetilde{S}_e = \begin{cases} 0 & r < \sqrt{\dfrac{Q_o t}{m\pi\varphi(1-S_r)}} \\ \dfrac{m}{m-1} - \dfrac{1}{m-1}\sqrt{\dfrac{mQ_o t}{r^2(1-s_r)\pi\varphi}} & \sqrt{\dfrac{Q_o t}{m\pi\varphi(1-S_r)}} < r < \sqrt{\dfrac{mQ_o t}{\pi\varphi(1-S_r)}} \\ 1 & r > \sqrt{\dfrac{mQ_o t}{\pi\varphi(1-S_r)}} \end{cases} \tag{3.20}$$

Equation (3.20) is the analytical solution for vertically averaged saturation over the height of the aquifer in the absence of a capillary term. This solution is similar to (39), and if a sharp interface separating the gas and the liquid is assumed, the solution is exactly equivalent to that of (39), and (64) when the buoyancy effect is neglected. Also, by employing linear relative permeability functions in (77), Eq. (18) is recovered.

Using Eqs. (3.20) and (3.13), P_c around $S = S^*$ is

$$P_c\big|_{S=S^*} \approx E(S^*) - A^{S^*}\left(\frac{m}{m-1} - \frac{1}{m-1}\sqrt{\frac{mQ_o t}{r^2(1-s_r)\pi\varphi}} - S^*\right) + \Delta\gamma z \tag{3.21}$$

And the functional for $P_c = P_c(S^*)$ will be

$$P_c\big|_{S=S^*} \approx \frac{E^{S^*}}{r} + Ez + C(S^*) \tag{3.22}$$

Where

$$E^{S^*} = \frac{A_{S^*}}{m-1}\sqrt{\frac{mQ_o t}{(1-s_r)\pi\varphi}} \tag{3.23}$$

$$E = \Delta\gamma \tag{3.24}$$

The constant C is only a function of S^*. From Eq. (3.22), the analytical expression for an isosat is

$$\eta = \frac{E_{(t)}^{S^*}}{r} + Ez \tag{3.25}$$

The value of η is different for different values of S, and consequently the exact position of an isosat cannot be determined with the available information; however, the position of the onset contour of saturation can be determined from the boundary condition, and the value of η specified.

$$S_{(r_{\max},H)} = 1 \tag{3.26}$$

$$\eta\big|_{(s=1)} = \eta\big|_{(r_{\max},H)} = \frac{E_{(t)}^{1}}{r_{\max}} + EH \tag{3.27}$$

The value of η is still a function of t. In the next part, the position of the isosat from the analytical solution is compared with numerical results. Details of the numerical model are provided in Chapter 4.

Table 3-1 Characteristics of injection of less viscous, less dense injectant into a water-wet saturated zone, linear relative permeability, in an axisymmetric geometry.

$\mathbf{Q_o}$ $(\frac{m^3}{s})$	$\boldsymbol{m = \frac{\mu_w}{\mu_n}}$	$\mathbf{S_r}$	**K (m^2)**	**φ**
0.0015	**19.3**	**0.1**	$\mathbf{10^{-14}}$	**0.1**

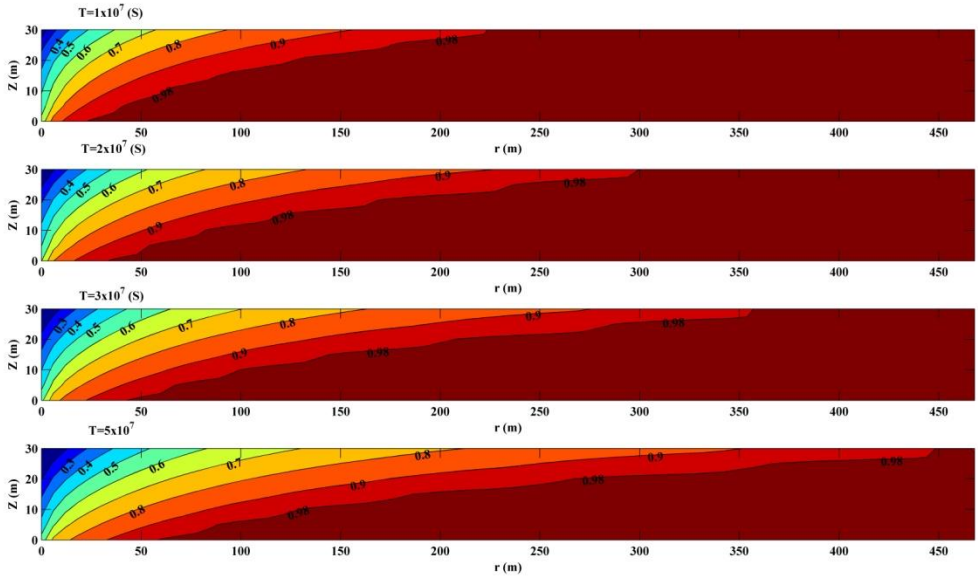

Fig 3-3 Numerical results for saturation progression for an axisymmetric geometry. Different colors represent an extended interfacial zone for the primary drainage process, and the fastest progression of gas belongs to the largest saturation.

Table 3-2 Characteristics of injection of less viscous, less dense injectant into a water-wet saturated zone, linear relative permeability in axisymmetric geometry.

$Q_{0(volumetric)}$ (m^3/t)	$P_{(base)}$	$K_{(m}2_{)}$	$m = \frac{\mu_w}{\mu_n}$	φ	S_r	P_{cm}(Pa)	T(°c)
0.0015	**10 MPa**	10^{-14}	**19.3**	**0.1**	**0.25**	2×10^5	$50^{\circ}C$

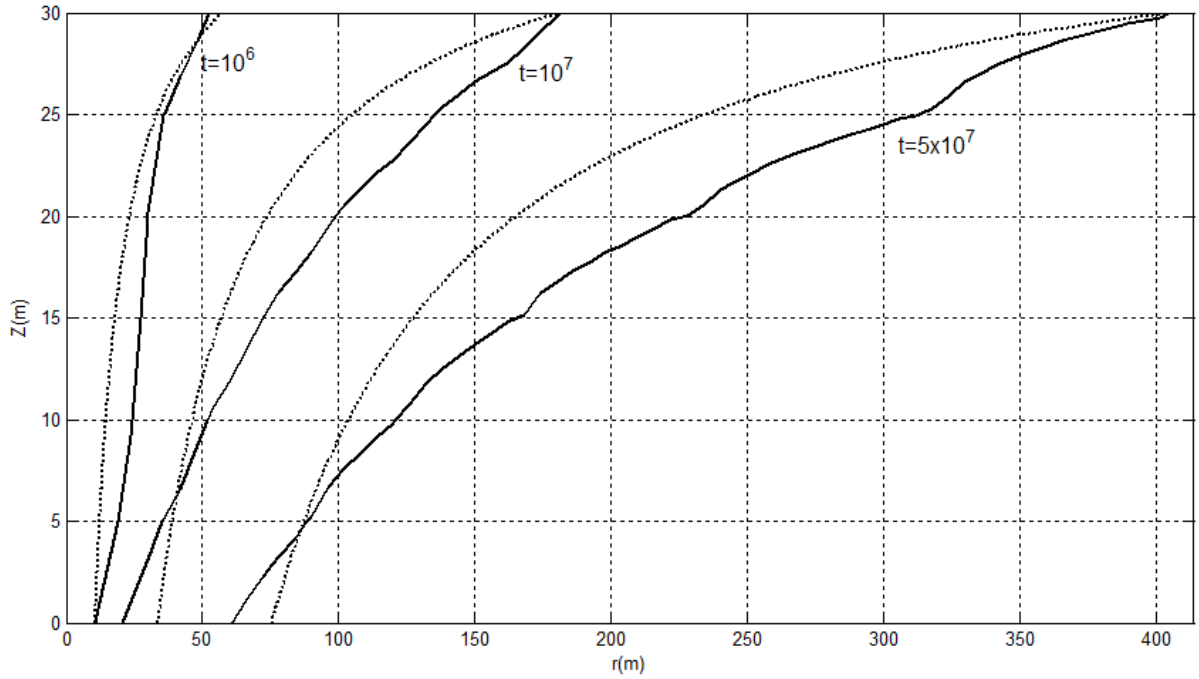

Fig 3-4 A comparison between numerical and analytical results of saturation contours for different times, continuous lines are the numerical solutions. All of the demonstrated contours corresponds to Se=1, which is the outer boundary of the transition zone at different times.

Table 3-3 Characteristics of fluids and formation

Q (mass rate) $\frac{kg}{s\,m}$	Q (volumetric rate) $\frac{m^2}{s}$	P base (*Mpa*)	$\frac{\mu_w}{\mu_{co_2}}$	K m^2	P_{cm} *Pa*	T *C°*
0.115	**0.0003**	***10***	***19.3***	10^{-13}	2×10^5	***50***

1.15 days

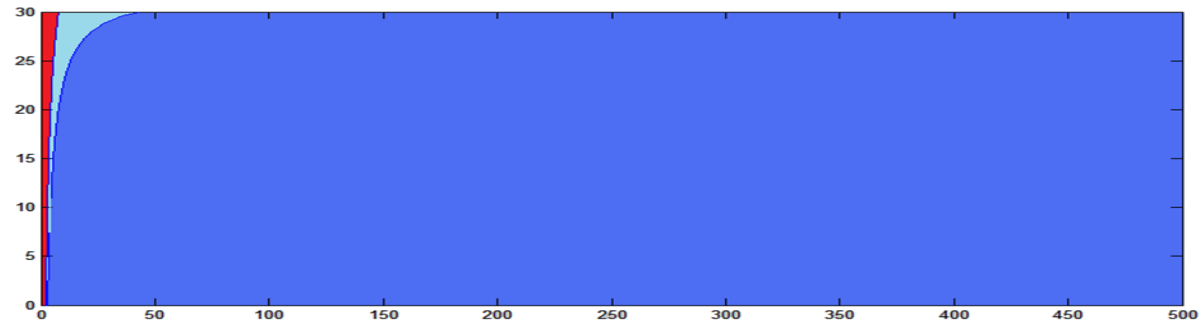

11.57 days

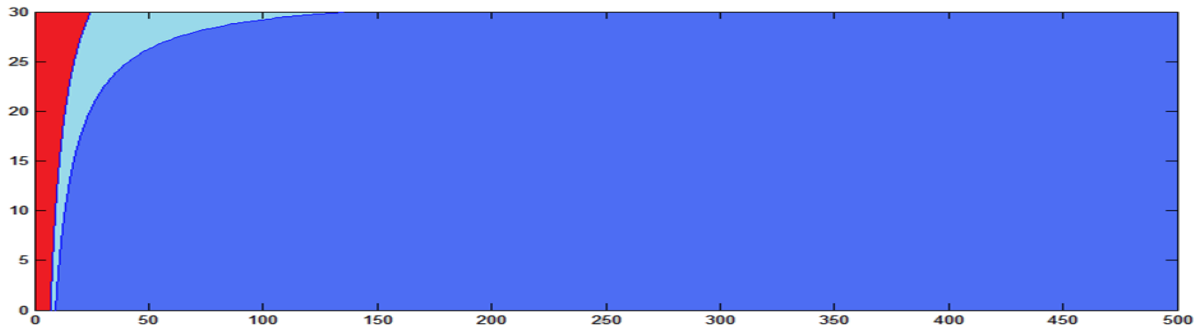

115.7 days

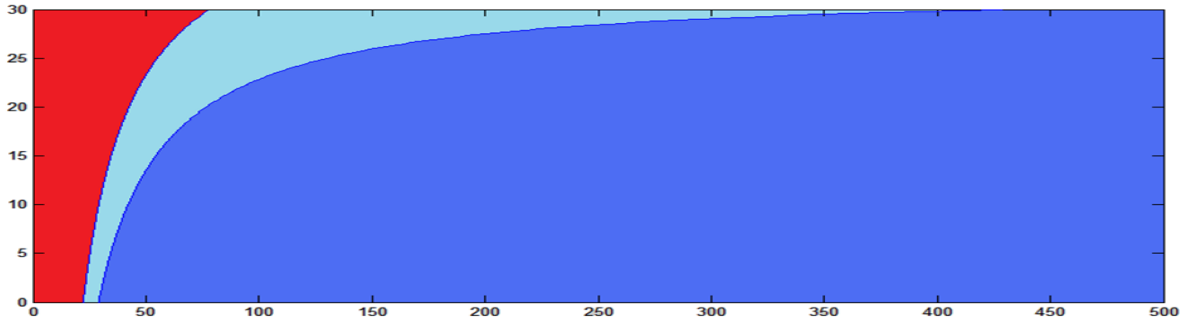

1157 days (3.2 year)

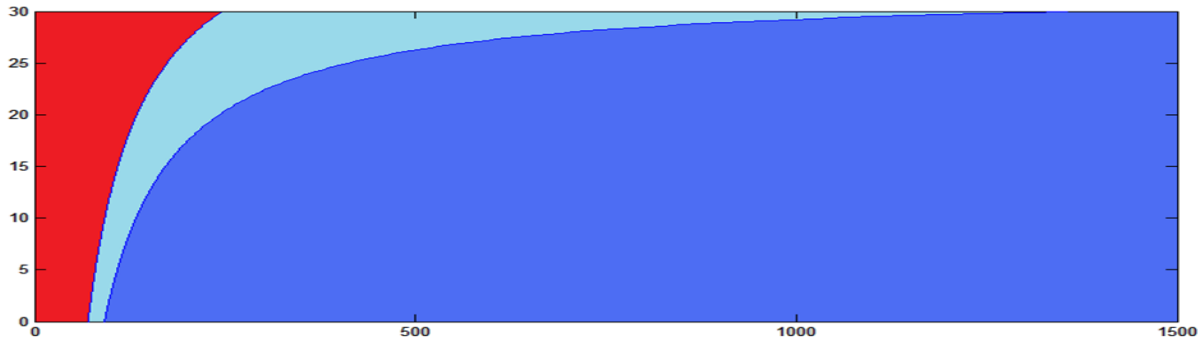

Fig 3-5 Snapshots of saturation distribution at different times, res area represents completely drained zone, blue area represents intact water and light blue represents transition zone

3.3.1.1 Discussion:

Numerical results are always a benchmark for any approximated solution. Fig. (3.4) provides a reasonable comparison between analytical and numerical solution, but as is apparent in the figure the agreement between these two is modest. The analytical solution predicts the

maximum breakthrough of the gaseous plume precisely, but the position of the isosat is not consistent with the numerical solution.

Another deficiency of the analytical scheme is that the Leverett-J function is constrained to a specific type of formulation. Third-order polynomial approximations are only adaptable to specific Pc-S data, and that decreases the precision of the analytical solution. Other sources of error come from the vertical equilibrium assumption which is not correct in all conditions.

Although the analytical scheme does not provide an excellent approximation of the position of isosats, the maximum breakthrough of the plume is calculated reasonably well. In the case of leakage from natural faults or abandoned wells, maximum breakthrough of the gaseous plume is important. Another mathematical scheme is presented later in this chapter that is based on more realistic assumptions.

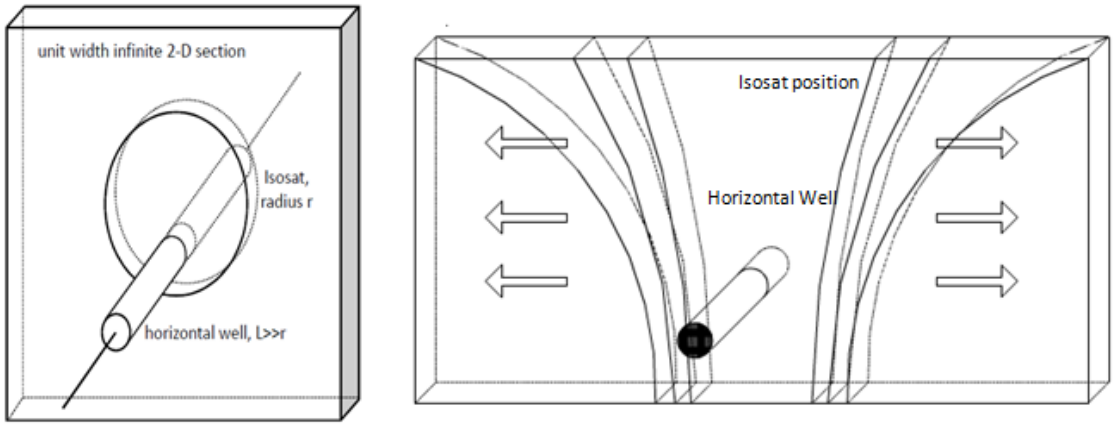

Fig 3-6 Schematic configuration of low-density phase injection from a horizontal well into a tabular confined porous formation. A) Early time injection when the plume has not reached the top and the bottom boundary; isosats are egg-shaped instead of circular because of gravity effects. B) Late time injection, long after the plume has reached the top and bottom boundaries.

3.3.2 Horizontal Well:

During injection into a horizontal well (L >> B), the less-dense phase first invades the pore space close to the well, and as the result of gravity, the radial progression of isosats is not centrally symmetric (Fig. 3.6-a); the isosats move faster upward and slower downward,

giving an egg shape to each isosat. The effective forces are viscous forces coming from the injection source and buoyancy coming from the density difference.

The geometry of the early-time problem approximates a 2-D point injection into an unbounded porous medium. The self-similar isosats are egg-shaped and centered on the injection well before the phase of different density reaches the impermeable boundaries. Although simulation of this early-time period may have little practical importance except in cases of extremely thick reservoirs, the results demonstrate the general capability of this approach.

After some time, depending on injection rate and system properties, the aquifer height B is reached by the light phase, and flux then gradually becomes dominated by laterally symmetric horizontal flow. Once this transition is completed during intermediate time, late-time linear flow dominates (Fig. 3.6-b) and thereafter the isosat distribution is similar to the lateral spreading case solved in previous section, with the difference being plane flux vs. axisymmetric spreading. In general, late time lateral spreading is likely to dominate horizontal well injection behavior in most real cases Fig. (Fig. 3.6-b) until the invaded zone distance becomes a large fraction of the well length.

3.3.2.1 Early-time point source injection:

Based on the assumption of negligible buoyancy driven flow, it is assumed that the gaseous and liquid velocities are both 2D radial in nature. This is analogous to the horizontal velocity of gas and liquid assumption in the lateral spreading case. One may rewrite the generalized Darcy's law in polar coordinates centered at the point source of injection as

$$\bar{u}_w = -\lambda_w \nabla P_w - \lambda_w \gamma_w \left(\sin(\theta)\bar{e}_r + \cos(\theta)\bar{e}_\theta\right) \quad (3.28)$$

$$\bar{u}_n = -\lambda_n \nabla P_n - \lambda_n \gamma_n \left(\sin(\theta)\bar{e}_r + \cos(\theta)\bar{e}_\theta\right) \quad (3.29)$$

Velocities become radial only if the vertical pressure distribution is fully hydrostatic.

$$P_w(r,\theta) = p_w(r) - r\sin(\theta)\gamma_w \quad (3.30)$$
$$P_n(r,\theta) = p_n(r) - r\sin(\theta)\gamma_n \quad (3.31)$$

Substituting equations (3.28) and (3.29) in equations (3.30) and (3.31) and noting that P_w and P_n are radially distributed, one may obtain

$$\bar{u}_w(r,\theta) = -\lambda_w(S_e)\nabla p_w(r) \quad (3.32)$$
$$\bar{u}_n(r,\theta) = -\lambda_n(S_e)\nabla p_n(r) \quad (3.33)$$

Note that although the direction of flux of both fluids is radial, their magnitudes are both functions of global saturation and therefore a function of r and θ. By averaging over θ, the equation reduces to

$$\tilde{\bar{u}}_w(r) = -\lambda_w(\tilde{S}_e)\frac{\partial p_w}{\partial r}(r) \quad (3.34)$$
$$\tilde{\bar{u}}_n(r) = -\lambda_n(\tilde{S}_e)\frac{\partial p_n}{\partial r}(r) \quad (3.35)$$

Herein, $\tilde{S}_e(r) = \frac{1}{2\pi}\int_{-\pi}^{\pi} S_e\,(r,\theta)d\theta$, averaged velocities and saturations are only radial, and it is possible to reduce the set of the equations to a single hyperbolic equation.

$$\tilde{\bar{u}}_t(r) = -\left(\lambda_w(\tilde{S}_e) + \lambda_n(\tilde{S}_e)\right)p_{,r} \quad (3.36)$$
$$\frac{F(\tilde{S})Q_o}{2\pi r}\bar{e}_r = -\lambda_w(\tilde{S}_e)\,p_{,r} \quad (3.37)$$
$$\frac{\partial}{\partial r^2}\left(\frac{F(\tilde{S}_e)Q_o}{(1-S_r)\varphi\pi}\right) = \frac{\partial \tilde{S}_e}{\partial t} \quad (3.38)$$

By using linear relative permeability functions, the value of averaged saturation can be obtained as

$$\tilde{S}_e = \begin{cases} 0 & r < \sqrt{\dfrac{Q_o t}{m\pi\varphi(1-S_r)}} \\ \dfrac{m}{m-1} - \dfrac{1}{m-1}\sqrt{\dfrac{mQ_o t}{r^2(1-s_r)\pi\varphi}} & \sqrt{\dfrac{Q_o t}{m\pi\varphi(1-S_r)}} < r < \sqrt{\dfrac{mQ_o t}{\pi\varphi(1-S_r)}} \\ 1 & r > \sqrt{\dfrac{mQ_o t}{\pi\varphi(1-S_r)}} \end{cases} \quad (3.39)$$

Eq. (3.39) is similar to Eq. (3.20) because the averaged radial distribution of saturation is always similar. The radial term of the capillary solution is obtained based on the locally linearized Leverett-J function assumption, similar to Eq. (3.21)

$$\tilde{P}_c = E_{(t)}^{S^*}(\tilde{S}_e) + C(S^*) \quad (3.40)$$

By adding the gravitational part, the global capillary pressure function can be obtained. The global saturation in (r,θ) space can be obtained by substituting Eq. (3.39) into Eq. (3.40):

$$\eta = \frac{E_{(t)}^{S^*}}{r} + Br\sin(\theta) \quad (3.41)$$

The value of C comes from applying the boundary condition; by implementing the maximum and minimum boundary condition to the saturation contours, this value of C is obtained:

$$\eta\big|_{s=1} = \eta\big|_{(r_{\max},\frac{\pi}{2})} = \frac{E_{(t)}^{1}}{r_{\max}} + Br_{\max} \quad (3.42)$$

Based on the information in Eq. (3.41), the position of the isosat S = 1 can now be determined.

Table 3-4 Characteristics of injection of less viscous, less dense injectant into a water-wet saturated zone, linear relative permeability in point source geometry.

$Q_{(\text{mass rate})}$ $(\frac{kg}{s\,m})$	$Q_{(\text{volumetric rate})}$ $(\frac{m^2}{s})$	P_{base} (MPa)	$\frac{\mu_w}{\mu_{CO_2}}$	φ	K (m^2)	$P_{cm\,(Pa)}$	T (C°)
0.007	1×10^{-5}	15	10.3	0.1	10^{-15}	1.1×10^{6}	50

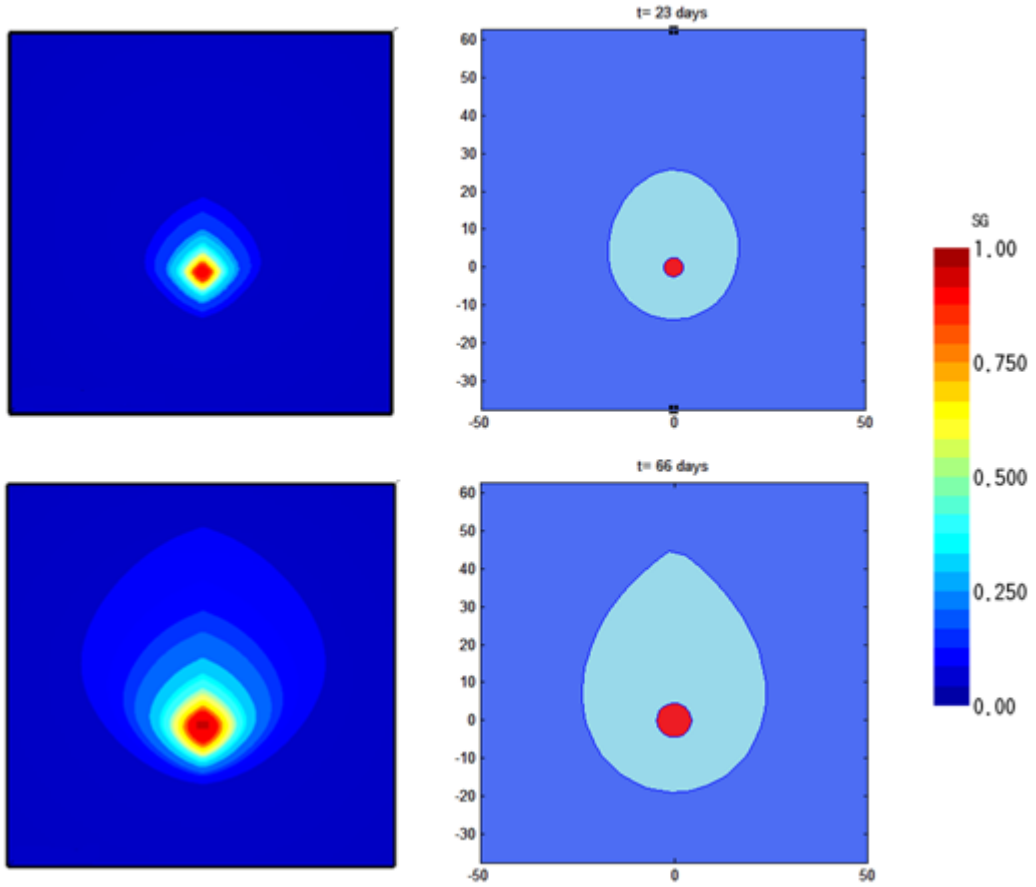

Fig 3-7 A comparison between analytical (right) and numerical (left) solutions for early-time injection. Numerical results are from TOUGH2 ECO2N (Pruess K 2007) , and although the compressibility is non-zero in their numerical model, the generated pressure in the well zone is not very different from hydrostatic pressure, and therefore the effect of compressibility is not significant.

3.3.2.1.1 Discussion:

Fig (3.7) presents a comparison between analytical and numerical results for the position of isosats during injection from a horizontal well when the density of injectant is lower than the host fluid. Elliptical shape of isosats is a result of density head. There is a reasonable qualitative agreement between the numerical and analytical solutions, but significant difference exists in parts of the curves. Sources of error for the analytical scheme are linearization of the Leverett-J function, neglecting the capillary term and the vertical equilibrium assumption.

This analytical solution has limited physical applications due to the generally small thickness of the aquifer (40-100 m) with respect to a typical well length (2 km). In the other words, the thickness of the aquifer is filled with gas in a short time after injection, and after that the drainage process will be only lateral. Lateral spreading of injected nonwetting in the plane flow geometry will be discussed next.

3.3.2.2 Late-time 2D point source injection:

After a relatively short time in the well life, the vertical space between the impermeable boundaries near the horizontal wellbore is filled with injected gas. Once the transition period is largely passed, shown in Fig (3.6-b) from numerical model results, the flow regime approaches linearly lateral plane flow.

$$\bar{u}_w = -\lambda_w \nabla P_w - \lambda_w \gamma_w \bar{e}_z \tag{3.43}$$
$$\bar{u}_n = -\lambda_n \nabla P_n - \lambda_n \gamma_n \bar{e}_z \tag{3.44}$$

Based on the vertical velocity assumption, the vertical pressure distribution is hydrostatic.

$$\bar{u}_w(r,z) = -\lambda_w(S_e)\nabla P_w(r) \tag{3.45}$$
$$\bar{u}_n(r,z) = -\lambda_n(S_e)\nabla P_n(r) \tag{3.46}$$

By averaging over the height of the aquifer, these functions reduce to

$$\tilde{\bar{u}}_w = -\lambda_w\left(\tilde{S}_e\right)\nabla P_w - \lambda_w \gamma_w \bar{e}_z \tag{3.47}$$
$$\tilde{\bar{u}}_n = -\lambda_n\left(\tilde{S}_e\right)\nabla P_n - \lambda_n \gamma_n \bar{e}_z \tag{3.48}$$

And, multiplying by the fractional flow function, the set of equations becomes

$$\tilde{\vec{u}}_t(r) = -\left(\lambda_w(\tilde{S}_e) + \lambda_n(\tilde{S}_e)\right)\nabla P_w(r) \tag{3.49}$$

$$\tilde{u}_t(r) = Q_o \tag{3.50}$$

$$\frac{\partial}{\partial x}\left(\frac{F(\tilde{S}_e)Q_o}{(1-S_r)}\right) = \frac{\varphi\partial\tilde{S}_e}{\partial t} \tag{3.51}$$

As before, by using a linear relative permeability function, Eq. (3.51) is solved as

$$\frac{F'(\tilde{S}_e)Q_o}{\varphi(1-S_r)} = \frac{r}{t} \tag{3.52}$$

And, similar to the procedure in the previous section

$$\tilde{S} = \begin{cases} 0 & r < \dfrac{Q_o t}{m\varphi(1-S_r)} \\ \dfrac{m}{m-1} - \dfrac{1}{m-1}\sqrt{\dfrac{mQ_o t}{r(1-s_r)\varphi}} & \dfrac{Q_o t}{m\varphi(1-S_r)} < r < \dfrac{mQ_o t}{\varphi(1-S_r)} \\ 1 & r > \dfrac{mQ_o t}{\varphi(1-S_r)} \end{cases} \tag{3.53}$$

By assuming a locally linearized J-Leverett function, the global capillary pressure is

$$\eta = \frac{E^{s^*}_{(t)}}{\sqrt{r}} + Bz \tag{3.54}$$

C is evaluated from the boundary condition because the value of saturation is known at the maximum and minimum points:

$$s\big|_{(r=r_{\max},\, z=H)} = 1 \Rightarrow \eta\big|_{s=1} = \eta\big|_{(r_{\max},H)} = \frac{E^1_{(t)}}{\sqrt{r_{\max}}} + BH \tag{3.55}$$

Based on the information in Eq (3.55), the positions of the isosat S = 1 is determined.

Table 3-5 Characteristics of injection of less viscous, less dense injectant into a water-wet saturated zone, linear relative permeability in plane flow geometry.

$Q_o\ (\frac{m^3}{s})$	$m = \frac{\mu_w}{\mu_n}$	S_r	K (m^2)	φ
$3x10^{-5}$	19.3	0.1	10^{-14}	0.1

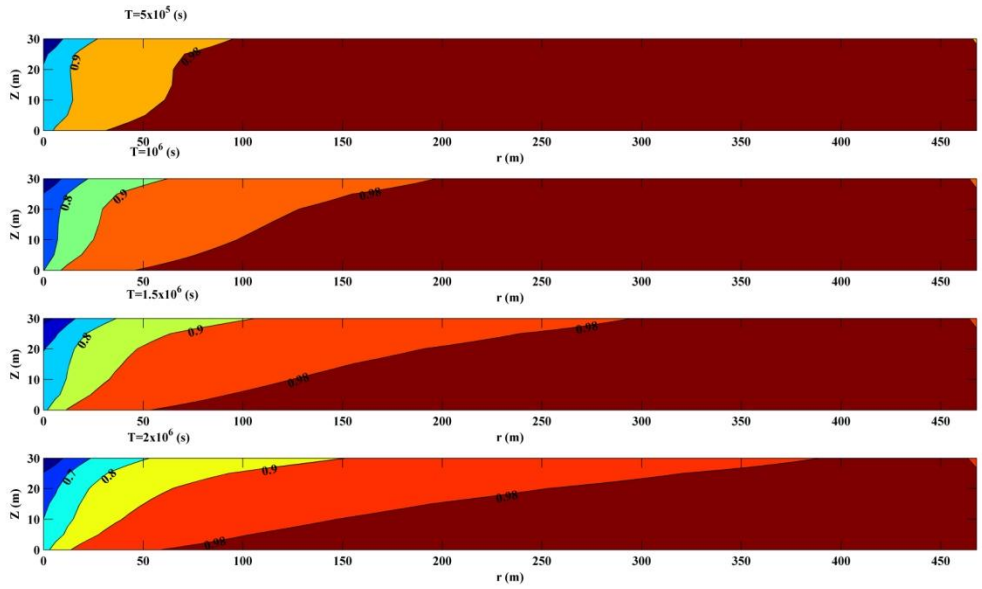

Fig 3-8 Numerical results for late-time primary drainage from horizontal well injection

Table 3-6 Characteristics of injection of less viscous, less dense injectant into a water-wet saturated zone, linear relative permeability in plane flow geometry.

$Q_{(volumetric\ rate)}\ (\frac{m^2}{s})$	P_{base} (MPa)	$\frac{\mu_w}{\mu_{CO_2}}$	φ	K (m^2)	P_{cm} (Pa)	S_r	T (C°)
1×10^{-5}	10	19.3	0.1	10^{-14}	2×10^5	0.25	50

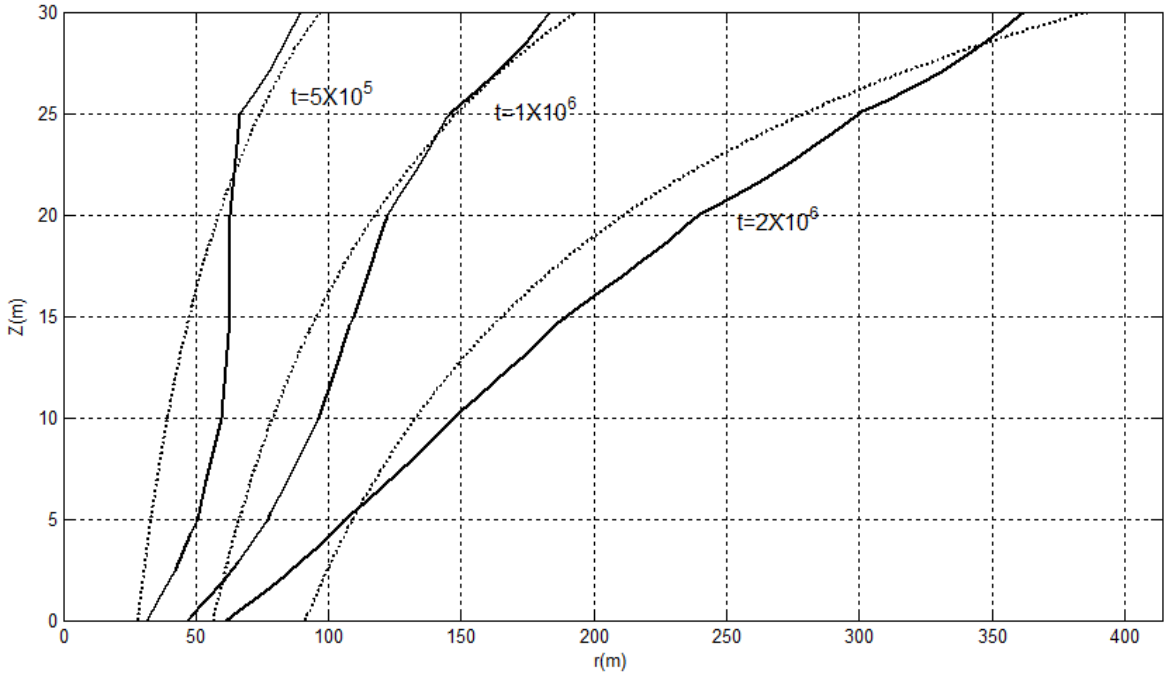

Fig 3-9 A comparison between numerical and analytical solutions for late time injection from a horizontal well. Numerical results (solid lines) come from a self-developed FEM model where compressibility is assumed to be zero.

Table 3-7 Characteristics of fluids and formation

Q (mass rate) $\frac{kg}{s\,m}$	**Q (volumetric rate)** $\frac{m^2}{s}$	**P base** ***(Mpa)***	$\frac{\mu_w}{\mu_{co_2}}$	**K** m^2	**P_{cm}** Pa	**T** $C°$
$3.67x10^{-4}$	$4.5x10^{-5}$	*15*	*10.3*	10^{-13}	9×10^4	*50*

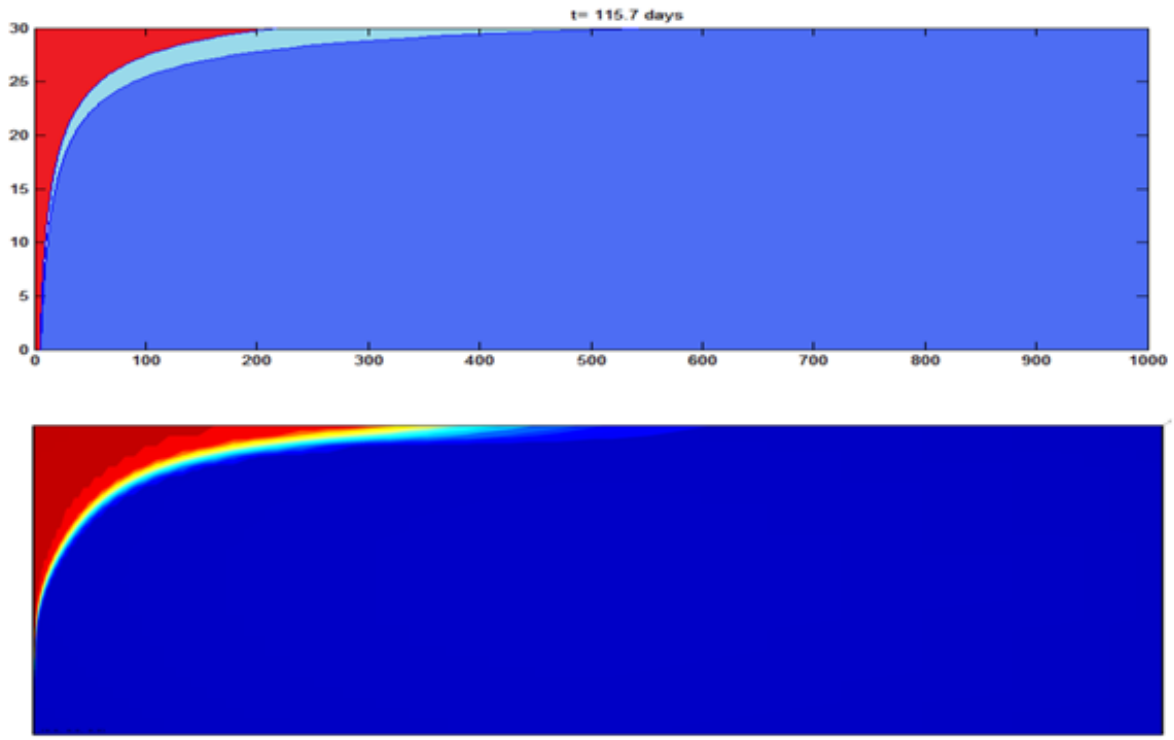

Fig 3-10 A comparison between analytical (top) and numerical (bottom) solutions for early-time injection. Numerical results are from TOUGH2 ECO2N (Pruess K 2007) , and although the compressibility is non-zero in their numerical model, the generated pressure in the well zone is not very different from hydrostatic pressure, and therefore the effect of compressibility is not significant.

3.3.2.2.1 Conclusion and Discussion:

In this part an analytical framework is presented for the position of isosats for a non-wetting injectant of a density different from that of the wetting phase which originally saturated the homogeneous porous medium. Previous analytic solutions were not capable of including the transitional zone for the injectant ($0 < S < 1$). To achieve this solution, assumptions are made that are similar to those made by others (linear approximations for relative permeability, small capillary number…). The new solution gives the location of any isosat at any time in a direct manner.

Although numerical models provide a reasonable approximation for the saturation distribution and are more flexible for different boundary conditions and geometries, they cannot provide a rapid and reasonable approximation for long time periods. In stochastic analysis, many realizations must be computed, and rapid estimates of the system state at long

times are needed, hence numerical models become expensive and time-consuming, even if the number of elements (nodes) is modest. The new analytical solutions provide immediate solutions for the isosat distribution for any time, and can therefore be easily incorporated into stochastic assessments.

The analytical solutions also provide a qualitative assessment of the results of commercial numerical models which generally function as a "black box", and allow comparison to the results of different numerical models. Parametric assessment is also facilitated, in that the new analytical solutions can quickly provide an assessment of the sensitivity of the solution to the set of physical parameters (density, viscosity, permeability, porosity…) used in the equations. For instance, the importance of relative permeability functions or viscosity ratios can be readily obtained, and it is apparent that this is a challenging task for a numerical model, particularly for late-time assessment.

This analytical model provides a good approximation for the fastest breakthrough time of the injected gas during a primary drainage process. Based on the analytical solution, formulation of different isosats is provided but the exact solution of the isosats is not known. This issue will be addressed elsewhere.

The agreements between analytical and numerical results are better in the plane flow geometry, partly because the analytical results in the second case are linear instead of being curved. The main deficiency of this method is that the analytical scheme is limited to only one type of Leverett-J function.

Progression of gravity-drainage front in the plane flow geometry is much faster than axisymmetric case, and that results in a much faster growth of the transition zone compared to the axisymmetric case. This has important practical applications for potential acceleration of CO_2 dissolution into the aqueous phase.

3.4 Arbitrary Leverett-J function:

To make the assumption of the analytical solutions more robust, another analytical scheme is developed here. This method uses the Buckley-Leveret solution for primary drainage as an approximation of the vertically averaged saturation. A fitting function was used to correlate vertically averaged saturation with saturation on the top of the aquifer and, by the help of the vertical equilibrium assumption, the saturation distribution is obtained. Assuming negligible vertical velocity, the pressure has radial and gravitational parts expressed as

$$P_w = p_w(r) - \gamma_w z \tag{3.56}$$
$$P_n = p_n(r) - \gamma_n z \tag{3.57}$$

And therefore, for the capillary pressure

$$P_c = P_c^{top}(r) + \Delta\gamma z \tag{3.58}$$

Eq. (3.59) represents the distribution of capillary pressure in the domain, and it is decomposed into radial and vertical parts. The vertical part of the capillary pressure is linear because of the hydrostatic pressure distribution of multiphase flow.

$$\begin{cases} k_{rw} = S_e \\ k_{rg} = b(1 - S_e) \end{cases} \tag{3.59}$$

$$P_c = AS^{-1} = \frac{A}{1 - S_r}\left(S_e + \frac{S_r}{1 - S_r}\right)^{-1} \tag{3.60}$$

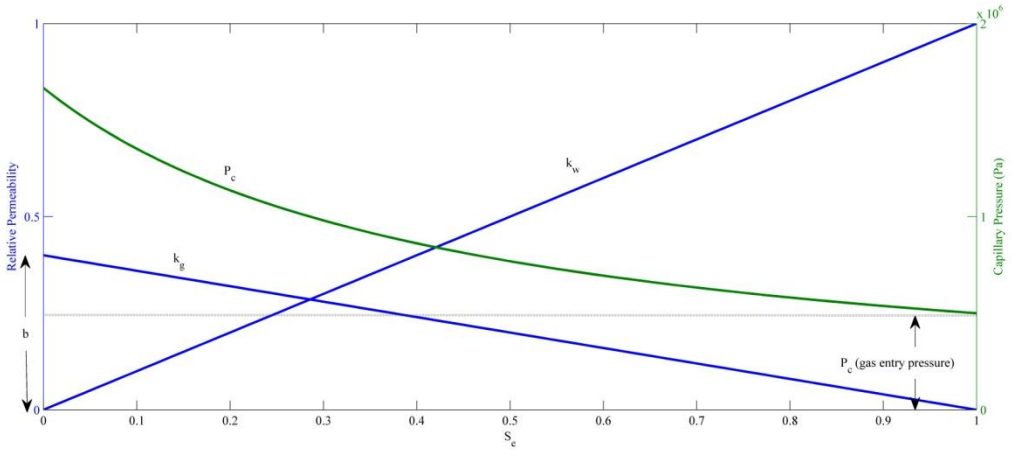

Fig 3-11 Relative permeability functions and Leverett-J function versus the effective saturation.

Here, A is gas entry capillary pressure and b is the maximum mobility of gas flow. Saturation at the top of the aquifer is not known, but a good approximation of the vertically averaged saturation can be obtained from the Buckley-Leverett equation. The capillary term is neglected in the hyperbolic equation, and that makes it impossible to introduce the boundary condition effects at the injector interface. However, it is shown in Fig. (3.13) that the solution of the hyperbolic equation is a good approximation of the precise solution of the convective-diffusive equation.

To obtain the saturation distribution on top of the aquifer, a fitting function with one degree of freedom is used. A pseudo-analytical function is assumed to present the correlation between vertically averaged saturation ($\tilde{S}_e$) and saturation on the top of the aquifer(S_e^{top}). In the rest of the formulation, S represents the effective saturation and the subscript is dropped.

$$S^{top} = \frac{e^{m\tilde{S}} - 1}{e^{m} - 1} \tag{3.61}$$

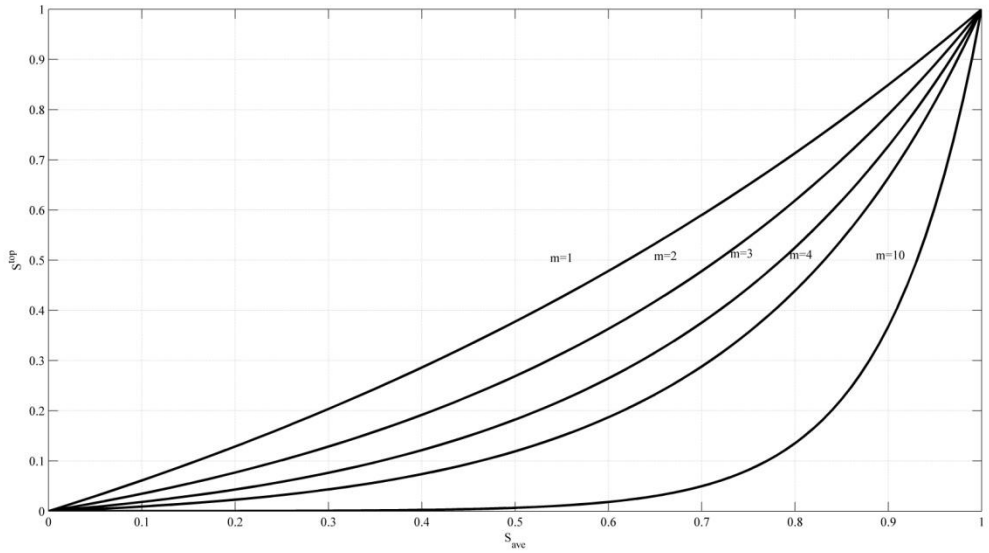

Fig 3-12 Fitting functions for correlation between average saturation and the saturation on the top of the aquifer. Different values of m provide a wide range of curvatures to approximate the correlation between S^{top} and S_{ave}.

There is no physical basis for Eq. (3.61), and any monotonically increasing fitting function with similar values at the boundaries can be used. In the other words, Eq. (3.61) represents an approximated relationship between vertically averaged saturation and the saturation on top of the aquifer. The value of m gives different curvatures to the formulation, but in all cases the formulation remains monotonically increasing and its values for (S=0 and S=1) are fixed. By substituting Eq. (3.61) in the mass conservation equation, different values of m result in different errors, and the minimum error case is obtained from the best fitted approximation. This simple mathematical approach provides a reasonably precise approximation for calculation of the fate of the injectant. Capillary pressure on the top of aquifer is obtained by

$$P_c^{top} = P_c\left(\frac{e^{m\tilde{S}}-1}{e^m-1}\right) = \frac{A}{1-S_r}\left(\frac{e^{m\tilde{S}}-1}{e^m-1}+\frac{S_r}{1-S_r}\right)^{-1} \tag{3.62}$$

And by assuming hydrostatic capillary pressure distribution in the vertical direction

$$P_c = P_c^{top} - \Delta\gamma(B-z) = \frac{A}{1-S_r}\left(\frac{e^{m\tilde{S}}-1}{e^m-1}+\frac{S_r}{1-S_r}\right)^{-1} - \Delta\gamma(B-z) \tag{3.63}$$

Eq. (3.63) is a global capillary pressure function, but the parameter m should be optimized for minimal error. The position of isosats can be derived from Eq. (3.63), and the position of isosat S=1 represents the outer boundary of the transition zone, and allows the breakthrough time of the gas to be estimated for that distance. The position of the interface of the transition zone is called b (from the bottom of the aquifer) and is equivalent to

$$b = B + \frac{A}{\Delta\gamma(1-S_r)}\left[(1-S_r) - \left(\frac{e^{m\tilde{S}}-1}{e^m-1}+\frac{S_r}{1-S_r}\right)^{-1}\right] \tag{3.64}$$

And by averaging the saturation in vertical dimension

$$\tilde{S} \approx \frac{1}{B}\left[\int_0^b dz + \int_b^B \left\{\frac{A}{\left(\frac{A}{1-S_r}\left(\frac{e^{m\tilde{S}}-1}{e^1-1}+\frac{S_r}{1-S_r}\right)^{-1} - \Delta\gamma(B-z)\right)(1-S_r)} - \frac{S_r}{1-S_r}\right\} dz\right] \tag{3.65}$$

To simplify the formulation, it is more convenient to define a new parameter similar to Eq. (3.65).

$$Q(\tilde{S}) = \frac{A}{1-S_r}\left(\frac{e^{m\tilde{S}}-1}{e^1-1}+\frac{S_r}{1-S_r}\right)^{-1} \tag{3.66}$$

Interestingly, an analytical integration of Eq. (3.65) is available

$$\tilde{\bar{S}} \approx \frac{1}{B}\left[\int_0^b dz + \int_b^B \left\{\frac{A}{\left(Q\left(\bar{\bar{S}}\right) - \Delta\gamma\left(B - z\right)\right)\left(1 - S_r\right)} - \frac{S_r}{1 - S_r}\right\} dz\right] =$$

$$\frac{1}{B}\left[b + \frac{A}{\left(1 - S_r\right)\Delta\gamma}\ln\left(\Delta\gamma z - \Delta\gamma B + Q\left(\bar{\bar{S}}\right)\right)\Big|_b^B - \left(\frac{S_r}{1 - S_r}\right)\left(B - b\right)\right] \tag{3.67}$$

$$\tilde{\bar{S}} \approx \frac{1}{B}\left[b - \left(\frac{S_r}{1 - S_r}\right)\left(B - b\right) + \frac{A}{\left(1 - S_r\right)\Delta\gamma}\ln\left(\frac{Q\left(\bar{\bar{S}}\right)}{\Delta\gamma\left(b - B\right) + Q\left(\bar{\bar{S}}\right)}\right)\right] \tag{3.68}$$

Eventually, by substituting Eq. (3.64) and Eq. (3.68) in Eq(3.69), the value of m can be optimized

$$Q_o t = \int_0^{r_m} 2\pi\left(B - b\right)\left(1 - \tilde{\bar{S}}\right) r dr \tag{3.69}$$

The value of $\tilde{\bar{S}}$ can be obtained by lowering the dimension of the problem. By employing a linear relative permeability relationship and averaging over the entire height of the aquifer, the two-dimensional problem is reduced to a one-dimensional problem.

By using the formulation obtained for the value of vertically averaged saturation in an axisymmetric geometry from the previous section

$$\tilde{\bar{S}} = \begin{cases} 0 & r < \sqrt{\dfrac{Q_o t}{m\pi\varphi\left(1 - S_r\right)}} \\ \dfrac{m}{m-1} - \dfrac{1}{m-1}\sqrt{\dfrac{mQ_o t}{r^2\left(1 - s_r\right)\pi\varphi}} & \sqrt{\dfrac{Q_o t}{m\pi\varphi\left(1 - S_r\right)}} < r < \sqrt{\dfrac{mQ_o t}{\pi\varphi\left(1 - S_r\right)}} \\ 1 & r > \sqrt{\dfrac{mQ_o t}{\pi\varphi\left(1 - S_r\right)}} \end{cases} \tag{3.70}$$

And for plane flow geometry

$$\tilde{S}=\begin{cases}0 & r<\dfrac{Q_o t}{m\varphi(1-S_r)}\\ \dfrac{m}{m-1}-\dfrac{1}{m-1}\sqrt{\dfrac{mQ_o t}{r(1-s_r)\varphi}} & \dfrac{Q_o t}{m\varphi(1-S_r)}<r<\dfrac{mQ_o t}{\varphi(1-S_r)}\\ 1 & r>\dfrac{mQ_o t}{\varphi(1-S_r)}\end{cases} \tag{3.71}$$

Table 3-8 Characteristics of primary injection of less viscous, less dense injectant into a water-wet saturated zone, linear relative permeability functions with S_r=0.3 are chosen.

$Q_{o(volumetric)}$ (m^2/sec)	$P_{(base)}$ (MPa)	K (m^2)	m = $\frac{\mu_w}{\mu_n}$	φ	S_r	P_{cm}(Pa)	t (year)
0.00009	**15**	**10^{-14}**	**19.3**	**0.3**	**0.3**	**5×10^5**	**1**

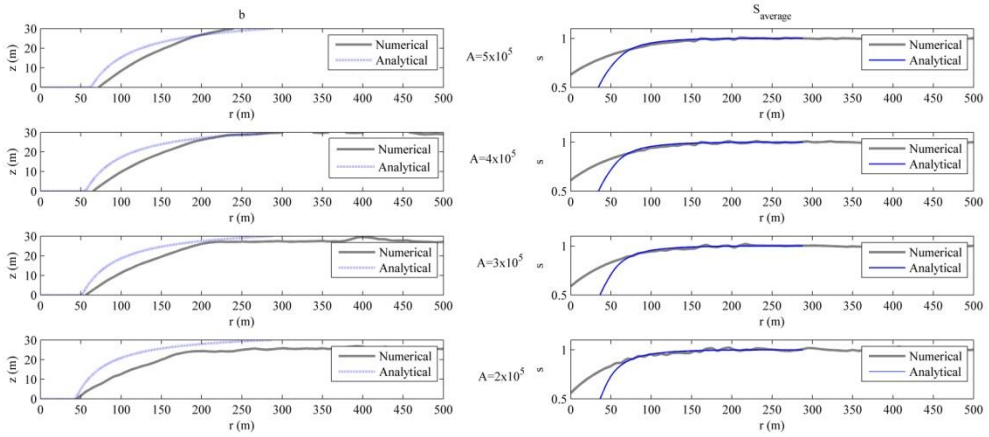

Fig 3-13 A comparison between analytical and numerical results using a fitting function approach for a set of linear relative permeabilities for an axisymmetric geometry. Right-hand figures represent the saturation contour of S=1 and the left ones are the vertically averaged saturation.

Table 3-9 Characteristics of primary injection of less viscous, less dense injectant into a water-wet saturated zone, linear relative permeability functions in plane flow conditions

$Q_{o(volumetric)}$ (m^2/sec)	$P_{(base)}$ (MPa)	K(m^2)	m = $\frac{\mu_w}{\mu_n}$	φ	S_r	P_{cm}(Pa)	t (year)
$5x10^{-4}$	**10**	**10^{-14}**	**19.3**	**0.3**	**0.3**	**1×10^5**	**1**

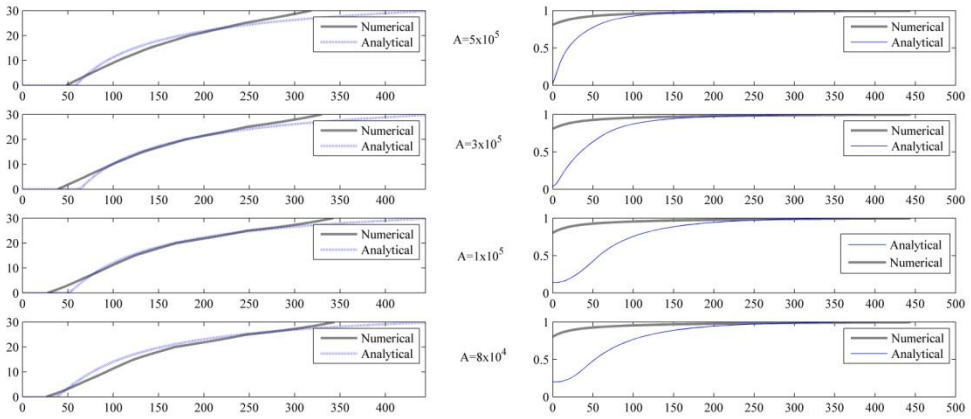

Fig 3-14 A comparison between analytical and numerical results using the fitting function approach for a set of linear relative permeabilities for a plane flow geometry. Right-hand figures represent the saturation contour of S=1 and the left-hand ones are the vertically averaged saturation.

Table 3-10 Characteristics of primary injection of less viscous, less dense injectant into a water-wet saturated zone, linear relative permeability functions.

$Q_{o(volumetric)}$ (m^2/sec)	$P_{(base)}$ (MPa)	$K_{(m2)}$	$m = \frac{\mu_w}{\mu_n}$	φ	S_r	T (year)
0.0009	10	10^{-14}	19.3	0.3	0.3	5

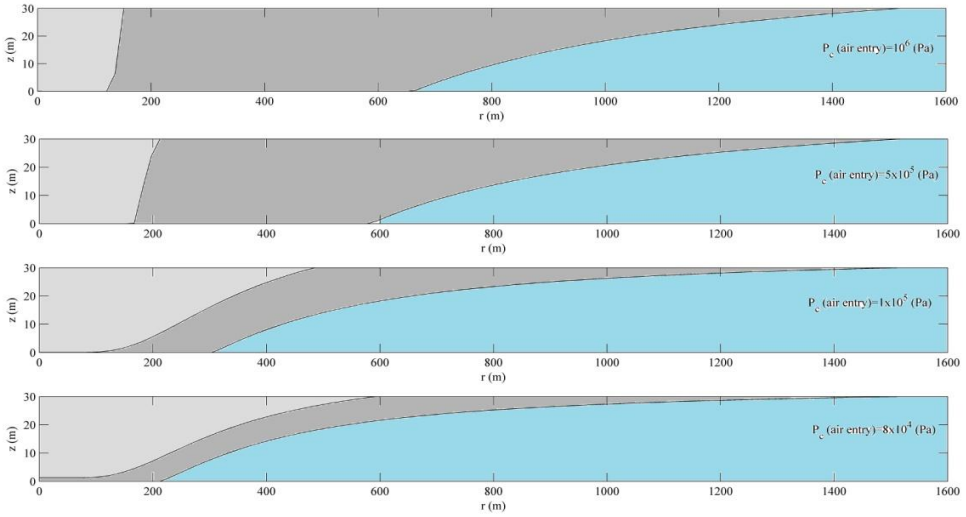

Fig 3-15 saturation distribution snap shots for different values of gas entry capillary pressure. For a low value of gas entry pressure, the size of the transition zone approaches zero for small values of A.

3.4.1 Discussion and Conclusion:

In the second analytical approach, a series of analytical fitting function makes it possible to use different Leverett-J functions. For simplicity, a simple Corey Leverett-J function is chosen here, though others could be used

$$P_c = AS^{-1} \tag{3.72}$$

This analytical result provides better agreement with the numerical solution, and also provides a quick and powerful tool to incorporate the effect of the Leverett-J function and the value of gas entry capillary pressure to calculate the size of the transition zone. It is clear from Fig. (3.15) that a small capillary pressure (large grain size) results in a sharp interface. In other words, the sharp interface assumption that has been used several times in the literature is only valid when the capillary pressure is small enough.

Similar to the first approach, the agreement between analytical and numerical results in plane flow conditions is better than in axisymmetric flow. Also, the effect of capillary pressure in the Buckley-Leverett function is neglected, and that results in discrepancies in the average saturation results. (Right-hand figures in Fig. (3.13) and Fig. (3.14)) Values of vertically averaged saturation for axisymmetric and plane flow geometries are obtained from a hyperbolic equation, and the capillary term is neglected. Approximating the primary drainage formulation with a single hyperbolic equation causes error in the values of saturation especially in the zone close to the boundary (close to the injector).

Linear relative permeability values lead to a poor representation of the physically correct properties of the displacement and fingering phenomena. Another analytical method is developed that incorporates the nonlinearity of the relative permeability functions and it will be discussed in Chapter 4.

Engineering applications of the derived analytical and semi-analytical tools are better estimation of fate of the injected gas during and after injection, developing a quantitative prediction tool for simulation of gaseous rich zone position and effect of different aquifer's characteristics on the shape of the plume. Most important contribution of the solutions here is formulating the effect of capillary gas entry pressure on the size of transition zone. Larger transition zone provides faster dissolution of gas in saline. Parametric analysis of gaseous progression during injection is another interesting application of the developed model.

4 Method of characteristics for primary gravity drainage

4.1 Introduction:

Each geologic formation has an intrinsic volumetric storage capacity (volume × porosity) and may possess singular advantages or deficiencies for disposal or sequestration, depending on geological context, the physical nature of the formation and bounding strata, geographical location, and so on. An ideal formation for CO_2 sequestration is a permeable stratum with high and fully interconnected porosity, overlain and perhaps laterally bounded by impermeable and non-reactive rock to prevent escape in pure or dissolved forms. Such seals might be salt, non-fractured anhydrite, and even shale if there are no chemical interactions with the minerals in the shale or shrinkage caused by replacement of the water phase by supercritical CO_2. Reservoir capacity, cap rock quality, and target stratum permeability are considered to be the major parameters in evaluation of formations for injection. Factors such as depth, thickness, dip, heterogeneity and other properties also play important roles in target selection (78).

The analytical basis of the governing equation for flow used here is the generalized Darcy's law, a continuum-based constitutive law (44) linking pressure gradient, rock and fluid properties, and flow velocities. In the generalized Darcy's equation, the distributions of saturation and pressure in two-phase fluid flow are linked to phenomenological relations including relative permeability functions and Leverett-J functions, as well as the intrinsic properties of the fluids and rock (mainly permeabilities, viscosities, densities, compressibilities and accessible porosity). By substitution of the constitutive relations into the statement of mass conservation of fluids, the governing equations based on the primary unknowns may be derived.

Numerical methods provide approximate solutions for the set of governing equations, and they are flexible enough to permit accommodation of different properties, boundary conditions and geometries. However, analytical solutions for simple geometries and linearized cases have great value for quick estimation of the results at very long times, for verification of numerical models, and for simple inverse solutions. In stochastic analyses involving parametric variability, such as a Monte Carlo simulation for a long period of injection for example, it becomes necessary to execute the calculations many times, and even a simple numerical model with time-stepping may display inordinately lengthy execution times in such cases. An analytical solution that almost instantaneously gives results at any stipulated time may be a key aspect of such simulations, and might also be combined with mathematical models that can account for aspects of spatial heterogeneity impossible to address analytically. Finally, we note that in an analytical model, meaningful qualitative and quantitative insight into the formulation and different possible mechanisms is straightforward and uncomplicated.

Analytical treatment of the transition zone is complicated and little has been achieved for realistic conditions. For one-dimensional and cylindrical geometries, the Buckley-Leverett solution was developed (37)(21)(77) by assuming a negligibly small capillary term. Neglecting the capillary term in gravity drainage process may be unrealistic in many cases and diminishes the size of the transition zone. However, this solution can be extended to any arbitrary shape of isosat, and by forcing the shape of isosat to the general mass conservation equation, a hyperbolic governing equation can be recovered and characteristics of the saturation distribution in the case of significant capillary pressure are obtained.

A precise analytical formulation of isosat positions is complicated if not impossible for strongly non-linear cases, but if the relative permeabilities are taken to be linear, an approximation is possible. Linear relative permeability functions is an over-simplification

and may not suit many real physical problems, but for coarse-grained or intensely fractured media (where fracture flow dominates), capillary effects are small, and a linear set of relative permeability functions is a reasonable approximation. Linearization of the Leverett-J function results in excessive error, but by using a local linearization scheme, the error is minimized, and then a discretized analytical method can be applied to transform the non-linear governing equation into a series of linear equations in small intervals of saturation. It turns out that in cases of massive CO_2 sequestration, excellent reservoir conditions usually conform to modest or low capillarity effects (high permeability), therefore these approximations are robust in such cases. Nevertheless, it is contingent upon the user of the new solutions developed here to assure that the assumptions are appropriate for specific cases.

First, a generalized formulation for mass conservation of two incompressible and immiscible fluids in a homogeneous porous medium is derived. This is based on the analytical formulation of isosats, and the obtained formulation of isosats from in Chapter 3 when a third-order polynomial Leverett-J function is assumed to be the case, is forced to obey mass conservation. Consequently, the equation is reduced to a one-dimensional hyperbolic PDE. The isosats are time-dependent, and thus the transient term of the mass conservation equations vanishes and the equation is transformed to a one-dimensional boundary-value problem for which the single boundary condition comes from the position of the outset isosat. The analytical results of the equation are compared to the numerical model. The local linearization of the Leverett-J function and the numerical discretization of the governing equations are explained in Chapter 3 and Appendix A respectively.

4.2 Formulation:

To derive the governing equations for propagation of a saturation front from an arbitrary injection source, a mass conservation equation over an isosat is written. If λ_w and λ_n are the wetting and nonwetting mobilities, γ_n and γ_w are the specific weights of wetting and

nonwetting fluids, u_w and u_n are the Darcian velocities of wetting and nonwetting phases, and Q_o is the injection rate per meter of perforation for a continuously perforated wellbore, then

By rewriting the general mass conservation equation that is independent from geometry and by introducing Q_o as the volumetric source injection and $h = \frac{K_y}{K_x}$ as the heterogeneity ratio

$$\bar{u}_w = -\frac{k_{rw}}{\mu_w}\begin{bmatrix} K_x & 0 \\ 0 & K_y \end{bmatrix}\nabla p_w - \frac{k_{rw}}{\mu_w}\gamma_w\begin{bmatrix} K_x & 0 \\ 0 & K_y \end{bmatrix}\cdot\bar{e}_y \tag{4.1}$$

$$\bar{u}_n = -\frac{k_{rn}}{\mu_n}\begin{bmatrix} K_x & 0 \\ 0 & K_y \end{bmatrix}\nabla p_n - \frac{k_{rn}}{\mu_n}\gamma_n\begin{bmatrix} K_x & 0 \\ 0 & K_y \end{bmatrix}\cdot\bar{e}_y \tag{4.2}$$

$$\nabla\cdot\bar{u}_w = \frac{\varphi\partial S}{\partial t} \tag{4.3}$$

$$\bar{u}_t = \bar{u}_w + \bar{u}_n = \begin{bmatrix} K_x & 0 \\ 0 & K_y \end{bmatrix}\left(-\frac{k_{rw}}{\mu_w}\nabla p_w - \frac{k_{rn}}{\mu_n}\nabla p_n - \left(\frac{k_{rw}}{\mu_w}\gamma_w + \frac{k_{rn}}{\mu_n}\gamma_n\right)\bar{e}_y\right) \tag{4.4}$$

$$\oint_\Gamma \bar{u}_t.\bar{n} = Q_o \tag{4.5}$$

Eq. (4.3) is based on an assumption of constant formation porosity and fluid densities. Generally, gas and supercritical liquids are not incompressible, but since pressure and temperature remain approximately constant during injection, the compressive volume change is not significant and an incompressible assumption is reasonable. By introducing P as

$$P = F(S)p_w + (1-F(S))p_n - \int_s^1 p_c(S)F'(S)ds \tag{4.6}$$

Eq. (4.4) can be written as

$$\bar{u}_t = -\begin{bmatrix} K_x & 0 \\ 0 & K_y \end{bmatrix}\left[\left(\frac{k_{rw}}{\mu_w} + \frac{k_{rn}}{\mu_n}\right)\nabla P + \left(\frac{k_{rw}}{\mu_w}\gamma_w + \frac{k_{rn}}{\mu_n}\gamma_n\right)\bar{e}_y\right] \tag{4.7}$$

If Γ is chosen as an isosat, the fluid mobilities remain constant over Γ, which makes it possible to bring them out of the integral, although at this point the positions of the isosat

curves are not yet determined, though we assume them to be static and of arbitrary shape. By introducing fractional phase flow

$$F(S)=\frac{k_{rw}}{k_{rw}+mk_{rn}} \tag{4.8}$$

And, substituting Eq. (4.6) into Eq. (4.7), we obtain

$$F(S)Q_o=\begin{bmatrix}K_x & 0\\ 0 & K_y\end{bmatrix}\left[\oint_\Gamma -\frac{k_{rw}}{\mu_w}\nabla P\cdot\bar{n}-\oint_\Gamma F(s)\left(\frac{k_{rw}}{\mu_w}\gamma_w+\frac{k_{rn}}{\mu_n}\gamma_n\right)\bar{e}_y\cdot\bar{n}\right] \tag{4.9}$$

$$F(S)Q_o=\begin{bmatrix}K_x & 0\\ 0 & K_y\end{bmatrix}\left[\begin{array}{l}\oint_\Gamma -\frac{k_{rw}}{\mu_w}\nabla p_w\cdot\bar{n}-\oint_\Gamma \frac{k_{rw}}{\mu_w}\gamma_w\bar{e}_y\cdot\bar{n}-\oint_\Gamma \frac{k_{rw}k_{rn}}{\mu_n(k_{rw}+mk_{rn})}\nabla p_c\cdot\bar{n}\\ +\oint_\Gamma \frac{k_{rw}}{\mu_w}\gamma_w\bar{e}_y\cdot\bar{n}-\oint_\Gamma F(S)\left(\frac{k_{rw}}{\mu_w}\gamma_w+\frac{k_{rn}}{\mu_n}\gamma_n\right)\bar{e}_y\cdot\bar{n}\end{array}\right] \tag{4.10}$$

$$\oint_\Gamma \frac{F(S)Q_o\bar{n}\cdot\bar{n}}{AR(\Gamma)}=\begin{bmatrix}K_x & 0\\ 0 & K_y\end{bmatrix}\left[\begin{array}{l}\oint_\Gamma\left(-\frac{k_{rw}}{\mu_w}\nabla p_w-\frac{k_{rw}}{\mu_w}\gamma_w\bar{e}_y\right)\cdot\bar{n}-\\ \oint_\Gamma \frac{k_{rw}k_{rn}}{\mu_n(k_{rw}+mk_{rn})}\nabla p_c\cdot\bar{n}-\oint_\Gamma \frac{k_{rn}}{\mu_n}F(S)(\gamma_n-\gamma_w)\bar{e}_y\cdot\bar{n}\end{array}\right] \tag{4.11}$$

AR stands for the area of the isosat (Γ) around the injection well, if the isosat Γ be closed curve, and the last term in Eq. (4.11) vanishes so that

$$\oint_\Gamma k_{rn}F(S)\,(\gamma_n-\gamma_w)\bar{e}_y\cdot\bar{n}=k_{rn}F(S)\Delta\gamma\oint_\Gamma \bar{e}_y\cdot\bar{n}=0 \tag{4.12}$$

It should be considered that closed isosats are only the case for free space (no-boundary condition geometry). In the interesting case of semi-infinite space, Eq (4.12) is not applicable and the last term of Eq (4.11) cannot be neglected. By the help of the divergence theorem

$$\int_{\Omega}\nabla\cdot\left(\frac{F(S)Q_o\bar{n}}{AR(\Gamma)}\right)=\int_{\Omega}\nabla\cdot\bar{u}_w-\begin{bmatrix}K_x & 0\\ 0 & K_y\end{bmatrix}\begin{bmatrix}\int_{\Omega}\nabla\cdot\left(\frac{k_{rn}k_{rw}}{\mu_n(k_{rn}+mk_{rw})}\nabla p_c\right)\\ -\oint_{\Omega}\nabla.\left(\frac{k_{rn}}{\mu_n}F(S)(\gamma_n-\gamma_w)\bar{e}_y\right)\end{bmatrix} \tag{4.13}$$

Similarly to the mass conservation relationship for the wetting phase (Eq. 4.3), it is possible to rewrite Eq. (4.13) as

$$\int_{\Omega}\nabla\cdot\left(\frac{F(S)Q_o\bar{n}}{AR(\Gamma)}\right)=\int_{\Omega}\frac{\varphi\partial S}{\partial t}-\begin{bmatrix}K_x & 0\\ 0 & K_y\end{bmatrix}\begin{bmatrix}\int_{\Omega}\nabla\cdot\left(\frac{k_{rn}k_{rw}}{\mu_n(k_{rn}+k_{rw})}\nabla p_c\right)\\ +\int_{\Omega}\nabla.\left(\frac{k_{rn}}{\mu_n}F(S)(\gamma_n-\gamma_w)\bar{e}_y\right)\end{bmatrix} \tag{4.14}$$

And in a general way

$$\nabla\cdot\left(\underbrace{\frac{F(S)Q_o\bar{n}}{AR(\Gamma)\varphi}}_{Visouse}+\underbrace{\frac{K_yk_{rn}F(S)\Delta\gamma\bar{e}_y}{\mu_n\varphi}}_{Buoyancy}+\underbrace{K_xk_{rn}F(S)\frac{p_c'(S)}{\mu_n\varphi}\begin{bmatrix}1 & 0\\ 0 & h\end{bmatrix}\nabla S}_{Capillary}\right)=\frac{\partial S}{\partial t} \tag{4.15}$$

Normalization:

By normalizing Eq (4.15) similar to

$$X=\frac{x}{L}\qquad Y=\frac{y}{L}\qquad P_m^*=\frac{p_m}{\Delta p}$$

$$T=\frac{K\Delta pt}{\mu_wL^2}=\frac{u_ot}{L}\quad P_c=\alpha\cos(\theta)\left(\varphi/K\right)^{1/2}J(S)$$

$$u_o=\frac{Q_o}{L}=\frac{K\Delta p}{\mu_nL}\qquad t=\frac{L^2\mu_n}{K\Delta p}T$$

By using normalized variables

$$\nabla\cdot\left(\underbrace{\frac{F(S)Q_o\bar{n}}{AR(\Gamma)\varphi}}_{Visouse}+\underbrace{\frac{K_y k_{rn}F(S)\Delta\gamma\bar{e}_y}{\mu_n\varphi}}_{Buoyancy}+\underbrace{K_x k_{rn}F(S)\frac{p_c'(S)}{\mu_n\varphi}\begin{bmatrix}1&0\\0&h\end{bmatrix}\nabla S}_{Capillary}\right)=\frac{\partial S}{\partial t} \tag{4.16}$$

$$\nabla^*\cdot\left(\begin{array}{l}\underbrace{\frac{K_x\Delta p}{\varphi\mu_n L^2}\frac{F(S)\bar{n}}{AR^*}}_{Visouse}+\underbrace{\frac{K_y\Delta\gamma}{L\mu_n\varphi}k_{rn}F(S)\bar{e}_y}_{Buoyancy}+\\ \frac{K_x\alpha\cos(\theta)\sqrt{\frac{\varphi}{K_x}}}{L^2\mu_n\varphi}\underbrace{k_{rn}F(S)J'(S)\begin{bmatrix}1&0\\0&h\end{bmatrix}\nabla^*S}_{Capillary}\end{array}\right)=\frac{K_x\Delta p}{L^2\mu_n}\frac{\partial S}{\partial T}$$

$$\nabla^*\cdot\left(\frac{1}{\varphi}\frac{F(S)\bar{n}}{AR^*}+\underbrace{\frac{hL\Delta\gamma}{\Delta p\varphi}}_{\varepsilon_1}k_{rn}F(S)\bar{e}_y+\underbrace{\frac{\alpha\cos(\theta)\sqrt{\frac{\varphi}{K_x}}}{\Delta p\varphi}}_{\varepsilon_2}k_{rn}F(S)J'(S)\begin{bmatrix}1&0\\0&h\end{bmatrix}\nabla^*S\right)=\frac{\partial S}{\partial T}$$

$$\nabla^*\cdot\left(\frac{1}{\varphi}\frac{F(S)\bar{n}}{AR^*}+\underbrace{\frac{K_y L\Delta\gamma}{Q_o\mu_n\varphi}}_{\varepsilon_1}k_{rn}F(S)\bar{e}_y+\underbrace{\frac{\alpha\cos(\theta)\sqrt{\frac{K_x}{\varphi}}}{Q_o\mu_n}}_{\varepsilon_2}k_{rn}F(S)J'(S)\begin{bmatrix}1&0\\0&h\end{bmatrix}\nabla^*S\right)=\frac{\partial S}{\partial T}$$

And value of capillary term is equal to

$$\varepsilon_1=\frac{\alpha\cos(\theta)\sqrt{\frac{K_x}{\varphi}}}{Q_o\mu_n} \tag{4.17}$$

$$\varepsilon_2=\frac{K_y L\Delta\gamma}{Q_o\mu_n\varphi} \tag{4.18}$$

Dimensionless numbers, ε_1 and ε_2 indicate the ratio of buoyancy force and viscous forces and capillary and capillary force and viscous force respectively.

For typical values of $K_x=10^{-13}$ (m^2), $K_y=10^{-14}$ (m^2), $Q_o=10^{-1}$ (m^2/sec), $\mu_n=10^{-5}$(Pa.sec), $\Delta\gamma=3000$ (N/m^3), $\Phi=0.1$ and $\alpha\cos(\theta)=10^{-2}$ (N/m) then $\varepsilon_1=0.01$ and $\varepsilon_2=3\times10^{-4}$ L. It has been widely accepted that ε_2 is small enough for typical range of injection and reservoir

characteristics. But interestingly ε_1 depends on L, and ε_1 is not an intensive parameter. In the other words, importance of buoyancy force can be different depends on the characteristic length. Characteristic length of the buoyancy force for aquifer in vertical thickness, and that is generally small. But for very thick aquifers or leakage problem when the plum has already escaped from the sealing formation (cap rock), the buoyancy force is the importance drive and dominant mechanism. Vertical equilibrium is not applicable for this important case. By skipping the capillary term , Eq (18) turns into

$$\nabla^* \cdot \left(\frac{1}{\varphi} \frac{F(S)\bar{n}}{AR^*} + \varepsilon_1 k_{rn} F(S) \bar{e}_y \right) = \frac{\partial S}{\partial T} \tag{4.19}$$

In this discussion, equations are stated in their intrinsic dimensions and they are not normalized. Eq. (4.19) is a first-order hyperbolic differential equation in three dimensions. It is the generalized form of the Buckley-Leverett equation, and by the help of method of characteristics the solution is obtainable. Also in the aquifer scale, value of ε_2 is small and the buoyancy term can be neglected. It appears not to be possible to solve Eq. (4.19) in its current form.

During injection, an evolving network of isosats and flowsats is generated. Contours of saturation represent the isosat positions which evolve as a family of non-intersecting curves. This will be proved for a homogeneous porous medium with linear relative permeability and locally linearized Leverett J-function. The gradient of the saturation represents the normal velocity of the flux of the initial saturating phase, and we call this a flowsat, defined as the curve with maximum saturation variation with distance, and therefore normal to the isosats. Flowsats are integral curves of saturation flux, not the gaseous or saline phase velocity; therefore they are different from streamlines. In a general case, it is possible to define the

isosat and flowsat families, η and ξ, which stand for curves, by transforming an axisymmetric geometry to a curvilinear orthogonal coordinate system with the orthogonal bases as

$$\bar{e}_\theta = \frac{\nabla \theta}{h_\theta} \tag{4.20}$$

$$\bar{e}_\eta = \frac{\nabla \eta}{h_\eta} \tag{4.21}$$

$$\bar{e}_\xi = \frac{\nabla \xi}{h_\xi} \tag{4.22}$$

Here, η, ξ and θ in an axisymmetric geometry or η, ξ and z in a plane flow direction are surfaces with constant scalar value. Rewriting Eq. (4.19) in this coordinate system gives

$$\frac{\partial}{h_\xi h_\eta h_\theta \partial \eta}\left(\frac{h_\theta h_\xi F(S) Q_o}{AR(\Gamma)\varphi}\right) = \frac{\partial S_{(\xi,\eta)}}{\partial t} \tag{4.23}$$

h_ξ, h_η and h_θ are the scale factors of different dimensions and we can define the area of a general isosat surrounding the injection region through double integration

$$AR(\Gamma) = \int_{\theta_0}^{\theta_1}\int_{\xi_0}^{\xi_1} h_\theta h_\xi d\xi d\theta = f(\eta) \tag{4.24}$$

For axisymmetric radial injection from a vertical fully penetrating line source, $h_\theta = r = f(\eta, \xi)$, which is independent of θ, so it comes out of the integral, but the other spatial variable ξ remains. By choosing a narrow range for ξ and cancelling terms, Eq. (4.24) is approximated as

$$AR(\Gamma) = 2\pi r \int_{\xi_0}^{\xi_1} h_\theta h_\xi d\xi \approx 2\pi r \Delta\xi h_\theta h_\xi \Big|_{\xi=\frac{\xi_1+\xi_2}{2}} \tag{4.25}$$

$$\Delta\xi = \xi_1 - \xi_0 \tag{4.26}$$

For axisymmetric geometry

$$AR(\Gamma) = \int_{\xi_0}^{\xi_1} h_\xi d\xi \approx \Delta\xi h_\xi \Big|_{\xi=\frac{\xi_1+\xi_2}{2}} \tag{4.27}$$

$$\Delta\xi = \xi_1 - \xi_0 \tag{4.28}$$

For plane-flow geometry, by substituting Eq. (4.25) in Eq. (4.23)

$$\frac{\partial}{\partial\psi}\left(\frac{F(S)HQ_o}{\Delta\xi\varphi}\right) = \frac{\partial s}{\partial t} \quad for \quad \xi\in[\xi_0,\xi_1] \;\; \theta\in(-\pi,\pi]\,\eta\in R \tag{4.29}$$

$$-\frac{F(S)HQ_o}{\varphi\Delta\xi^2}\frac{\partial\Delta\xi}{\partial\psi} + \frac{F'(S)HQ_o}{\varphi\Delta\xi}\frac{\partial S}{\partial\psi} = \frac{\partial S}{\partial t} \tag{4.30}$$

$$\psi = \int h_\theta h_\xi h_\eta d\eta \;\Big|_{\xi=\frac{1}{\xi_0+\xi_1}} = \psi(\eta) \tag{4.31}$$

In an axisymmetric geometry, it is possible to prove that the first term of Eq. (4.30) is much smaller than the second one and it is thus possible to neglect the first term (see Chapter 5). By skipping the first term, Eq. (4.30) becomes similar to the classic Buckley-Leverett equation (37), but with a different spatial similarity variable. The positions of the isosats and integral curves are not trivially stipulated, but in the next section, we show how the position of the isosats can be obtained analytically. For linear relative permeability functions (e.g. strictly convex fractional flow function), Eq. (4.30) is solved as

$$\frac{\psi(\eta)}{t} = \frac{F'(s)Q_o}{\varphi} \qquad \xi\in[\xi_0,\xi_1] \;\; \theta\in[-\pi,\pi] \;\; \eta\in R \tag{4.32}$$

Eq. (4.32) is the self-similar solution for the governing hyperbolic equation, Eq. (4.32), in the case of convexity of the fractional flow function. For a one-dimensional geometry, $\psi(\eta) = x$ and the Buckley-Leverett relationship for a linear set of relative permeability functions is recovered. For a cylindrical geometry, $\psi(\eta) = cr^2$ (77)(21), and for a spherical symmetric geometry $\psi(\eta) = cr^3$ (21) (where c is a constant). Derivation of Eq. (4.32) is the mathematical proof of the discontinuity of saturation profile close to the value of Sc. Using the mathematical presentation of the isosats' formulations from Chapter 3 and substituting them into Eq. (4.32), an analytical solution is possible.

$$\frac{F\left(S_{\eta^+}\right)-F\left(S_{\eta^-}\right)}{S_{\eta^+}-S_{\eta^-}}=F'\left(S_{\eta^-}\right) \tag{4.33}$$

$$S_{\eta^+}=1 \tag{4.34}$$

$$F\left(S_{\eta^+}\right)=1 \tag{4.35}$$

Nonlinearity of the relative permeability must be treated by some other means, but for a linear set of relative permeability functions, it is possible to assume $S_c = S_{\eta+} = 1$.

4.2.1 Axisymmetric Geometry:

Using the derived analytical formulation from Chapter 3, the position of isosats for vertical penetrating well injection into a tabular flat aquifer is derived as (see chapter 3)

$$\eta=\frac{E_{(t)}^{S^*}}{r}+Bz \tag{4.36}$$

$$E^{s^*}=\frac{A_{S^*}}{m-1}\sqrt{\frac{mQ_o t}{(1-S_r)\pi\varphi}} \tag{4.37}$$

$$B=\Delta\gamma \tag{4.38}$$

Eq. (4.36) provides a time-dependent basis for Eq. (4.29); in other words, the value of saturation is only a function of η, and η itself is a function of r,z,ɵ and t. Consequently

$$\frac{\partial S_{(\eta)}}{\partial t} = 0 \tag{4.39}$$

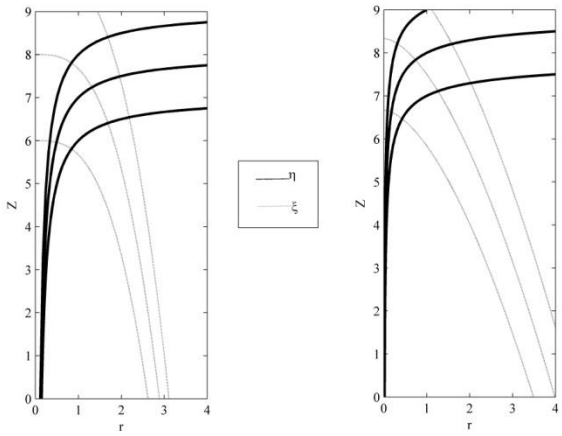

Fig 4-1 ***a: Saturation flow network in axisymmetric geometry; blue curves are isosats, red lines are flowsats, and*** $\eta = \frac{E^{s^*}_{(t)}}{r} + Bz$ ***and*** $\xi = \frac{r^3}{3E^{s^*}_{(t)}} + \frac{z}{B}$***. 3) b: Saturation flow network in plane flow geometry; blue curves are isosats, red lines are flowsats, and*** $\eta = \frac{E^{s^*}_{(t)}}{\sqrt{r}} + Bz$ ***and*** $\xi = \frac{6r^{\frac{5}{3}}}{5E^{s^*}_{(t)}} + \frac{z}{B}$

With the help of Eq. (4.39), Eq. (4.29) reduces to a steady-state equation in (η-ξ) space.

$$\frac{\partial}{\partial \eta}\left(\frac{F(S)Q_o}{\Delta \xi \varphi}\right) = 0 \tag{4.40}$$

This simplifies the problem because the analytical solution for Eq. (4.40), a first-order differential, is simple. The external boundary condition for Eq. (4.40) is derived in Chapter 3 and first by integrating Eq. (4.40), then by applying the boundary condition, the value of the integration constant is stipulated, and the solution of S for each value of η is derived.

$$\frac{F(S)Q_o}{\Delta \xi \varphi} = C \tag{4.41}$$

The boundary condition for Eq. (4.40) comes from

$$\eta_{S=1} = \eta_1 \tag{4.42}$$

and by imposing this, C is derived as

$$\frac{F(s)Q_o}{\Delta\xi\varphi} = \frac{F(1)Q_o}{\Delta\xi|_{\eta_1}\varphi} \tag{4.43}$$

And, by using further straightforward simplifications, Eq. (4.43) becomes

$$F(s) = \frac{\Delta\xi(\eta)}{\Delta\xi(\eta_1)} \tag{4.44}$$

Eq. (4.44) is an algebraic equation and the solution is direct. The value of η_1 for the axisymmetric geometry is constant and the relationship between S and η can be obtained accordingly. Eq. (4.44) can be adapted for any saturation. The value of η for each saturation is derived and the result thus provides an analytical relation between η and S. Eq. (4.43) can be derived from a simpler method, through applying direct mass conservation in a differential interval of η. According to Fig (4.2), the amount of water that goes into the gray zone must also come out because the saturation inside the gray area is constant, and the water content of the zone is also constant.

In Fig (4.2) the gray zone is the infinitesimal zone between $[\eta_0, \eta_1]$ and by writing mass conservation for this area Eq. (4.41) is recovered. Because the saturation inside the zone is constant over time, the water content variation is zero, therefore the mass conservation is reduced to

$$\oint_{\Gamma_1} \frac{q_{w1} \bullet \bar{n}}{AR(\Gamma_1)} = \oint_{\Gamma_2} \frac{q_{w2} \bullet \bar{n}}{AR(\Gamma_2)} \tag{4.45}$$

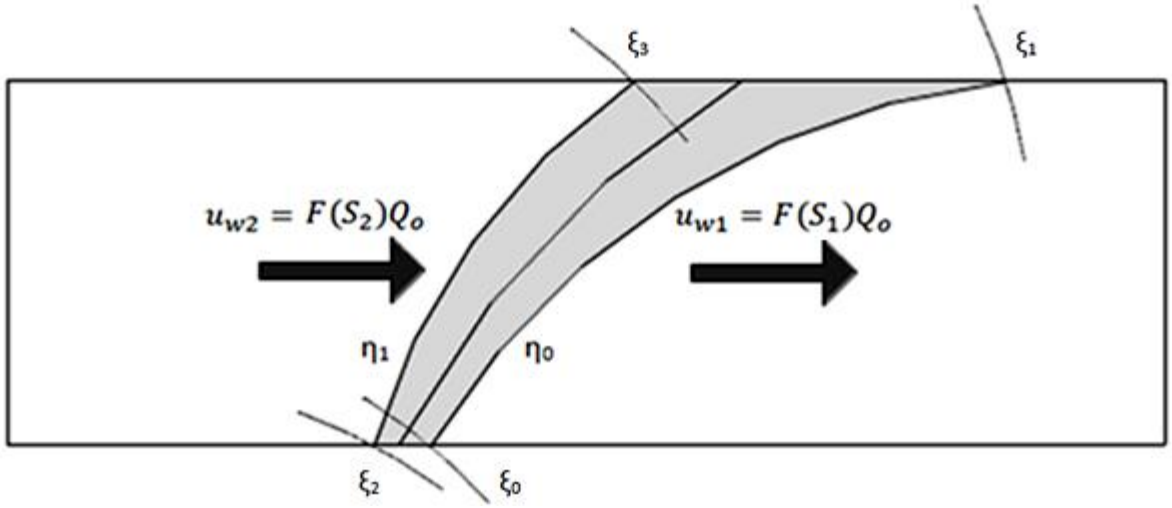

Fig 4-2 Mass conservation applied to an infinitesimal zone between two isosats, the saturation remains constant because the coordinate system is moving.

And by substitution of Eq (4.24) in Eq (4.45), and transforming the coordinate system from (x,y,z) to (η,ξ,θ), it becomes

$$\frac{F(S_1)h_\theta h_\xi}{2\pi \int_{\xi_0}^{\xi_1} h_\theta h_\xi d\xi} = \frac{F(S_2)h_\theta h_\xi}{2\pi \int_{\xi_2}^{\xi_3} h_\theta h_\xi d\xi} \Rightarrow \frac{F(S_1)}{(\xi_1 - \xi_0)} = \frac{F(S_2)}{(\xi_3 - \xi_2)} \tag{4.46}$$

Eq (4.46) is equivalent to Eq. (4.43).

4.2.2 Discretized Analytical Solution:

Es* is a function of saturation, and consequently Eq. (4.36) is not the collection of non-intersecting family of curves. In order to define Eq. (4.43) in the new coordinate system, the basis of the coordinate system should be independent of S*.

The coordinate system is defined based on two parameters, S* and t and the coordinate system is named H(S*,t) with bases of

$$\text{Basis of } H_{(S^*,t)} = \left(\frac{\nabla\eta}{|\nabla\eta|}, \frac{\nabla\xi}{|\nabla\xi|}\right)$$

Superscript indicates the value of saturation that the coordinate system (or Es*) is based on, and subscript is the value of η corresponding to the saturation. The value $\eta_{S=S^*}$ in $H_{(S^*,t)}$ can be written as $\eta_{S^*}^{(S^*,t)}$, specifying the isosat of S*. By perturbing the value of S from S* to S*-ΔS, the value of $\eta_{S=S^*-\Delta S}^{(S^*,t)}$ is derived from Eq. (4.43). By having the isosat of $\eta_{S=S^*-\Delta S}$ at t in $H_{(S^*,t)}$, the maximum radius is readily obtained. Now the global coordinate system is transformed to $H_{(S^*-\Delta S,t)}$ and the value of $\eta_{S^*-\Delta S}^{(S^*-\Delta S,t)}$ is obtained based on the assumption of $r_{max\,(S^*-\Delta S)}^{S^*} = r_{max\,(S^*-\Delta S)}^{S^*-\Delta S}$ (Fig (4.3)). In a similar manner, this procedure can be repeated for $S = S^* - 2\Delta s$ and so on so that the positions of isosats for other saturations are obtained. This progressive scheme for treatment of nonlinearity of the coefficient matrix is reported in the literature (22), and now it is applied to the coordinate system so that the isosat position and the coordinate system are simultaneously updated.

There are several sources of error, starting from the vertical equilibrium assumption that approximates the shape of isosat, to Eq. (4.24), and finally the discretization scheme. However, the analytical solution captures the trend of the isosat variations, and the positions of contours of different saturations at different times are rapidly obtainable. This scheme therefore provides a fast and robust method for quantification of the position of isosats for a linear set of relative permeability functions.

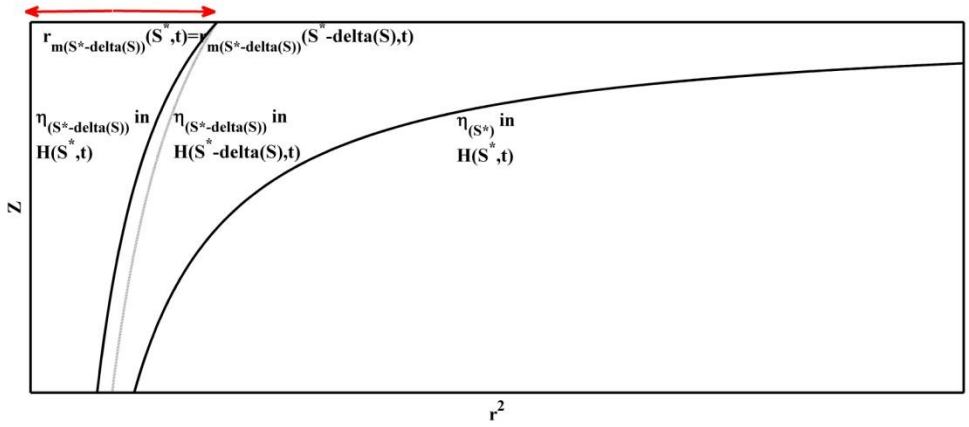

Fig 4-3 Schematic presentation of different isosats in different coordinate system.

4.3 Analytical and numerical results:

In order to compare analytical and numerical results, a simple axisymmetric injection model is developed here. The isosats for different saturations are derived and compared with the analytical results. The agreement is reasonable in Fig (4.4-a) and Fig (4.4-b), and also in Fig. (4.4-c), although the numerical result shows a fluctuation which comes from the convective instability of the model. In the numerical method, an upstream weighting function has (79) been used to stabilize the result. By applying an artificially large capillary pressure to the numerical method, or other stabilizing schemes like Upwind Petrov-Galerkin methods, the numerical stability of the results improves but accuracy is thereby reduced.

Fig. (4.5) contains snapshots of different saturation contours at different times in an axisymmetric geometry. Expansion of the saturation contour in time is apparent, which is equivalent to the faster progression of the higher saturation isosats, which is essentially the expansion of the transition zone. Characteristics of the aquifer and fluids are in Table 4.1.

Table 4-1 Properties of reservoir and injection for numerical model of primary drainage in axisymmetric condition

Q_o (m^3/s)	$P_{(base)}$ MPa	K (m^2)	$m = \frac{\mu_w}{\mu_n}$	φ	S_r	P_{cm} (Pa)	T (°C)
0.0015	10	10^{-14}	19.3	0.1	0	1×10^5	50

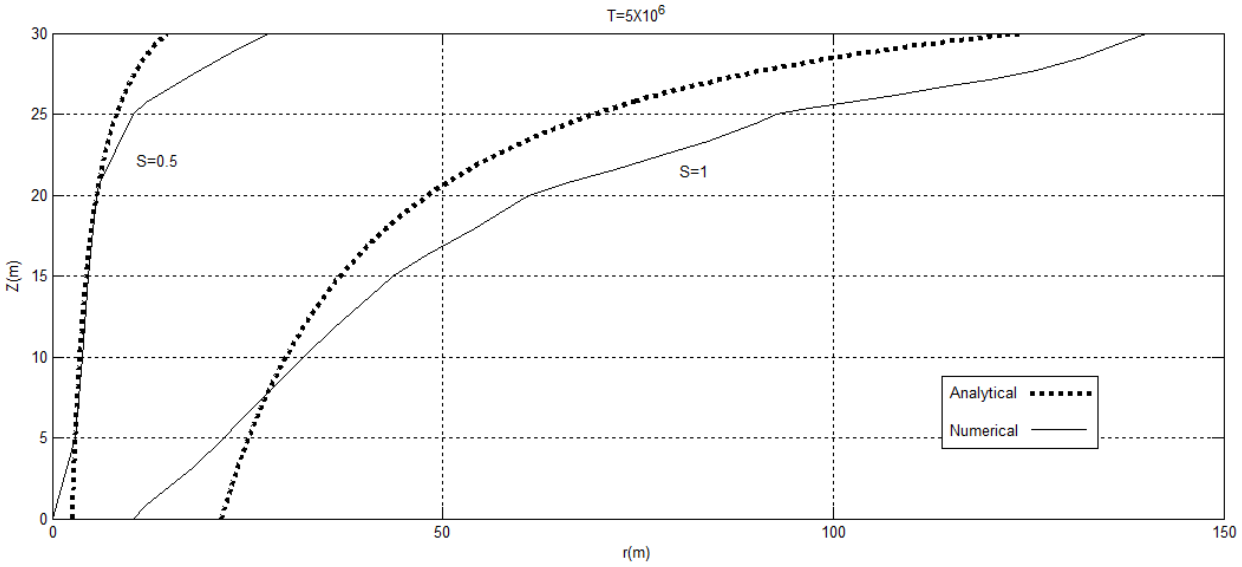

Fig (4.4-a)

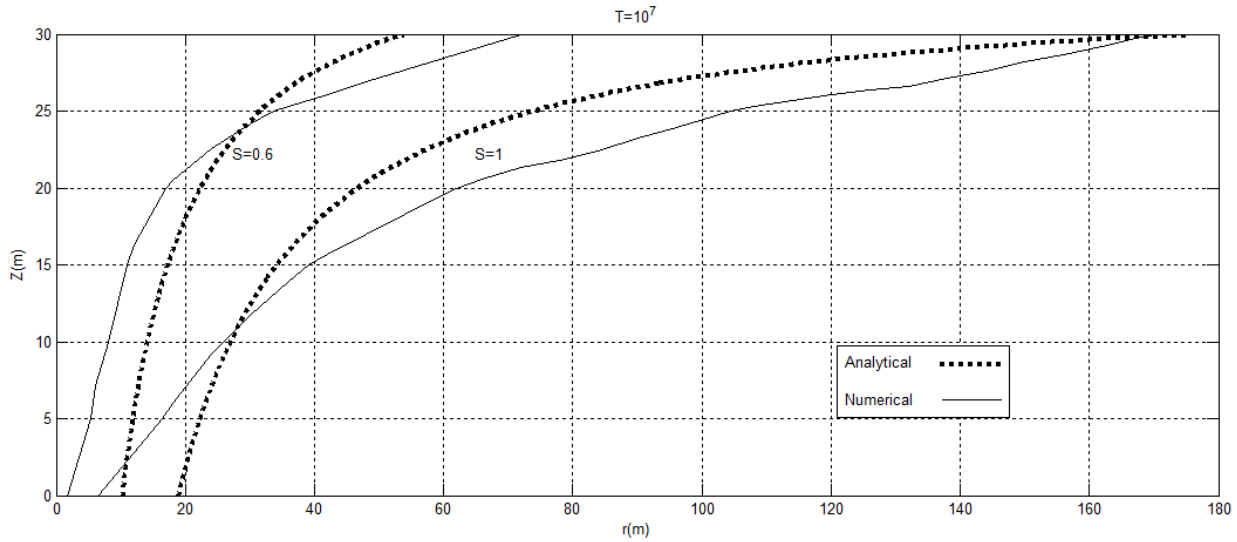

Fig (4.4-b)

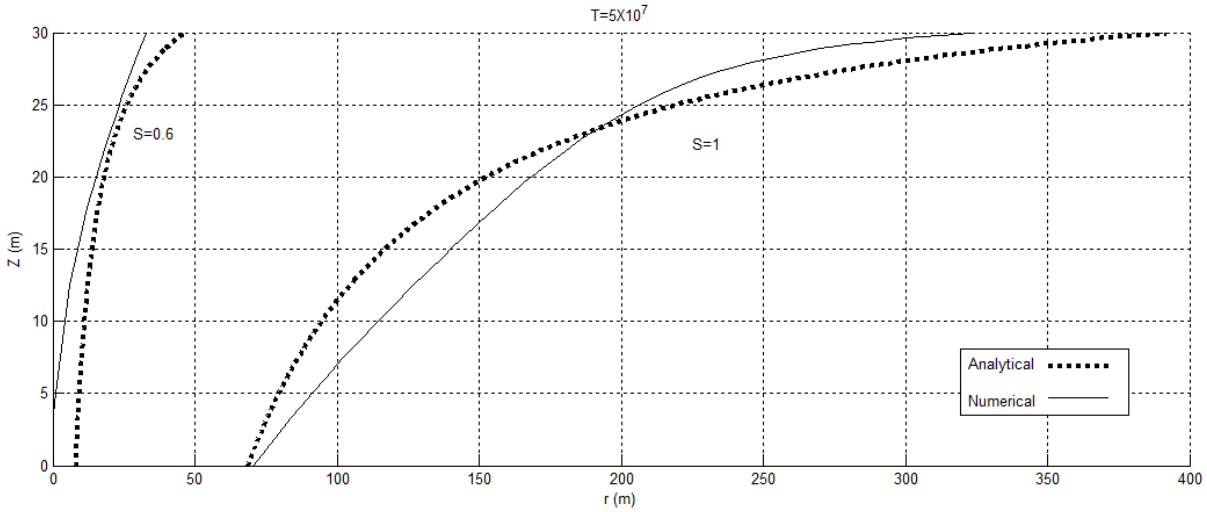

Fig 4-4 Comparison of analytical and numerical results of saturation distribution at different times. Capillary pressure has been included to maintain numerical stability

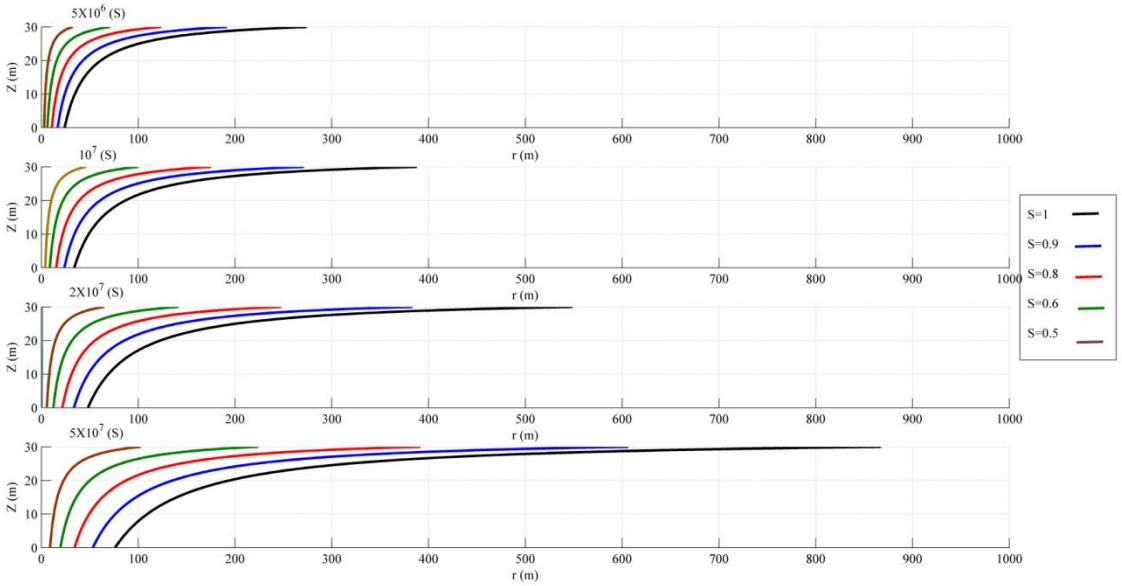

Fig 4-5 Isosat progression for different injection times; snapshots of saturation distribution at four different times.

4.4 Nonlinear relative permeability:

An analytical position for isosats (η) has been derived only for systems with linear relative permeability functions. For nonlinear relative permeability systems, considered to be more practical cases, the position of isosats is not known. Therefore, the applicability of the solution in its current form is limited.

Here, another possibility is presented that makes the solution more general and adoptable for cases involving nonlinear relative permeabilities. Examining Eq (4.19), one may note that there are five variables (r, z, t, AR, S). By introducing the maximum radius of the injected plume in each elevation (z) and time (t) as another variable here, r_m (z,t), the number of variables are increased to six. It should be considered that r_m is the radius of the gas-water interface (i.e., the isosat corresponding to S=1) for any elevation and time. Consequently, r_m is a function of z and t. Now, AR can be directly written as a function of r_m;

$$AR = \int_0^B 2\pi r_m(z,t)dz \tag{4.47}$$

Therefore, r_m provides a similarity variable that is a function of z and t, and AR is a function of r_m. Consequently, the number of variables is reduced to 4, including (r_m, r, t, s). Using the Buckingham Pi theorem, the number of variables is n = 4 and number of fundamental dimensions is m = 2 ([L] , [T]). It is possible to define two (n-m=2) dimensionless numbers that are functions of each other. Introducing

$$\pi_1 = \frac{r}{r_m} \qquad \pi_2 = S$$

And introducing a relationship

$$\frac{r}{r_m} = I(S) \tag{4.48}$$

And noting that an isosat can be directly defined as

$$\frac{r}{r_m} = c \tag{4.49}$$

The position of isosats and flowsats can be obtained as

$$\eta = \frac{r}{r_m} \rightarrow \nabla\eta = \begin{pmatrix} \frac{1}{r_m} & -\frac{rr_{m,z}}{r_m^2} \end{pmatrix} \tag{4.50}$$

$$\nabla\eta.\nabla\xi = 0 \rightarrow \nabla\xi = \begin{pmatrix} r_m & \frac{r_m^2}{rr_{m,z}} \end{pmatrix} \rightarrow \xi = r\,r_m + \int \frac{r_m^2}{rr_{m,z}} dz \tag{4.51}$$

Eq (4.51) provides a reasonable formulation for the position of isosats and flowsats. If r_m is known, by using Eq (4.43), the position of an isosat for any value of saturation for an arbitrary relative permeability function is obtained. A derivation of r_m for nonlinear relative permeabilities and arbitrary Leverett-J functions will be discussed in greater detail in the next chapter.

4.5 Conclusions:

An approximate solution for the position of the isosaturation contours (isosats) has been developed and verified for the case of an immiscible phase of different density being injected into a porous medium that is saturated and wet by another fluid phase of higher viscosity. This solution represents an important advance in the class of Buckley-Leverett problems because now the development and evolution of the transition zone of saturations can be explored in an analytical manner for several simple geometries (e.g. axisymmetric vertical well injection and late-time long horizontal well injection). This will allow "quick-look" assessments of various geological cases, partial verification of numerical schemes (providing the assumptions are honored, such as phase incompressibility), and stochastic analysis of parametric variations (although not spatially non-homogeneous distributions of properties).

A major engineering application of the analytical solution developed here is quantifying the dimensionless number to estimate the contribution of different effective forces for different geometries and characteristics. Understanding the physical behavior in different conditions and formations is an important part of the problem, and these aspects of relative importance of different processes are far more easily obtained by using first-order dimensionless numbers

than by laborious repeated mathematical modeling. Formulating of the position of different isosats may not be as important as simulation of the position of the interface, but still provides a thorough understanding of behavior of the transition zone, and can lead to better estimates of the rate of dissolution of the CO_2 into the saline water phase.

The following assumptions were made in developing the solution, and the reader is counseled to assure that the solution is not mis-applied by using it in conditions for which it is not appropriate (e.g. highly non-linear relative permeability functions, high capillary entry pressures, strong heterogeneity…):

- The relative permeabilities of the two phases are reasonably approximated by straight lines.
- The fluids are treated as incompressible because the solution is for approximately constant pressure injection.
- Vertical pressure distribution is hydrostatic and dominant flow is horizontal

5 Prediction of interface position during primary drainage and secondary imbibition in nonlinear relative permeability system

5.1 Introduction:

During continuous injection of a lighter immiscible phase, viscosity and density contrasts lead to growth of a saturation transition zone as well as gravity override of the injectate. In Chapter 2 and Chapter 3, the position and formulation of the isosats (contours of saturation) were semi-analytically quantified based on assumptions of immiscibility, vertical equilibrium and incompressibility of the host liquid and injectate. These assumptions have been widely accepted by others and form the basis of previous works addressing this class of problems in analytic or semi-analytic terms. A linear set of relative permeability functions was also assumed, but this tends to oversimplify the problem, making solutions applicable only to specific types of formations where capillary pressure during injection is very small. Herein, solutions are developed to accommodate any arbitrary set of relative permeability functions. The effect of relative permeability non-linearity is not negligible and if the continuous trail behind the shock is incorporated correctly, and the evolution of the two-phase zone between the drained and intact zones requires significant capillary pressure, the degree of nonlinearity becomes important. To show this, in Fig. (5.1) different degrees of nonlinearity are applied to a numerical solution, and the saturation distributions indeed are quite different. In these examples, residual saturation for the primary drainage process is considered to be zero to better illustrate the difference in the saturation progression.

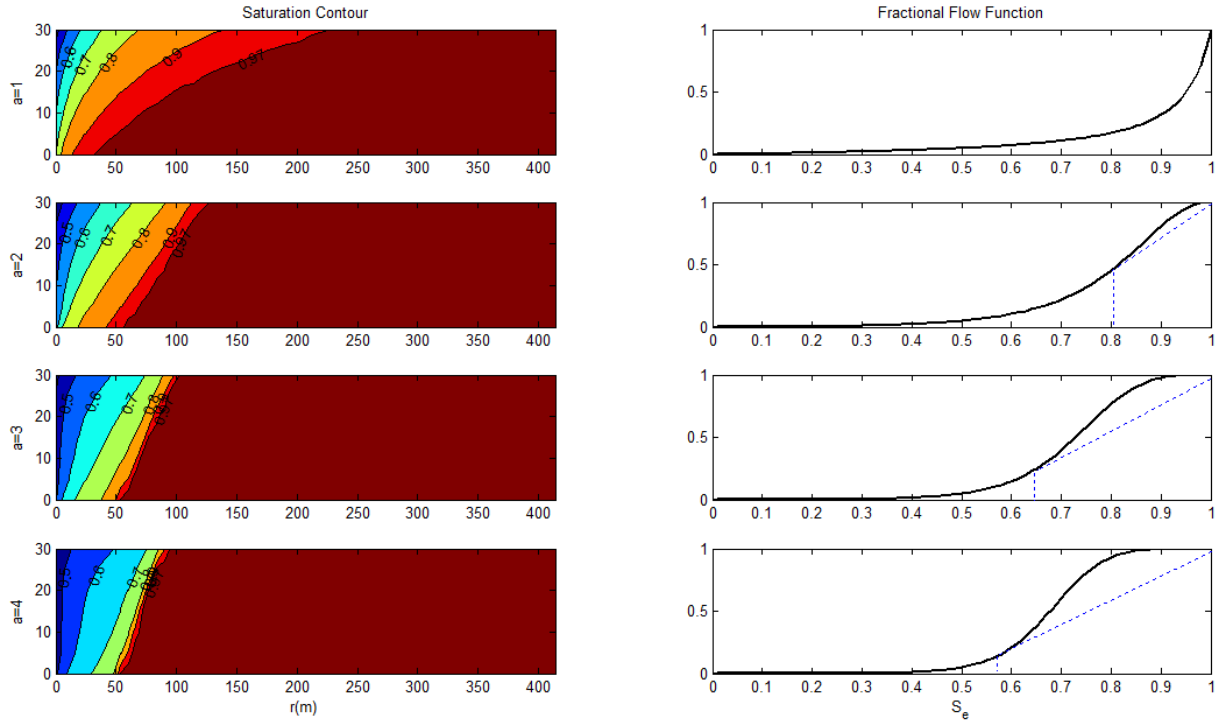

Fig 5-1 Typical relative permeability functions for primary drainage process are approximated as $k_{rw}=S_e^a$ and $k_{rn}=\beta\ (1-S_e)^a$, and different values of a represents different degrees of nonlinearity. Saturation progression has been shown for β=1 and α=1-4.

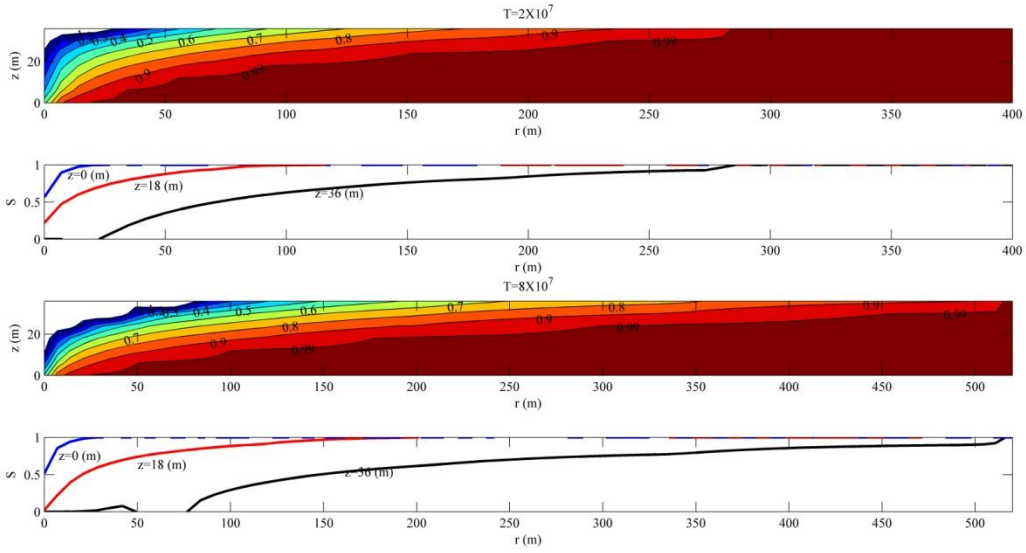

Fig 5-2 Numerical results of saturation progression at different times and profile of different values of S at different depths

In this approach, a semi-analytical solution is developed to quantify the position of the shock waves for different degrees of nonlinearity (values of a), and since only primary drainage is of interest in this article, a typical formulation for relative permeability functions suits reasonably well.

The effect of gravity and the different hydrostatic pressure (gravity head) distributions of columns of fluids of different density complicate the pattern of saturation progression during injection. Injection of a gas (or a lighter supercritical fluid or a solvent) into a water-saturated formation is called “primary drainage”, and the density contrast generates a vertical capillary pressure effect. The vertical part of capillary pressure is assumed to be constant and equal to $\Delta\gamma = \gamma_w - \gamma_n$, an assumption stipulated from the vertical equilibrium assumption of fluids and the condition of negligible vertical velocity (which is realistic for large-scale rapid injection into tabular flat-lying reservoirs). The vertical equilibrium assumption has been discussed and justified several times (62),(80). The vertical part of the capillary pressure associated with a radial capillary pressure calculated as the vertically averaged saturation leads to wedge-shaped contours of equal saturation (isosats). Lateral progression of the non-wetting phase saturation is faster on the top compared to the bottom because of the lower initial pore pressure of the host fluid on the top of the aquifer arising from the different hydrostatic pressure distributions. Formulation of the positions of the isosats is necessary for two-dimensional analytical solutions for the saturation in the transition zone. Combining the radial and the vertical parts of capillary pressure, a global functional for the capillary function is obtained and stipulation of the capillary pressure contours, which are equivalent to the saturation contours, then becomes possible.

In a confined horizontal tabular formation, the injectant invades the pore space and pushes the host wetting liquid away from the injection zone. In this case, the ratio of viscosities is a

key parameter in estimating the size of the transition zone. Nordbotten et al. (61),(56),(52) derived an analytical solution assuming a sharp interface between the host liquid and the trailing completely drained zone and the total gas content at any radius is lumped only at the top of the aquifer. Juanes et al. (57) extended this solution to a secondary imbibition process and estimated the magnitude of the residual trapping mechanism for the host fluid. Sloping aquifers (inclined geometries) and the effect of a capillary fringe were studied in later works (52),(49). Although the residual saturation in the fully drained zone is incorporated in the solution procedure, because of the sharp interface assumption the influence of relative permeability functions are totally neglected.

5.2 Formulation:

Lemma I: In an axisymmetric geometry, the structure and domain of the saturation transition waves (shock or rarefaction) in the presence of gravity is similar to gravity-free condition, but the spatial amplitude of the waves is scaled differently.

Proof: Although the proposition sounds trivial, and has been mentioned in the literature (e.g. (41)), a rigorous proof apparently has not been provided. Here a generalized mass conservation equation is stipulated, using the basic generalized Darcy's law, to derive the hyperbolic equation for mass conservation for any arbitrary isosat (contour of constant saturation). By using simple isosat curves like a flat line or a cylinder, the classic Buckley-Leverett equation for 1D and cylindrical flow is recovered. Starting from Eq (4.27) of Chapter 4

$$\frac{1}{\psi(r,z,t)}\left(-\frac{\Delta\xi_{,r}\,F(S)Q_o}{\varphi\Delta\xi^2}+\frac{1}{\Delta\xi}\left(\frac{F(S)Q_o}{\varphi}\right)_{,r}\right)=\frac{\partial S}{\partial t} \tag{5.1}$$

As stated above, the precise expressions for η and ξ are not determined, but if one assumes that their formulation can be developed as a perturbation of the base case with linear relative

permeability functions, scaling of Eq. (5.1) is possible. For a linear set of relative permeability functions, $\eta = \alpha(\frac{A}{r} + Bz)$ and $\xi = O(\frac{r^3}{3A})$ (see Chapter 3), consequently

$$\frac{\Delta\xi_{,r}}{\Delta\xi^2} = O\left(\frac{1}{r^4}\right) \tag{5.2}$$

$$\frac{1}{\Delta\xi} = O\left(\frac{1}{r^3}\right) \tag{5.3}$$

Because the first term of Eq. (5.1) is much smaller than the second term, it is possible to ignore it and rewrite Eq. (5.1) as

$$\frac{1}{\Lambda_{(r,z)}}\frac{\partial}{\partial r}\left(\frac{F(S)Q_o}{\varphi}\right) = \frac{\partial}{\partial\Omega}\left(\frac{F(S)Q_o}{\varphi}\right) = \frac{\partial S}{\partial t} \tag{5.4}$$

$$\Omega_{(r,z)} = \int_{r_w}^{r} \Lambda_{(\tau,z)} d\tau \tag{5.5}$$

Eq. (5.4) is a hyperbolic equation and the F(S) function determines the structure of the saturation transition waves which is identical to the gravity-free case. The spatial similarity variable is different and imposes different spatial amplitude to the transition waves, but as stated in Lemma 1, the domain of the waves is similar.

The similarity solution can be defined as

$$\Pi_{(r,z,t)} = \frac{\Omega}{t} = \frac{F'(S)Q_o}{\varphi} \tag{5.6}$$

A direct solution of Eq. (5.4) is not possible because an analytical form for Λ is not available. Based on the expected behavior of the solution and dimensions of variables, a separation of variables is proposed as

$$\Pi_{(r,z,t)} = \Pi_{\left(a=\frac{r}{r_{m(z,t)}}\right)} \tag{5.7}$$

Here, r_m is the maximum breakthrough of the injectate plume, which is a function of z and t. Π is the similarity variable for Eq. (5.7) and it is not known here, but the exact expression of Π for gravity-free conditions is well-known as (69),(41).

$$\frac{r}{r_m} = \frac{1}{m-(m-1)S} \tag{5.8}$$

$$r_m = \sqrt{\frac{Q_o m t}{\pi \varphi}} \tag{5.9}$$

For the case of nonlinear relative permeability relationships, generalized forms Chapter 4

$$\frac{r}{r_m} = \sqrt{\frac{F'(S)}{F'(S_c)}} \tag{5.10}$$

$$r_m = \sqrt{\frac{F'(S_c) Q_o t}{\pi \varphi}} \tag{5.11}$$

In the case of injection of a less viscous fluid into a saturated water wet-formation, a combination of a continuous trail (rarefaction wave) that follows a faster shock wave is always generated, Fig (5.1). The size of this continuous transition zone grows over time, eventually resulting in a huge transition zone. The nature of the rarefaction wave behind the shock wave is important for many practical reasons because it specifies the distribution of saturation at different times.

Fig (5.3) shows the location of the shock wave for axisymmetric injection into a water-wet saturated tabular reservoir with a vertically penetrating well at the left, and r >> B so that flux is almost entirely horizontal. To the upper left of the shock front, the water saturation is 0.6, to the right of the shock front it is 1.0. The residual saturation is taken to be $S_r = 0.2$, and the

lower part of the figure shows the distribution of saturation along two different horizontal surface defined by the intersection of the radius of 250 and 1000 m respectively with the shock wave front. The transition zone is the curved line (rarefaction wave), the shock wave is the jump in saturation, and beyond that, the injectant has yet to penetrate.

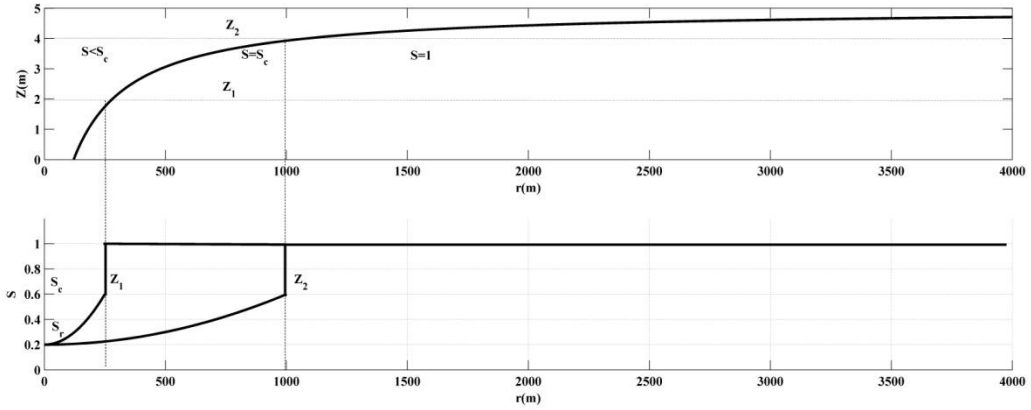

Fig 5-3 Schematic saturation distribution for nonlinear relative permeability function, position of isosat S=Sc is equivalent to the shockwave.

5.3 Analytical solution:

Starting from typical constitutive formulation primary drainage

$$\begin{cases} k_{rw} = S_e^{\,a} \\ k_{rg} = b\left(1 - S_e\right)^b \\ P_c = AS^{-1} = \dfrac{A}{1 - S_r}\left(S_e + \dfrac{S_r}{1 - S_r}\right)^{-c} \end{cases} \tag{5.12}$$

Assuming a=b=2 and c=1. These values are consistent to core data provided in (32). In this simple but important case, analytical solution for saturation distribution with inclusion of nonlinearity of relative permeability functions and Leverett-J function can be computed without numerical discretization, if the capillary-diffusive term is neglected.

$$P_c = J\left(S, S_r\right) \rightarrow J\left(S_e\right) = \frac{A}{1 - S_r}\left(S_e + \frac{S_r}{1 - S_r}\right)^{-1} \tag{5.13}$$

$$S = J^{inv}\left(S_e\right) \rightarrow S_e = \begin{cases} \dfrac{A}{P_c\left(1 - S_r\right)} - \dfrac{S_r}{1 - S_r} & P_c > A \\ 1 & P_c < A \end{cases} \tag{5.14}$$

By introducing S^{top}

$$S^{top} = S\big|_{z = H} \tag{5.15}$$

Its possible to rewrite the Eq (5.15)

$$P_c^{top} = \frac{A}{1 - S_r}\left(S_e^{top} + \frac{S_r}{1 - S_r}\right)^{-1} \tag{5.16}$$

And by assuming vertical hydrostatic pressure distribution

$$P_c = P_c^{top} - \Delta\gamma z = \frac{A}{1-S_r}\left(S_e^{top} + \frac{S_r}{1-S_r}\right)^{-1} - \Delta\gamma z \tag{5.17}$$

Its possible obtain the position of the interface, that represents the position of capillary pressure equivalent to P_c =A.

$$b = \frac{A}{(1-S_r)\Delta\gamma}\left[\left(S_e^{top} + \frac{S_r}{1-S_r}\right)^{-1} + S_r - 1\right] = \frac{A}{(1-S_r)\Delta\gamma}\left(Q(S_e^{top}) + S_r - 1\right) \tag{5.18}$$

By imposing the boundary conditions

$$b = \begin{cases} EQ\left(S_e^{top}\right) + D & \left(EQ\left(S_e^{top}\right) + D\right) < B \\ B & \left(EQ\left(S_e^{top}\right) + D\right) > B \end{cases} \tag{5.19}$$

$$E(S_r) = \frac{A}{(1-S_r)\Delta\gamma} \tag{5.20}$$

$$D = -\frac{A}{\Delta\gamma} \tag{5.21}$$

Saturation can be readily obtained from Eq (5.14)

$$S_e = \begin{cases} \dfrac{1}{\dfrac{1}{S_e^t + \dfrac{S_r}{1-S_r}} - \dfrac{\Delta\gamma(1-S_r)}{A}z} - \dfrac{S_r}{1-S_r} & z < b \\ 1 & z > b \end{cases} \tag{5.22}$$

For simplicity, we introduce two new terms here,

$$Q(S_e^t) = \frac{1}{S_e^t + \dfrac{S_r}{1 - S_r}}$$

$$W(S_r) = \frac{\Delta\gamma(1 - S_r)}{A} = \frac{1}{E(S_r)}$$

$$P(S_r) = \frac{S_r}{1 - S_r}$$

Consequently

$$S_e = \begin{cases} \dfrac{1}{Q(S_e^t) - W(S_r)z} - P(S_r) & z < b \\ 1 & z > b \end{cases} \tag{5.26}$$

Now it possible to calculate the mobilities and vertically averaged saturation

$$\tilde{S}_e = \frac{1}{B}\left[\frac{1}{W(S_r)}\ln\left(\frac{Q(S_e^t)}{Q(S_e^t) - W(S_r)b}\right) - P(S_r)b + (B - b)\right] \tag{5.27}$$

$$\tilde{S}_e = \frac{1}{B}\left[\frac{1}{W(S_r)}\ln\left(\frac{Q(S_e^t)}{Q(S_e^t) - W(S_r)b}\right) - \left(P(S_r) + 1\right)\left(E\,Q(S_e^t) + D\right) + B\right] \tag{5.28}$$

and by substitution of Eq (5.26) in Eq (5.12)

$$k_{rw} = S_e^2 = \begin{cases} \left(\dfrac{1}{Q(S_e^t) - W(S_r)z} - P(S_r)\right)^2 & z < b \\ 1 & z > b \end{cases} \tag{5.29}$$

$$\tilde{k}_{rw} = \frac{1}{B}\left[\begin{array}{l} \dfrac{1}{W(S_r)}\left(\dfrac{1}{Q(S_e^t) - W(S_r)b} - \dfrac{1}{Q(S_e^t)}\right) \\ + \dfrac{2P}{W(S_r)}\ln\left(\dfrac{Q(S_e^t) - W(S_r)b}{Q(S_e^t)}\right) + P(S_r)^2 b + (B - b) \end{array}\right] \tag{5.30}$$

$$k_{rn} = \beta\left(1 - S_e\right)^2 = \begin{cases} \beta\left(1 + P(S_r) - \dfrac{1}{Q\left(S_e^t\right) - W(S_r)z}\right)^2 & z < b \\ 0 & z > b \end{cases} \quad (5.31)$$

$$\tilde{k}_{rn} = \frac{\beta}{B}\left[\begin{array}{l} -\dfrac{1}{W(S_r)}\left[\dfrac{1}{Wb - Q(S_e^t)} + \dfrac{1}{Q(S_e^t)}\right] - \\ \dfrac{2(1+P(S_r))}{W(S_r)}\ln\left(\dfrac{Q(S_e^t)}{Q(S_e^t) - W(S_r)b}\right) + \left(1 + P(S_r)\right)^2 b \end{array}\right] \quad (5.32)$$

Expanded formulation for the capillary term is not derived here, as it will be proved that the capillary term is negligibly small. By averaging the flow equations

$$\begin{cases} \tilde{u}_w = -\tilde{\lambda}_w P,_r & (5.33) \\ \tilde{u}_n = -\tilde{\lambda}_n P,_r - \tilde{\lambda}_n \tilde{P}_c,_r & (5.34) \end{cases}$$

And by substitution of Eq (5.29) and Eq (5.30) in Eq (5.33) and Eq (5.34), the analytical integration is possible. To eliminate the pressure, fractional flow function can be introduced as

$$\tilde{F} = \frac{\tilde{\lambda}_w}{\tilde{\lambda}_w + \tilde{\lambda}_n} = \frac{\tilde{k}_{rw}}{\tilde{k}_{rw} + \dfrac{\mu_w}{\mu_n}\tilde{k}_{rn}} \quad (5.35)$$

Using the incompressibility of the two fluids, it is possible to write the equations as

$$\tilde{u}_w = \tilde{F}Q_o + \frac{1}{B}\int_0^B F\lambda_n P_c,_r \, dz \quad (5.36)$$

It is possible to rewrite the mass conservation equation as

$$\nabla.\tilde{u}_w = \varphi\left(1 - S_r\right)\frac{\partial \tilde{S}}{\partial t} \quad (5.37)$$

By substituting Eq (5.36) in Eq (5.37)

$$\overbrace{\Lambda(S^{top})S^{top}_{,r^2}}^{advective} + \overbrace{K(S^{top})}^{diffusive}{}_{,r^2} = H(S^{top})S^{top}_{,t} \tag{5.38}$$

and in Eq (5.38);

$$\Lambda(S^{top}) = \frac{\tilde{F}'Q_o}{\pi\varphi(1-S_r)} \quad (Q_o(\frac{m^2}{\sec}) total \quad rate \quad of \quad injection) \tag{5.39}$$

$$K(S^{top}) = \gamma_{s-c}\ \frac{\sqrt{\varphi k_{in}}}{\mu_n \varphi(1-S_r)} rv(S^{top})_{,r} \tag{5.40}$$

$$H(S^{top}) = \tilde{S} \tag{5.41}$$

v is vertical averaged of mobility of gas in fractional flow

$$v(S^{top}) = \frac{1}{B}\int_0^B \frac{\lambda_n(S^{top},z)}{k_{in}\varphi(1-S_r)} F(S^{top},z)\, j(S^{top},z)dz \tag{5.42}$$

In the basin scale, only for very small spatial scale of injection or very large Leverett-J functions the capillary pressure term will be comparable to the convective and accumulation terms, otherwise capillary term can be dropped and hyperbolic equation becomes a good approximation for the diffusive convective equation. This has been proved in many references (see (41), (77)).

Eq (5.38) is an advection diffusion equation, and it is solvable by any standard numerical method. It is possible to neglect the second term on the right hand side and use the hyperbolic asymptotic limit as an approximation. Eq (5.38) is reduced to a hyperbolic equation as

$$\frac{\tilde{F}'Q_o}{\pi\varphi(1-S_r)}\frac{\partial S_e^t}{\partial r^2} = H'\frac{\partial S_e^t}{\partial t} \tag{5.43}$$

$$S_e^t\Big|_{t=0} = \begin{cases} 1 & r>0 \\ 0 & r<0 \end{cases} \tag{5.44}$$

Eq (5.43) is a Cauchy-Riemann equation, and its analytical solution is possible (50) (67). Position of isosats (b) is calculated from Eq (5.18) and that incorporates capillary effect and nonlinearity of relative permeability functions.

This should be clarified here that the negligible capillary term in Eq (5.38) is not necessarily equivalent to small capillary forces. In the other words, small capillary force always diminishes the capillary term, but there is a possibility of negligibly small capillary term in Eq (5.38) when the capillary force is significant. That clarifies the existence of transition zone (capillary fringe) when the conservation equation is strictly hyperbolic.

$$\tilde{F}' = \frac{\tilde{k}'_{rw}\left(\tilde{k}_{rw} + M\tilde{k}_{rn}\right) - \tilde{k}_{rw}\left(\tilde{k}'_{rw} + M\tilde{k}'_{rn}\right)}{\left(\tilde{k}_{rw} + M\tilde{k}_{rn}\right)^2} \tag{5.45}$$

From Eq (5.45) and Eq (5.43),

$$\tilde{k}'_{rw} = \frac{1}{BW}\left(\frac{W\,b' - Q'}{(Q - Wb)^2} + \frac{Q'}{Q^2}\right) + \frac{2P}{BW}\left(\frac{(Q' - Wb')Q - (Q - Wb)Q'}{Q(Q - Wb)}\right) + \frac{P^2 b' - b'}{B} \tag{5.46}$$

$$\tilde{k}'_{rw} = \frac{Q'}{B}\left[\frac{1}{W}\left(\frac{We - 1}{(Q - Wb)^2} + \frac{1}{Q^2}\right) + \frac{2P}{W}\left(\frac{(1 - We)Q - (Q - Wb)}{Q(Q - Wb)}\right) + \left(P^2 e - e\right)\right] \tag{5.47}$$

$$\tilde{k}'_{rn} = \frac{\beta}{B}\left[\frac{1}{W}\left(\frac{Q'}{Q^2} - \frac{Q' - Wb'}{(Wb - Q)^2}\right) - \frac{2(1 + P)}{W}\left(\frac{Q'(Q - Wb) - Q(Q' - Wb')}{Q(Q - Wb)}\right) + (1 + P)^2 b'\right] \tag{5.48}$$

$$\tilde{k}'_{rn} = \frac{\beta Q'}{B}\left[\frac{1}{W}\left(\frac{1}{Q^2} - \frac{1 - We}{(Wb - Q)^2}\right) - \frac{2(1 + P)}{W}\left(\frac{(Q - Wb) - Q(1 - We)}{Q(Q - Wb)}\right) + (1 + P)^2 e\right] \tag{5.49}$$

$$H' = \frac{1}{B}\left[\frac{1}{W}\left(\frac{Q'(Q - Wb) - Q(Q' - Wb')}{Q(Q - Wb)}\right) - Pb' - b'\right] \tag{5.50}$$

$$H' = \frac{Q'}{B}\left[\frac{1}{W}\left(\frac{(Q - Wb) - Q(1 - We)}{Q(Q - Wb)}\right) - e(P + 1)\right] \tag{5.51}$$

And from Eq (5.23) and Eq (5.24)

$$Q' = -\frac{S^{t'}}{\left(S^{t} + P\right)^2} \tag{5.52}$$

$$b' = eQ' \tag{5.53}$$

$$e = \begin{cases} \dfrac{A}{(1 - S_r)\Delta\gamma} = E & \left(E\,Q\left(S_e^{top}\right) + D\right) < B \\ 0 & \left(E\,Q\left(S_e^{top}\right) + D\right) > B \end{cases} \tag{5.54}$$

By subsisting Eq (5.52) in Eq (5.43),

$$\Psi'\left(S^t\right) = \frac{F'(Q)}{H'(Q)} \rightarrow \Psi' \frac{\partial S^t}{\partial r^2} = \frac{\partial S^t}{\partial t} \tag{5.55}$$

Eq (5.55) is a classic Cauchy-Riemann equation, and depending on ψ' the nature of the solution is different. As it is apparent from Fig (5.4), ψ' is not increasing and therefore the results is a combination of shock and rarefaction wave. This is equivalent to Eq (4.16) (chapter 4).

$$\frac{\int_{S^*}^{1} \psi' ds}{1 - S^*} = \psi(S^*) \tag{5.56}$$

For B=30 (m), β=0.5, Δγ =3000 (N), A=5×10^5, S_r=0.3, φ=0.3 and M=19.3 result of the Eq (5.56) is S^*=0.58. Value of S^* is the saturation of shock wave, and it is not consistent to the numerical results. The mathematical derivations are straight forward, but all are based on the vertical equilibrium assumption. This method has been used by Nordbotten and Dahle (58) for injection time scale and by Golding et al. (60) for post injection process. But in the both of the aforementioned, the results were not compared to analytical solutions. The sources of

the error here come from capillary-gravity assumption, which is not physical for two phase zone.

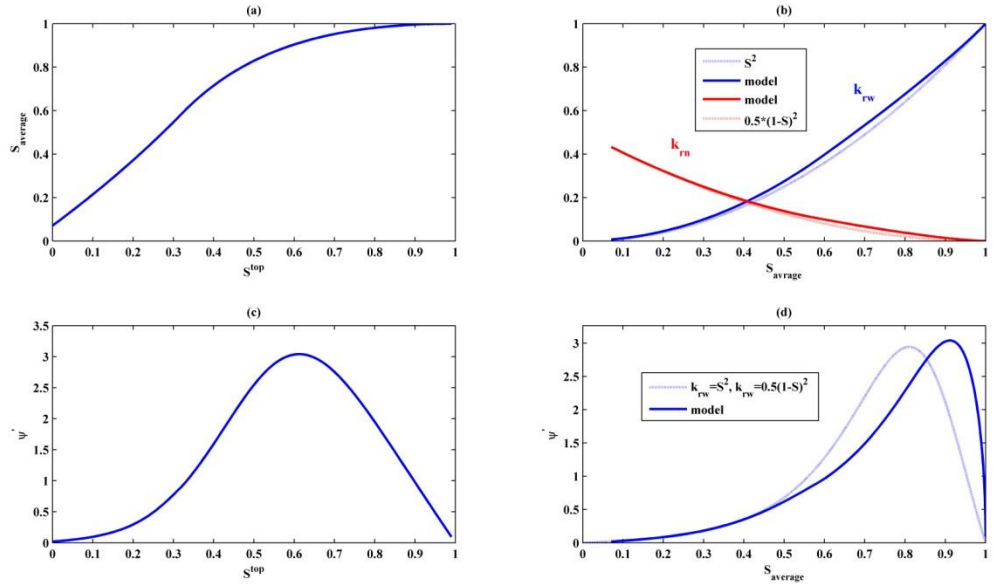

Fig 5-4 (a) calculated values of vertically averages saturation versus the saturation on the top of the aquifer (b) calculated vertically averaged relative permeability function from Eq (5.46) and Eq (5.47) (continuous line) and relative permeabilities from Eq (5.12) (discontinuous lines) (c) Hyperbolic function versus saturation in the top (d) Hyperbolic function versus vertically averaged saturation (continuous lines) and from relative permeabilities Eq (5.46) and Eq (5.47) (discontinuous lines).

Table 5-1 Parameters and characteristics of equivalent fractional function

a Eq (5.12)	b Eq (5.12)	c Eq (5.13)	Δγ (N)	M	A (Pa)
2	0.5	1	3000	19.3	5×10^5

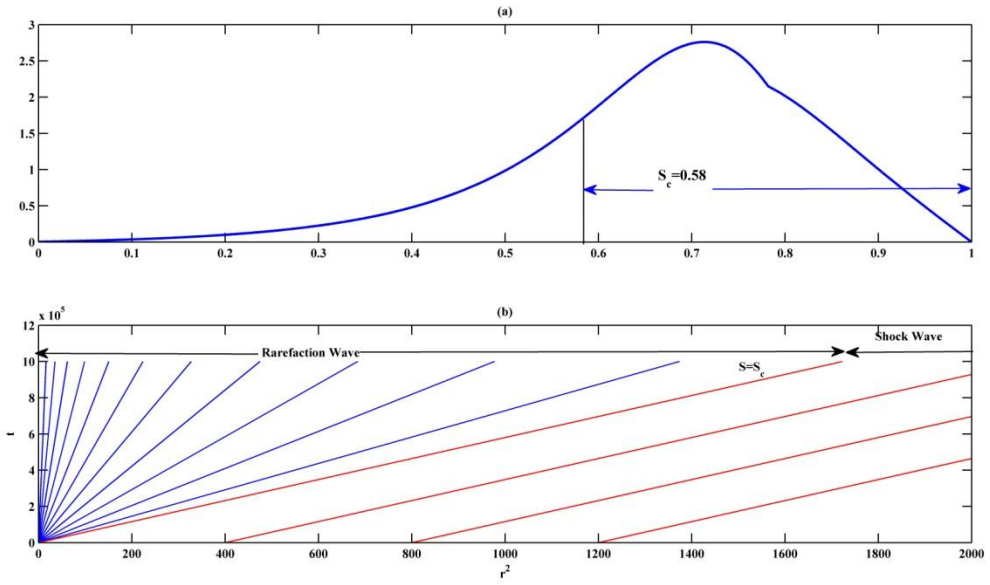

Fig 5-5 (a) Hyperbolic function and S*, saturation on the tip of shock wave (b) characteristics for shock and rarefaction.

Analytical solution of Eq (5.55) is straight forward. Because of the convexity of the hyperbolic function close to S=0, the transition stars with rarefaction wave, and before the inflection point, the solution transforms to a shock wave. Using Rankine-Hugoniot jump condition the velocity of shock wave should be equal to the velocity of rarefaction waves of the closest ray of saturation.

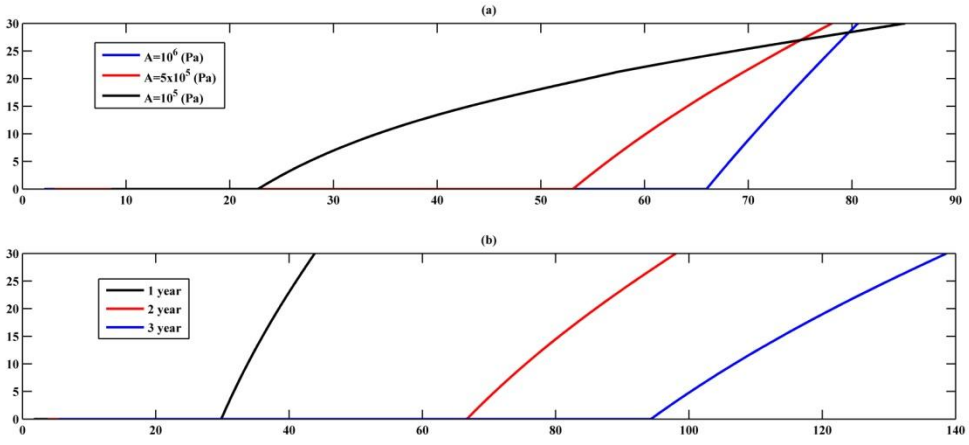

Fig 5-6 (a) position of the interface at t=108 (sec) for three different values of A (air entry pressure) (b) position of interface for A=5x105 (Pa) for three different times

Analytical solution of Eq (5.55) is straight forward, but requires an intensive integration to derive the functions F and H (see (58)). That should also be considered that the simplest possible relative permeability and Leverett-J functions are deployed here. If a more complex relative permeability function be deployed, analytical solution of Eq (5.55) becomes more complicated. Here a semi analytical solution is proposed to derive a reasonable approximation of the problem.

5.4 Semi analytical solution:

For an arbitrary relative permeability function, the critical saturation value Sc delineates the position and amplitude of the frontal shock. Behind the frontal shock, a continuous rarefaction wave exists and expands through time. In this part of the chapter, a vertically averaged flow rate is calculated above the shock front. By averaging the nonlinear functions through the vertical domain, an approximate formulation based on the averaged saturation is obtained. The advantage of the linear relative permeability functions is that by averaging the flow rate over the thickness of the aquifer, the flow rate can be written directly based on the vertically averaged saturation, allowing one to reduce the problem from a 2D to a 1D equation (which is a type of 1D Cauchy-Riemann equation), and then invoke classic solutions for this 1D hyperbolic equation. However, as shown by the mathematical modeling results in Fig 1, this oversimplifies the problem and leads to large deviations from a realistic solution in almost all cases. Similarly to Fig (5.7) below (dotted lines), two different linear approximations have been suggested for the set of linear relative permeabilities: one is a line that connects the beginning and end of the relative permeability function, and the other is the tangent line at $S = S_c$.

An averaging process can be used only if there is a continuous distribution of saturations behind the shock wave in the transition zone, and the relative permeability functions must also be continuously differentiable. The linearization of the relative permeability functions

introduced here only approximates the amplitude of the rarefaction wave (the continuous part of the saturation transition).

$$u_{uw} = -\lambda_w(S)P,r \tag{5.57}$$

$$u_{un} = -\lambda_n(S)P,r \tag{5.58}$$

Averaging the velocity over the continuous thickness [b,B] gives b the height of the shock wave and B the thickness of the reservoir.

$$\tilde{u}_{uw/n} = \int_b^B u_{uw/n}dz = -\left[\int_b^B \lambda_{w/n}(S)dz\right]P,r \tag{5.59}$$

Because in the zone of continuous saturation transition (above the shock front in Fig (5.5) the functions are differentiable, it is possible to expand the relative permeability function around the vertically averaged saturation. Using a Taylor series at S = Sc, a linear approximation can be made

$$\tilde{u}_{uw/n} = -\left[\int_b^B \left[\lambda_{w/n}(\tilde{S}) + \lambda'_{w/n}(\tilde{S})(S-\tilde{S}) + \lambda''_{w/n}(\tilde{S})\frac{(S-\tilde{S})^2}{2} + O\left((S-\tilde{S})^3\right)\right]dz\right]P,r \tag{5.60}$$

Keeping the first and the second terms of Eq. (5.60) provides a reasonable approximation for the relative permeability function, the second term of Eq. (5.60) vanishes and the averaged velocity is reduced to

$$\tilde{u}_{uw/n} = -\lambda_{w/n}(\tilde{S})P,r \tag{5.61}$$

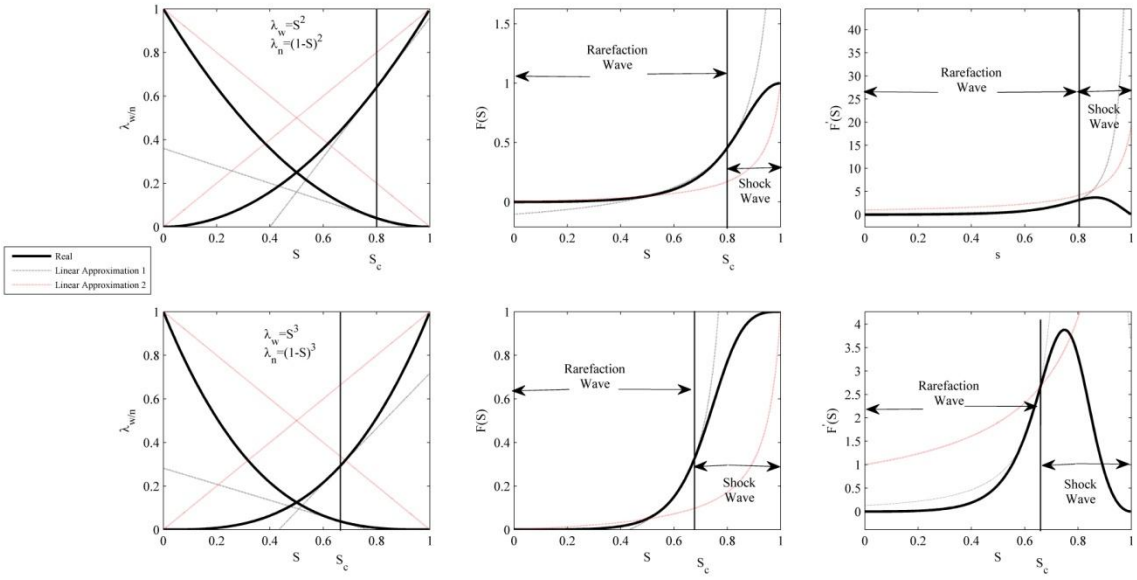

Fig 5-7 Linear approximation for relative permeability functions, fractional flow functions and derivations of fractional flow functions. Two different linear approximations are used, one is the tangent line that passes through $S_e=S_c$ and the second is the line that connects relative permeability for $S_e=0$ to $S_e=1$. Large differences are noted.

Fig (5.7) shows a reasonable linearized approximation for the set of relative permeability functions, and it is important to note that the linearized relative permeability functions are close enough to the real fractional flow function in the rarefaction part of the saturation curve to be realistic. As suggested before, a single line approximation for the entire range of saturation behind the shock wave usually leads to excessive error, which makes a general assumption of pseudo-linearity impractical, especially for the amplitude of the shock wave $S \epsilon [S_c, 1]$.

5.4.1 Generalized mass conservation:

In order to write the conservation equation and to include the continuous trail of saturation behind the shock wave, the height of the shock wave and the average saturation above the shock waves are considered as the unknowns here. Using linearized relative permeability functions, the velocity of the water in the transition zone above the shock wave is formulated as (Fig 5.7)

$$\tilde{u}_{uw}(r,t) \approx -\lambda_{wl}(\tilde{S}_{(r,t)})P,r \qquad S_r < S < S_c \tag{5.62}$$

$$\tilde{u}_{un}(r,t) \approx -\lambda_{nl}(\tilde{S}_{(r,t)})P,r \qquad S_r < S < S_c \tag{5.63}$$

And for the region below the shock wave

$$\tilde{u}_{dw}(r,t) = -\lambda_{wl}(1)P,r \qquad S_c < S < 1 \tag{5.64}$$

$$\tilde{u}_{dn}(r,t) = 0 \qquad S_c < S < 1 \tag{5.65}$$

If b is height of the shock wave, the total injected flow from the well at any radius is

$$q_n = (B-b)\tilde{u}_{un} \tag{5.66}$$

$$q_w = (B-b)\tilde{u}_{uw} + b\tilde{u}_{dw} \tag{5.67}$$

Eliminating pressure from the set of equations, and rewriting the mass conservation equation

$$q_t = q_w + q_n = \frac{Q_o}{2\pi r} \tag{5.68}$$

By some mathematical manipulation, it can be shown that

$$q_n = \frac{(B-b)\lambda_{nl}(\tilde{S}_{(r,t)})Q_o}{2\pi r\left[(B-b)\underbrace{\left(\lambda_{nl}(\tilde{S}_{(r,t)}) + \lambda_{wl}(\tilde{S}_{(r,t)})\right)}_{\lambda_{tl}(\tilde{S})} + \lambda_{wl}(1)b\right]} \tag{5.69}$$

Introducing

$$\lambda_{tl}(\tilde{S}) = \lambda_{nl}(\tilde{S}) + \lambda_{wl}(\tilde{S}) \tag{5.70}$$

$$q_n = \frac{(B-b)\lambda_{nl}(\tilde{S})Q_o}{2\pi r\left((B-b)\lambda_{tl}(\tilde{S}) + \lambda_{wl}(1)b\right)} \tag{5.71}$$

And finally

$$\nabla \cdot q_n = \frac{\partial\left(\varphi(B-b)(1-\tilde{S})\right)}{\partial t} \tag{5.72}$$

$$\frac{\partial}{\partial r^2}\left[\frac{(B-b_{\left(r^2,t\right)})\lambda_{nl}(\tilde{S}_{\left(r^2,t\right)})Q_o}{\pi\left((B-b_{\left(r^2,t\right)})\lambda_{tl}(\tilde{S}_{\left(r^2,t\right)}) + \lambda_{wl}(1)b_{\left(r^2,t\right)}\right)}\right] = \frac{\partial\left(\varphi(B-b_{\left(r^2,t\right)})(1-\tilde{S}_{\left(r^2,t\right)})\right)}{\partial t} \tag{5.73}$$

Eq. (5.73) is a hyperbolic equation, but there are two unknowns, b and $\tilde{S}$. The explicit relationship between these two is not known, but based on global mass conservation in steady-state injection rate conditions (constant Q_o), one may write

$$Q_o t = \int_0^{\sqrt{r_m}} \varphi\pi\left(1-\tilde{S}\right)(B-b)dr^2 \tag{5.74}$$

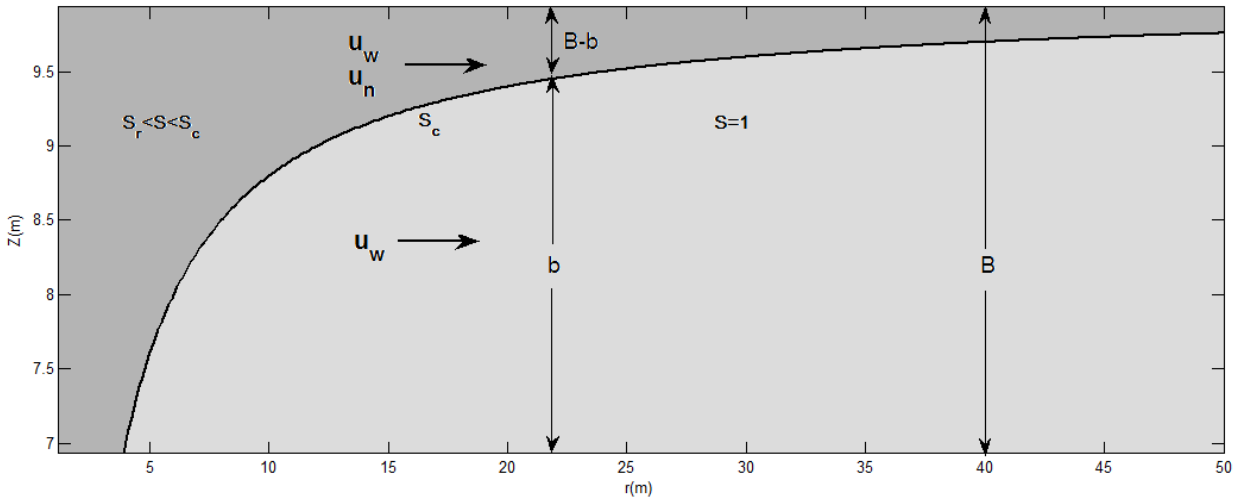

Fig 5-8 Schematic saturation distribution for horizontal velocity bellow and above of the shockwave

Lemma II: There is a monotonic one-to-one relationship between $\tilde{S}$ and b.

Proof: Based on dimensional analysis, it is possible to write the following relationship:

$$\frac{r}{r_m(z,t)} = P(S) \tag{5.75}$$

Here, P(S) is an unknown function that is different for different geometries and

characteristics and r_m is the maximum radius of breakthrough of the overriding immiscible phase. It is clear that P(S) is a monotonically increasing function, and also

$$\frac{\partial r_m}{\partial z} > 0 \tag{5.76}$$

By taking the derivation with respect to z from Eq. (5.76), it is possible to prove that

$$-\frac{r r_{m,z}}{P'(S) r_m^2} = S_{,z} \tag{5.77}$$

And consequently

$$S_{,z} < 0 \tag{5.78}$$

Based on Eq. (5.78), it is proven that saturation decreases monotonically with z. Now, by defining the vertically averaged value for S in any arbitrary radius as

$$\tilde{S}(r) = \frac{\int_b^B S(r,z)dz}{B-b} \tag{5.79}$$

$$S(r,b) = S_c \tag{5.80}$$

$$S(r,B) = P^{-1}\left(\frac{r}{r_m(B,t)}\right) \tag{5.81}$$

And by mapping S(r,z) from $z \in [b, B]$ to $z_{eq} \in [0,1]$, Eq. (5.79) can be simplified to

$$\tilde{S}(r) = \int_0^1 S(r,z)dz \tag{5.82}$$

$$S(r,0) = S_c \tag{5.83}$$

$$S(r,1) = P^{-1}\left(\frac{r}{r_m(B,t)}\right) \tag{5.84}$$

Consequently, for $r_1 < r_2$

$$\tilde{S}(r_1) - \tilde{S}(r_2) = \int_0^1 [S(r_1, z) - S(r_1, z)]dz = \int_0^1 \varphi(z)dz \tag{5.85}$$

In Eq (5.85), $\varphi(0) = 0$ and $\varphi(1) < 0$ and $\varphi,z < 0$, consequently

$$\tilde{S}(r_1) > \tilde{S}(r_2) \tag{5.86}$$

Eq. (5.86) is the mathematical proof that $\tilde{S}$ has a monotonically increasing relationship with r, and b has a monotonically increasing relationship with r, therefore $\tilde{S}$ and b are related in a monotonically increasing manner.

$$b = b\left(\tilde{S}_{(r,t)}\right) \tag{5.87}$$

Two points are known along the monotonically increasing correlation between b and $\tilde{S}$:

$$b(S_c) = B \tag{5.88}$$
$$b(S_{rw}) = 0 \tag{5.89}$$

5.4.2 Mathematical Solution:

An exact analytical solution for Eqs. (5.73) and (5.74) is not possible because the relationship between b and $\tilde{S}$ is not explicit. But, by using known information about the $b(\tilde{S})$ relationship developed above, an assumed correlation may be chosen and parameters can be modified iteratively. First, a exponential approximation for the correlation between b and $\tilde{S}$ is assumed, the two points on $b(\tilde{S})$ are known from Eqs. (5.88) and (5.89), and the value of m is unknown

$$S^{top} = S_c\left(\frac{e^{m\tilde{S}}-1}{e^{mS_c}-1}\right) \tag{5.90}$$

$$S^{top} \in [0, S_c] \quad \tilde{S} \in [0, S_c]$$

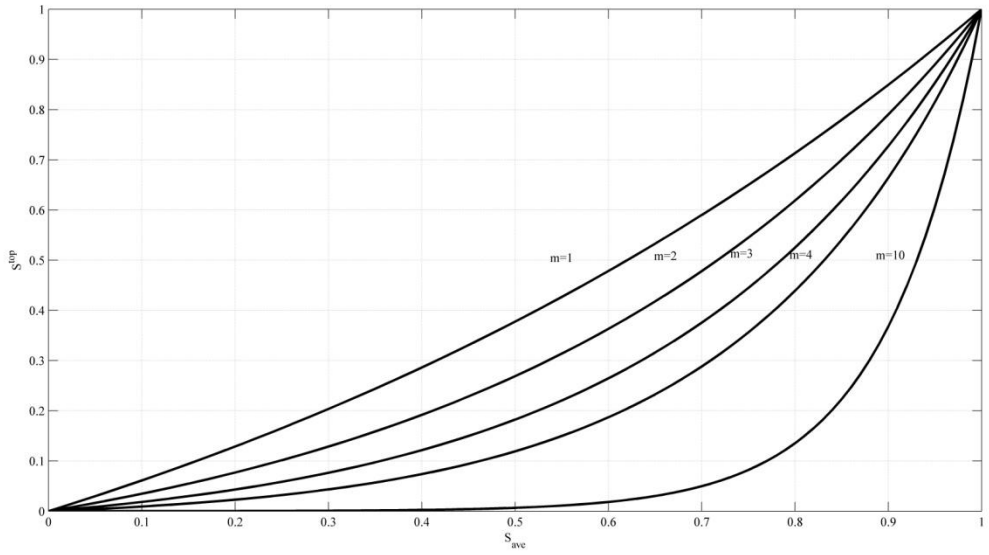

Fig 5-9 fitting functions for correlation between average saturation and the saturation on the top of the aquifer. Different values of m provide a wide range of curvatures to approximate the correlation between Stop and Save.

$$P_c^{top} = P_c\left(\frac{e^{m\tilde{S}}-1}{e^{m}-1}\right) = \frac{A}{1-S_r}\left(\frac{e^{m\tilde{S}}-1}{e^{m}-1}+\frac{S_r}{1-S_r}\right)^{-1} \tag{5.91}$$

$$P_c = P_c^{top} - \Delta\gamma(B-z) = \frac{A}{1-S_r}\left(\frac{e^{m\tilde{S}}-1}{e^{m}-1}+\frac{S_r}{1-S_r}\right)^{-1} - \Delta\gamma(B-z) \tag{5.92}$$

$$b = B + \frac{A}{\Delta\gamma(1-S_{rw})}\left[\left(S_c+\frac{1}{1-S_r}\right)^{-1} - \left(\frac{e^{m\tilde{S}}-1}{e^{m}-1}+\frac{S_r}{1-S_r}\right)^{-1}\right] \tag{5.93}$$

Eq (5.93) provides a relationship between $\tilde{S}$ and b with one degree of freedom. Eqs. (5.73) and Eq. (5.74) are sufficient for derivation of $\tilde{S}$ and consequently b, and the value of can be corrected iteratively. As a first estimation, an arbitrary value within the $[S_r, S_c]$ interval is

taken, and $\tilde{S}$ is calculated for any value of r. By substituting the derived values for $\tilde{S}$ into Eq. (5.74), a second better estimation for m is obtained, and the process continued until the chosen convergence criterion is met. Fig (5.10) is a flow chart showing the solution method.

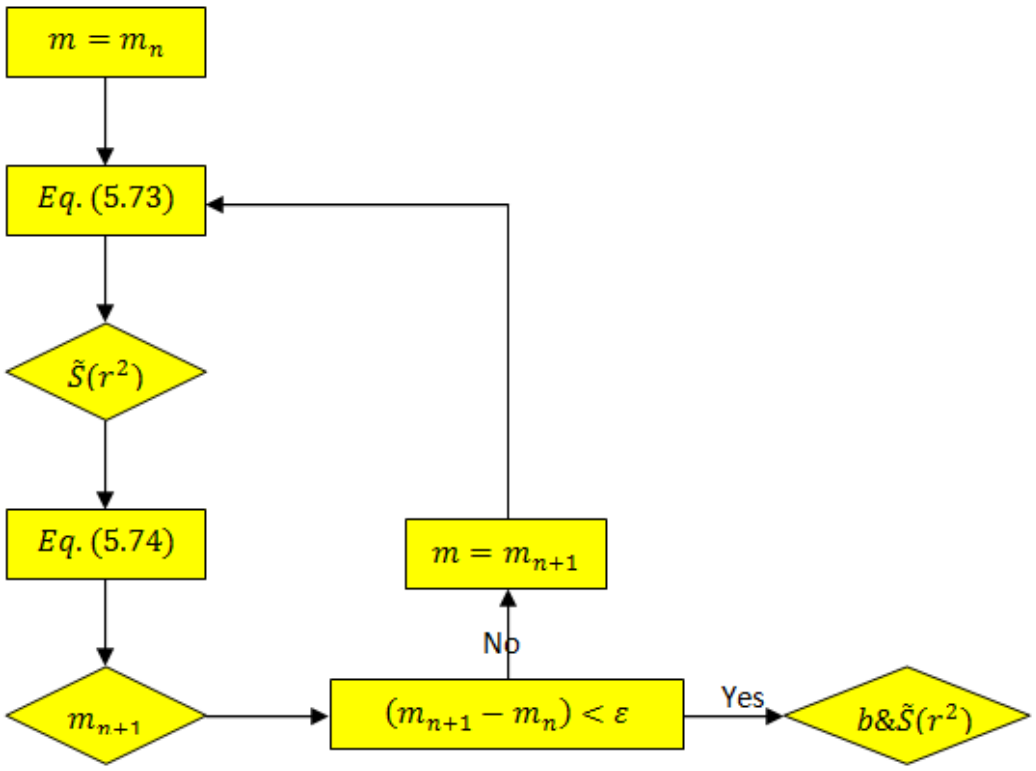

Fig 5-10-Semi-analytical procedure for solution of Eq (5.73) and Eq (5.74). Value of ε represents a limit for convergence of the scheme.

Figures (5.11) to (5.13) show the progress of the shock and rarefaction waves for a 30 m high reservoir using non-linear permeability functions. The smooth light lines are the results from this new development, and the darker lines represent results from the finite element model developed for this case. A reasonable agreement is seen, and the semi-analytic solution is preferred because, for the conditions and limitations described herein, it is considered to be fairly precise.

Table 5-2 Characteristics of primary injection of less viscous, less dense injectant into a water-wet saturated zone

Qo $(\frac{m^3}{sec})$	φ	Sr	m	a	Pc (air entry Pressure) (Pa)
0.0027	0.3	0.3	19.3	2	5×10^5

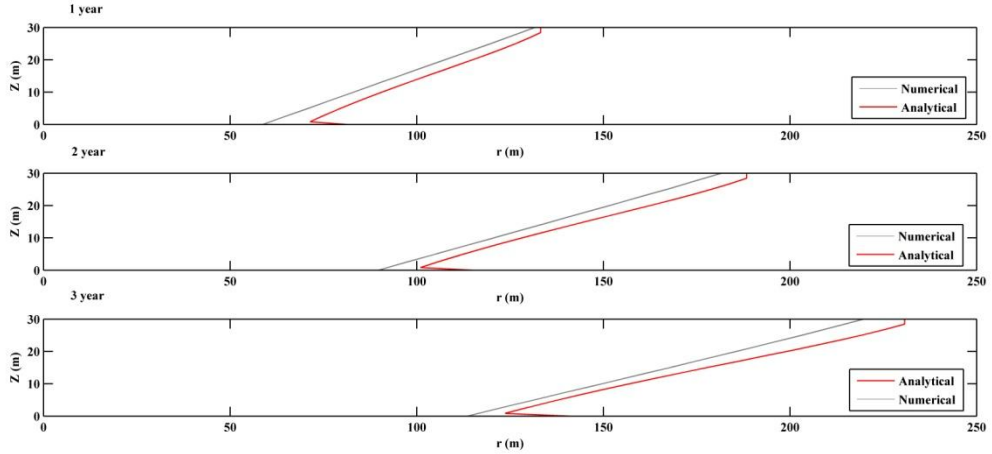

Fig 5-11 comparison between analytical and numerical solution for the position of interface for nonlinear case

Table 5-3 Characteristics of primary injection of less viscous, less dense injectant into a water-wet saturated zone

Qo $(\frac{m^3}{sec})$	φ	Sr	m	a	Pc (air entry Pressure) Pa
0.0027	0.3	0.3	19.3	1.5	5×10^5

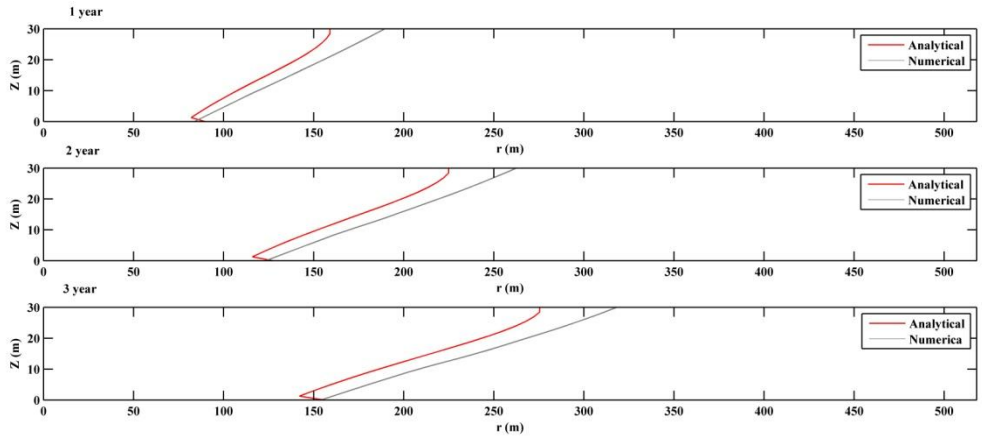

Fig 5-12 comparison between analytical and numerical solution for the position of interface for nonlinear case

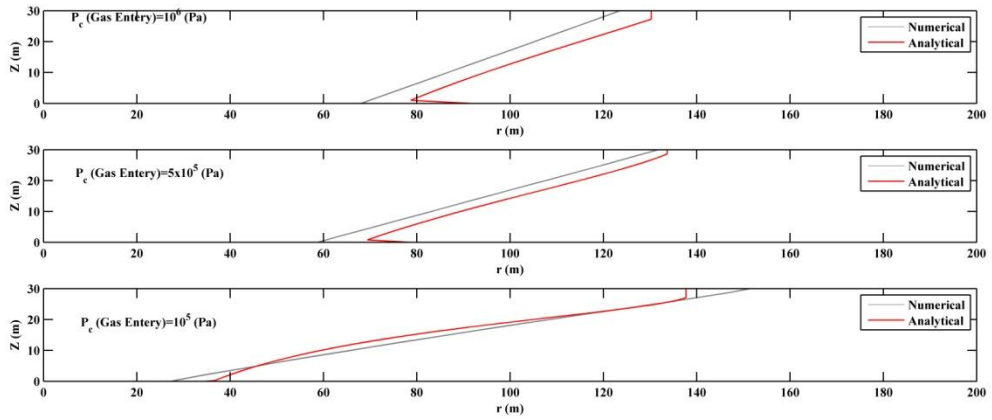

Fig 5-13 comparison between analytical and numerical solution for the position of interface for nonlinear case

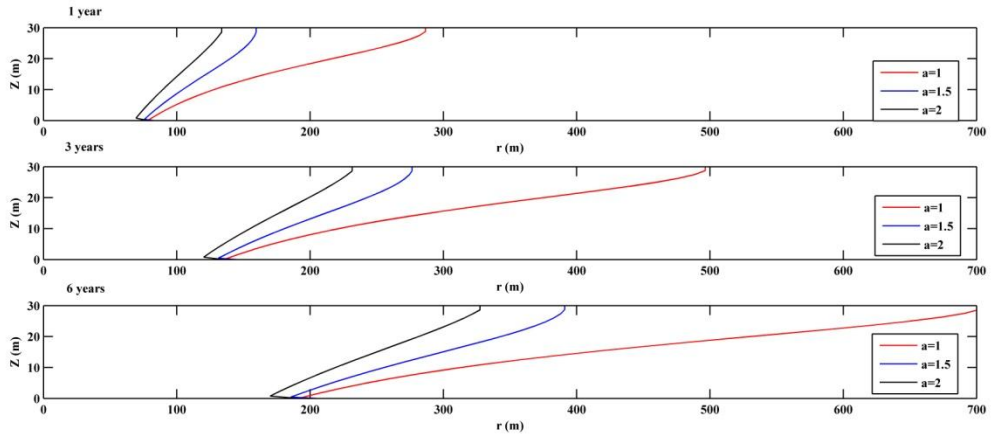

Fig 5-14 Effect of nonlinearity of saturation progression is presented as the position of shock wave for different values of a.

Table 5-4 Characteristics and parameters of injection problem

Qo $(\frac{m^3}{sec})$	φ	Sr	m	a	t (year)
0.001	0.3	0.3	19.3	1.5	1

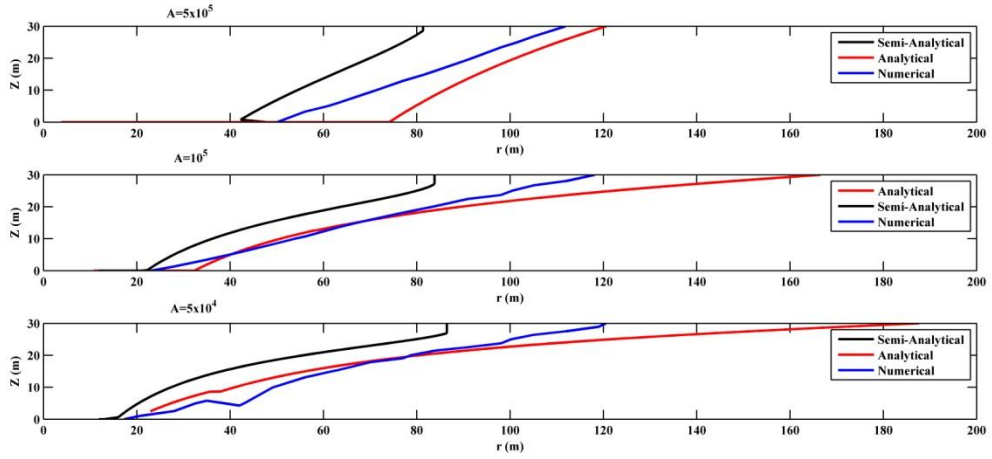

Fig 5--515-Comparison of analytical, numerical and semi analytical solution for the interface position for different values of gas entry pressure. The agreement is reasonable, and the semi analytical solution is easily adoptable for any degree of nonlinearity

5.5 Up scaled averaged mass conservation:

The theory is a combination of the analytical solution proposed by Juanes et al. (64) (81) and the one was proposed by Nordbotten and Dahle (58) or the analytical solution in section (5.3) that incorporates the effect of large scale capillary driven transition zone. Starting from Eq (5.33) and Eq (5.34)

$$\begin{cases} \tilde{u}_w = -\tilde{\lambda}_w P,_r & (5.94) \\ \tilde{u}_n = -\tilde{\lambda}_n P,_r - \tilde{\lambda}_n \tilde{P}_c,_r & (5.95) \end{cases}$$

And by introducing fractional flow function

$$\tilde{F} = \frac{\tilde{\lambda}_w}{\tilde{\lambda}_w + \tilde{\lambda}_n} = \frac{\tilde{k}_{rw}}{\tilde{k}_{rw} + \frac{\mu_w}{\mu_n}\tilde{k}_{rn}} \tag{5.96}$$

And by writing the mass conservation for wetting phase and neglecting the capillary term

$$\frac{F'\left(S^t\right)Q_o}{\varphi(1-S_r)}\frac{\partial S^t}{\partial r^2} = \frac{\partial \tilde{S}\left(S^t\right)}{\partial t} \tag{5.97}$$

And by writing

$$S^t = f\left(\tilde{S}\right) \rightarrow \frac{\partial S^t}{\partial r^2} = f'\left(\tilde{S}\right)\frac{\partial \tilde{S}}{\partial r^2} \tag{5.98}$$

f is the inverse of Eq (5.28), and analytical presentation of $f^{'}$ is complicated. But numerical calculation of $f^{'}$ is trivial. By substituting Eq (5.98) in Eq (5.97)

$$\frac{F'\left(f\left(\tilde{S}\right)\right)Q_o}{\varphi(1-S_r)}\, f'\left(\tilde{S}\right)\frac{\partial \tilde{S}}{\partial r^2} = \frac{\partial \tilde{S}}{\partial t} \;\rightarrow\; \Pi\left(\tilde{S}\right)\frac{\partial \tilde{S}}{\partial r^2} = \frac{\partial \tilde{S}}{\partial t} \tag{5.99}$$

Eq (5.99) is Π is the fractional flow function based on the vertically averaged saturation.

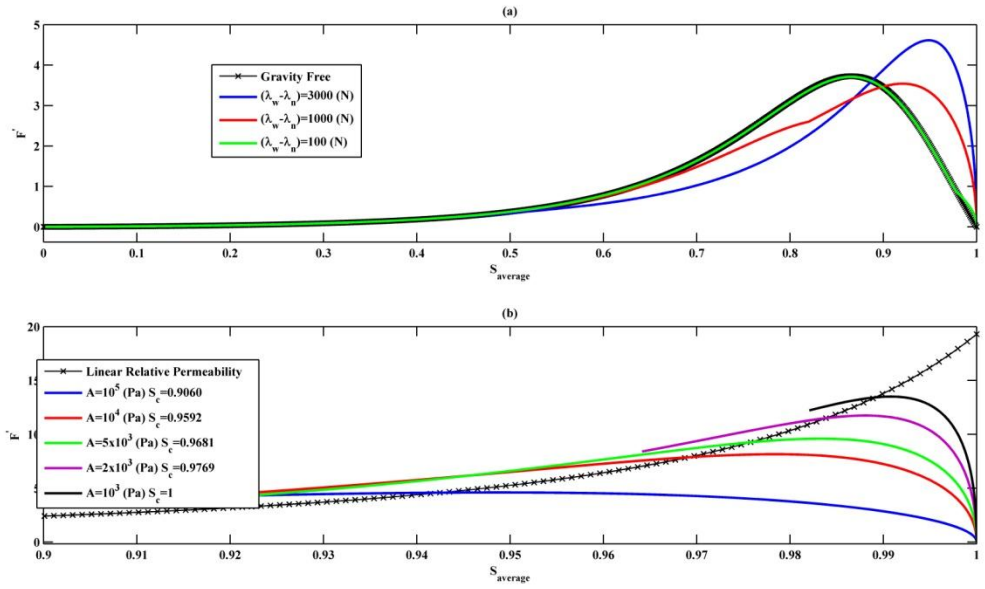

Fig 5-16 (a) Derivative of fractional flow function versus vertically averaged saturation for different Δγ, for Δγ=100 (N) the F' becomes similar to gravity-free case (b) Comparison of fractional flow function for a set of linear relative permeability function and the calculated fractional flow function for different values of A. Small values of A converge to linear relative permeability case, because small capillary force results in sharp interface between saline and CO_2.

Eq (5.99) is the up scaled fractional flow function for geometries with large aspect ratio. By using 1D problem instead of 2D, the calculation of saturation distribution is easier.

Eq (5.99) is valuable because it reduces the dimension of the problem and is the correct vertically averaged conservation of mass that is not based on the sharp interface assumption similar to the previous works (63), (76), (81), (39). Eq (5.96) is for the second degree of nonlinearity and with the same procedure it is possible to calculate equivalent 1D fractional flow function for other degrees of freedom.

5.6 Cyclic Injection:

In the most of the practical applications, cyclic injection of water and gas (Water Alteration Gas) is important. For special cases of CO2 sequestration, sequential injection of water and gas enhances surface contact between injectant (CO2) and host liquid (saline) and that provides faster dissolution of gas. In this section, analytical solution for the set of nonlinear relative permeabilities is extended to include the sequential injection of CO2-Sline.

Numerical simulation of cyclic injection is expensive and requires heavy computation and mesh adaptation, and any analytical approximation has a great value.

Gaseous injectant from the injector drains the porous media and invades the pores. By injecting saline after injection of gas, the invaded pores imbibe and the injected saline recaptures the invaded pores. In the case of significant capillary effect, the transition zone grows, and cyclic injection of water accelerates the mixing process. In previous section, gravity-primary drainage was reduces to a classic Buckley-Leverett equation, and in this chapter the solution is extended to cyclic reinjection of saline. Additional to enhancement of solubility trapping, after reinjection of saline, a trail of gas remain in its residual saturation. This has been extensively studied by Juanes et al. (81), Hesse et al. (54) and other researchers in the field.

$$S = \frac{S - S_r - S_{rg}}{1 - S_r - S_{rg}} \tag{5.100}$$

And Eq (5.99) can be rewrite as

$$\Pi\left(\tilde{S}\right)\frac{\partial \tilde{S}}{\partial r^2} = \frac{\partial \tilde{S}}{\partial t} \tag{5.101}$$

$$\Pi\left(\tilde{S}\right) = \frac{F'\left(f\left(\tilde{S}\right)\right)Q_m}{\varphi R}\, f'\left(\tilde{S}\right) \rightarrow \begin{cases} R = 1 - S_r & Q_m = Q_c & Drainage \\ R = 1 - S_r - S_{rg} & Q_m = Q_w & \text{Im}bibibition \end{cases} \tag{5.102}$$

Saturation distribution at the end of drainage process is initial condition of imbibition process. Front tracking methods should be used for solution of the secondary imbibition, and the interaction of imbibition wave to the drainage wave. Similar problem was solved by Juanes et al.(81) for strictly convex fractional flow function assuming a sharp interface and segregated phases. According to Fig (5.16-b), strictly convex fractional flow function is an asymptotic limit for small capillary forces. In case of significant capillary forces and diffused

interface, the fractional flow function cannot be strictly convex and has an inflection point. That condition provides a rarefaction wave chasing a faster shock wave. Because of the constant boundary condition at the far end (S=1), domain of the shock wave remain constant. In Fig (5.16-a) the saturation of the shock wave is equal to S_c.

Assuming the injection of CO_2 is stopped suddenly and water is injected from the same injector. It is easily practical, by switching the injectant from a single well. Fractional flow function remains similar, but the position of saturation transition will be reverse. Contrasting to (81), partial concavity of the fractional flow provides different possibilities for the wave's structure. In the other words, the imbibition front is not necessarily a single shock wave and there could be rarefaction trail follow the imbibition front. Domain of the shock wave saturation is obtained in Fig (5.16-a), and it is equal to S_w.

Mechanism of secondary imbibition is dominantly a shock wave, and that makes the imbibition front faster. Consequently the water front recaptures the drained zone much faster. Theoretically there are two possibilities for saturation transition during distribution process, but it will be proved that only one is relevant for physical parameters of aquifer and rate of injection. It is possible to define different stages for cyclic injection.

Primary Drainage: This process is similar to the problem that was discussed in the previous chapters and first part of this chapter. If the equivalent fractional flow function be applied for the gravity-drainage process, there will be rarefaction zone that follows a faster shock front. The completely drained zone is equivalent to the slowest ray of the rarefaction wave.

Chasing Process: The process starts after injection of water, and the structure of the saturation transition wave is a large shock wave that may be followed by a rarefaction wave.

The process is faster than the drainage process, and when the shock front reaches to the slowest rarefaction ray and the imbibition front starts to recaptures the transition zone, the process completes.

Interaction Process: The imbibition wave interacts with drainage wave. A simplified problem is solved in (57), when the imbibition is a single shock and drainage is a rarefaction wave. Here, a generalized solution is proposed that incorporates arbitrary structure of transition waves. A detailed approach is also suggested for *p-system* (dynamics of an inviscid , non heat conducting gas) is proposed in (50) that is readily adoptable to the multiphase system. Because of the larger velocity of the imbibition front the injected wetting phase recapture the drained zone. When the drained zone is totally recaptured, this stage is terminated.

Secondary Drainage: After completion of the previous stage and when the total drained area is recaptured by saline, the media becomes similar to intact water saturated zone. Drainage process can be repeated arbitrarily. Mathematically this process is similar to the primary drainage process, but the relative permeabilities and Leverett-J function can be different and hysteresis effect should be considered.

5.6.1 Formulations:

Starting from Eq (5.102), the drainages front velocities is calculated as

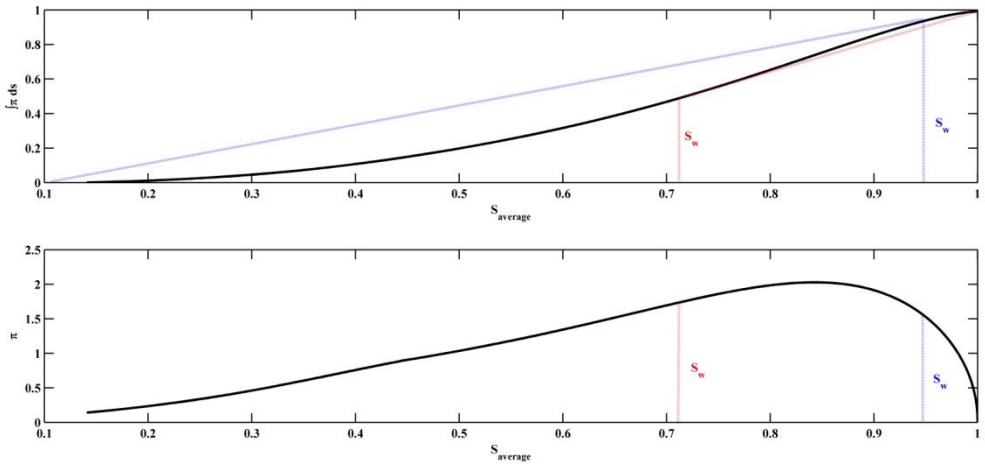

Fig 5-17 Equivalent fractional flow function and derivative of fractional flow function from Eq (5.45)

$$\frac{F'\left(f\left(\tilde{S}\right)\right)Q_o}{\varphi\left(1-S_r\right)} f'\left(\tilde{S}\right)\frac{\partial\tilde{S}}{\partial r^2}=\frac{\partial\tilde{S}}{\partial t} \rightarrow \Pi\left(\tilde{S}\right)\frac{\partial\tilde{S}}{\partial r^2}=\frac{\partial\tilde{S}}{\partial t} \tag{5.103}$$

Solution of Eq (5.103) is straight forward;

$$\Pi\left(\tilde{S}\right)=\frac{r^2}{t} \qquad S\in[0,S_c] \tag{5.104}$$

$$\Pi\left(\tilde{S}_c\right)=\frac{r^2}{t} \qquad S\in[S_c,1] \tag{5.105}$$

And the length of the completely drained zone (S=0) from Eq (5.104)

$$L=\sqrt{\Pi(0)t} \tag{5.106}$$

After injection of saline, the leading front is a shock and the domain of the shock is $[0,S_w]$.

From Rankine-Hugoniot condition, velocity of wave is obtained.

$$\sigma_w=\frac{\pi Q_w}{\varphi\left(1-S_{rw}-S_{rg}\right)}\frac{\int_{S_w}^{0}\Pi ds}{S_w} \tag{5.107}$$

And by defining t_c as the time that leading shock reaches to the L length of the drained zone) and impinges the transition zone.

$$t_c = \frac{L}{\sigma} \tag{5.108}$$

After the imbibition front reaches to the transition zone, the imbibition front interacts with the drainage wave (Interaction stage). Fractional flow function is not strictly convex, and there is possibility for evolution of a rarefaction wave. To find the saturation distribution in the interaction stage, we assume the existence of a rarefaction wave before the shock front and another rarefaction wave after the shock wave. Labeling the saturations on the upstream and downstream (i.e. left side and right side) of the shock front as S_u and S_d, and duration of gaseous injection and water injection as T and t. In discontinuous front the governing equations are continuity of the upstream and the downstream;

$$dx\big|_{Shock} = dx\big|_{Rarefaction\ of\ upstream} = dx\big|_{Rarefaction\ of\ downstream} \tag{5.109}$$

$$x\big|_{Rarefaction\ of\ upstream} = x\big|_{Rarefaction\ of\ downstream} \tag{5.110}$$

$$\sigma_w dt = d\left(\Pi(S_d)(t+T)\right) \tag{5.111}$$

Eq (5.110) and Eq (5.111) provide two independent equations for calculation of S_u and S_d at different times.

$$\sigma_w dt = d\left(\Pi(S_d)t\right) = \Pi'(S_d)(t+T)dS_d + \Pi(S_d)dt \tag{5.112}$$

$$\sigma_w = \frac{\pi Q_w}{\varphi\left(1-S_{rw}-S_{rg}\right)} \frac{\int_{S_d}^{S_u} \Pi ds}{S_d - S_u} dt = \Pi'(S_d)tdS_d + \Pi(S_d)dt \tag{5.113}$$

And by separation of variables

$$\frac{\Pi'(S_d)dS_d}{\left(\frac{\pi Q_w}{\varphi\left(1-S_{rw}-S_{rg}\right)}\frac{\int_{S_d}^{S_u}\Pi ds}{S_d-S_u}-\Pi(S_d)\right)}=\frac{dt}{t} \tag{5.114}$$

$$\int_0^{S_d}\frac{\Pi'(s_u)ds_u}{\frac{\pi Q_w}{\varphi\left(1-S_{rw}-S_{rg}\right)}\left(\frac{\int_{s_d}^{s_u}\Pi ds}{s_d-s_u}-\Pi(s_d)\right)}=\ln\left(\frac{T+t}{T+t_c}\right) \tag{5.115}$$

Numerical integration of Eq (5.116) is possible. Initial condition of Eq (5.116) comes from $t=t_c$, when the $S_u=S_w$ and $S_d=0$. The closing equation Eq (5.110) is

$$\Pi(S_u)t=\Pi(S_d)(T+t) \tag{5.116}$$

$$\Pi(S_u)=\Pi(S_d)\frac{(T+t)}{t} \tag{5.117}$$

An iterative numerical scheme readily can be used for calculation of S_u and S_d. Not surprisingly, the continuity equations are not satisfied for any values of S_u and consequently the rarefaction does not exist. It simplifies the problem drastically, and a correlation between S_d (downstream saturation) and t (saline injection) can easily obtain with a fixed upper limit of integration.

$$\int_0^{S_d} \frac{\Pi'(s)ds}{\frac{\pi Q_w}{\varphi\left(1-S_{rw}-S_{rg}\right)}\left(\frac{\int_s^1 \Pi ds}{1-s}-\Pi(s)\right)} = \ln\left(\frac{t+T}{t_c+T}\right) \tag{5.118}$$

This is equivalent to solution in (64).

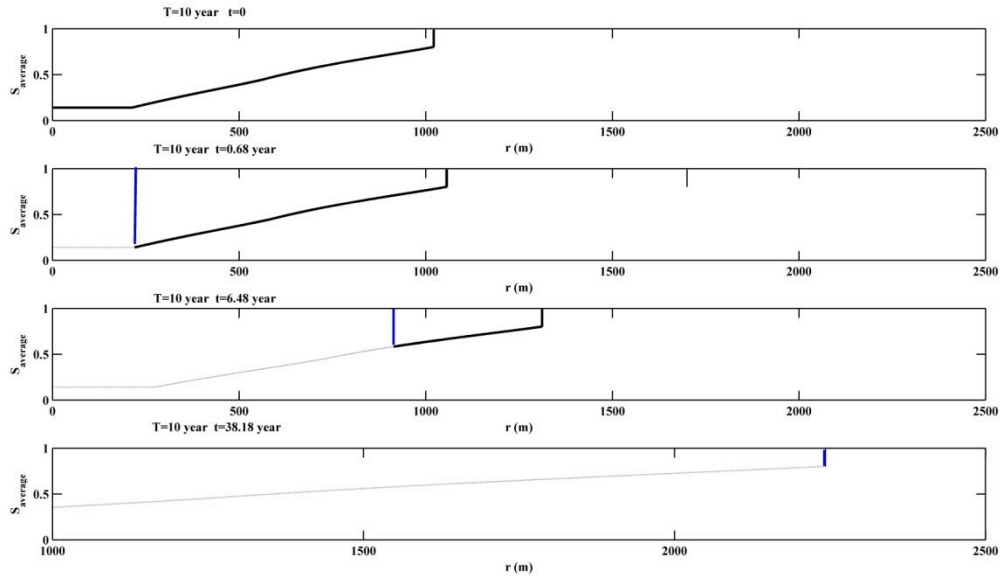

Fig 5-18 Snapshots of primary drainage and secondary imbibition, the black line represents gaseous interface and the blue line is saline front

5.7 Conclusions:

A semi-analytic solution has been developed for the location of the shock wave and saturation contours for non-linear permeability functions during injection of an immiscible fluid of different viscosity and density into a liquid-saturated tabular reservoir. The reservoir is isotropic and homogeneous, laterally extensive, and the grains are wet with the initial saturatant.

To achieve a solution, the following assumptions were made: incompressible fluids, constant density and viscosity, fluid immiscibility and non-reactivity.

Non-linearity was introduced by first proving that the relationship between the height of the shock wave and the mean saturation is a smooth, monotonic function, and by knowing the two end points of this relationship. Then, a predictor-corrector scheme is used to converge to an appropriate relationship which gives the location of the shock wave for the non-linear relative permeability case. The solution is limited to relative permeability curves (and transition zone saturations) that are continuous and monotonic, with a degree of nonlinearity less than exponent 3, and it is intended for use in primary drainage cases, such as the continuous injection of supercritical CO_2 into a saline aquifer for sequestration, water-flooding an oil-wet reservoir, gas injection into an oil-saturated reservoir, and related problems.

The incorporation of nonlinearity that has been achieved in these solutions, combined with the appreciation that the other assumptions are physically realistic for wide ranges of conditions, increases the practical importance of the developed solutions, and makes them applicable to real formations under real conditions. Hence, the solutions can be developed into useful engineering tools to be used at all times during sequestration activities, as well as being applied to other reservoir drainage and displacement processes involving immiscible fluids of different density. These analytical solutions are adaptable to a wide range of real geometries and characteristics, and provide a good approximation of saturation distribution at different times. Moreover, the cyclic injection of CO_2-water is a complicated process and the developed analytical solution can more easily capture the physics of the problem and propose an excellent approximation. Because the solution gives the result directly for any time, laborious time-stepping and numerical dispersion can be avoided in getting a "quick look" assessment before introducing a more complicated approach based on mathematical modeling. Clearly, issues such as heterogeneity and spatially varying properties must be

handled by mathematical modeling, but this modeling can be combined with the solutions herein to give better understanding of the engineering constraints.

6 Conclusion

The main contribution of this thesis is physical simulation of the extended interfacial zone generated during injection of a lower-viscosity and different density fluid into a reservoir that is saturated and wet with another fluid. An example of an application of the new analytical and semi-analytical formulations is the injection of supercritical CO_2 into a water-wet tabular reservoir to achieve sequestration.

The analytical solutions presented in Chapters 3 to 5 relax the sharp interface assumption that has been a major restrictive assumption in most analytical works. A sharp interface is only valid when the capillary force is small, and that assumption simplifies the problem of primary drainage, but greatly restricts the applicability of such solutions. Drainage progression can be driven by injection, natural flow or gravity segregation in dipping geometries. In this thesis, only injection has been considered as the force driving lateral spreading, but the equations can be easily transformed to natural flow and gravity-driven flow cases, or a combination of driving forces.

The effect of the capillary fringe (transition zone) has been widely discussed in the literature, but adequate mathematical solutions for the extended interfacial zone have not been provided. Starting from the simplest possible relative permeability function, a linear assumption, the size of the transition zone was calculated in Chapters 3 and 4. However, a linear relative permeability function is a poor description of porous media, and is only valid when the capillary forces are small enough to be neglected (e.g. coarse-grained or fractured material), but it provides interesting possibilities for intuitive analytical solutions. Linear relative permeability assumptions have been used to demonstrate the qualitative interfacial interaction during drainage and imbibition (see(41)). Chapter 3 proposes two different methods for estimation of the position and nature of the transition zone, allowing its size to be calculated. It is shown that large capillary numbers lead to a larger transition zone.

Moreover, the size of the capillary zone grows in time and has a direct relation with the ratio of mobilities (or ratio of the viscosities) of the two fluids.

The effect of non-linear relative permeabilities has been widely neglected in the literature that deals with analytical or semi-analytical flow equations. Not only are most of the analytical solutions based on the sharp interface assumption, the few that attempt to incorporate the capillary fringe effect do not correctly incorporate realistic relative permeability functions. For instance in (58), the existence of a significant capillary force is considered equivalent to the diffused interface (continuous interface). In Chapter 4 (Eq (4.26)) and Chapter 5 (lemma 1) it has been proven (and verified numerically - Fig (5.1)) that even in the presence of large capillary forces appropriate relative permeability functions can provide a sharp interface.

Chapter 4 proposes a generalized conservation equation, and the classic Buckley-Leverett equation for gravity-free 1D, cylindrical or spherical geometries are special cases of Eq (4.26) when the shape of isosats are considered to be flat surface, cylinders or spheres respectively.

Chapter 5 proposes two different methods for prediction of the interface position and the average saturation in the case of nonlinear relative permeabilities and an arbitrary Leverett-J function. The first analytical solution is an extension of existing one by Nordbotten and Dahle (58) and Golding et al. (60), but with the introduction of non-linear relative permeabilities. Analytical integration is time consuming and it is only possible when the degrees of nonlinearity (a in Eq (5.12)) are expressed with an integer (2, 3…). In most relative permeability functions calibrated from samples, the degree of nonlinearity is not expressed with an integer. For instance in (82), the degree of nonlinearity (exponent a) would be equal to 2.7 if the parameters in Eq (5.12) are determined from the published data. It is apparent that the analytical solution is not easily adaptable with non-integral degrees of

nonlinearity. Another semi-analytical solution is also presented in Chapter 5 that incorporates a variety of Leverett-J functions and degrees of nonlinearity including non-integer values for exponent a.

Chapter 5 also presents an upscaled fractional flow function for the extended interface, gravity drainage problem. By using this new fractional flow function, it becomes possible to model secondary imbibition, secondary drainage, and so on, opening the possibility for semi-analytical modeling of injection processes that involve cyclic fluid injection, such as CO_2 injection for a month, followed by water injection for three months, and so on. Alternating fluid injection technologies already are used (water-alternating-gas), and such approaches hold promise for optimization of secure CO_2 sequestration approaches that enhance dissolution into the aqueous phase and residual trapping.

It should be emphasized that the new developments herein, which greatly extend the range of analytical and semi-analytical solutions in the class of problems related to injection of immiscible fluids of different density, are widely applicable to technologies such as enhanced oil recovery by gravity drainage, gas, solvent or water injection, air sparging for cleaning contaminated aquifers, and so on.

6.1 Recommendations for future research:

Mathematical simulation of multiphase flow remains in a somewhat naïve state, and better understanding of the physics of fluid flow will continue to benefit from more rigorous laboratory and field studies. Some of the more interesting subjects for future research (83)(84) are identified here

Vertically dynamic injection: In most analytical and numerical analysis, the capillary gravity condition is a basic assumption. It has been widely accepted intuitively, and justified mathematically, but vertical equilibrium is only acceptable if the geometry provides a large

aspect ratio. In other words, only if the thickness of the aquifer is much smaller than its length. Vertical equilibrium is therefore only valid for specific reservoir geometry and characteristics and it remains unsuitable for more complex geometry.

Effect of mixing, dissolution and vaporization, salt precipitation: A gaseous fluid such as CO_2 is partially soluble in the aqueous phase, and the dissolution process is simultaneous with the injection process. Saline water also vaporizes, and the precipitation of salt is possible from the evaporating residual water content as CO_2 injection continues. Mass transfer from the injected gas to the saline water and and the reverse can be calculated based on equilibrium thermodynamics (85) or kinetic mass transfer (75). Mixing of gaseous or super critical phases with aqueous phases is an interesting subject for future studies; for example, direct co-injection of supercritical CO_2 and produced formation water into a reservoir is of interest to enhanced oil recovery schemes as well as to sequestration approaches.

Effect of compressibility of fluids and the poroelasticity of the granular medium: A major assumptions in this work and similar works is incompressibility of fluids and the rock, justified because of the small pressure variations that would take place during constant pressure injection of CO2. Also, a negligible temperature variation is always assumed. These assumptions are only valid for specific scenarios of injection, but for massive injection or cyclic injection, pressure and temperature variation become major issues. Pressure build-up has been widely studied (86) in a manner similar to the case of single phase immiscible injection, but the interfacial effect, the solubility effect and the geomechanical effects (stress redistribution and poroelastic effects) have not been fully incorporated in a rigorously coupled manner.

Bibliography

1. Dooley JDRDCWMGNKSME. A technology report from the second phase of the global energy technology strategy. ; 2006.

2. Wigley T. Kyoto Protocol: CO2 CH4 and climate implications. Geophysical research letters. 1998.

3. Samuel CM, Ronny P, Zuo L, Benson SM. Relative permeability and trapping of CO2 and water in sandstone rocks at reservoir conditions. 2012; 48(2532).

4. Hassanzadeh HPDMKW. Scaling behavior of convective Mixing, with application to geological storage of CO2. AlChe Journal. 2007;: p. 1121-1131.

5. Riaz AHMTAOJ. Onset of convection in a gravitationally unstable, diffusive boundary layer in porous media. Journal of fluid mechanics. 2006;: p. 87-111.

6. Ennis-King JPL. Role of convective mixing in the long-term storage of carbon dioxide in deep saline formations. Society of Petroleum Energy. 2005;: p. 326-334.

7. Benson SCD. CO2 sequestration in deep sedimentary formations. Elements 4.5. 2008;: p. 325-331.

8. Firoozabadi A. Thermodynamics of Hydrocarbon Reservoir: McGraw Hill; 1999.

9. Hassanzadeh HPDMKW. The Effect of Natural Flow of Aquifers and associated dispersion on the onset of buoyancy-driven convection in a standard porous media. AlChe Journal. 2009;: p. 475-485.

10. Robinson SBLJA. Prediction of the natural convective heat transfer from a horizontal heated disk. Journal of heat transfer. 1987;: p. 269-279.

11. Li SDMLZHHQHNESLMDZLSHHQEN. Gas breakthrough pressure for hydrocarbon reservoir seal rocks: implications for the security of long-term CO2 storage in the Weyburn field Geofluids. Geofluids. 2005;: p. 326-334.

12. Haywood HEJSH. Carbon dioxide sequestration as stable carbonate minerals – environmental barriers. Environmental geology. 2004;: p. 11-16.

13. Bachu SGWDPEH. Aquifer disposal of CO2: hydrodynamic and mineral trapping. Energy Conversion Management. 1994;: p. 269-279.

14. Gunter WWBPE. Aquifer disposal of CO2-rich greenhouse gases: Extension of the time scale of experiment for CO2-sequestering reactions by geochemical modeling. Mineral Petroleum. 1997;: p. 121-140.

15. Crossley N. Conversion of LPG salt caverns to natural gas storage "A Transgas experience". Journal of Canadian petroleum technology. 1998.

16. Johnston PSDSR. Ocean Disposal/Sequestration of Carbon Dioxide from fossil fuel production and use: an overview of rationale, Techniques and implications. ; 1999.

17. Yang DUNST. Automaton Simulations of Dispersion in Porous Media. Transport in porous media. 2004;: p. 187-198.

18. Sanchez-Palencia E. Homogenization in mechanics, a survey of solved and open problems; 1974.

19. Lee CSCMC. Computation of permeability and dispersivities of solute and heat in periodic porous media. International journal of heat and mass transfer. 1996;: p. 661-676.

20. Zijil WTA. Numerical homogenization of two-phase flow in porous media. Computational geoscience. 2002;: p. 49-71.

21. Barenblatt IG, Entov VM, Ryzhik VM. Theory of Fluid Flow in Natural Rock: Kluwer Academic Publisher; 1990.

22. Malekzadeh FA, Pak A. A discretized analytical solution for fully coupled non-linear simulation of heat and mass transfer in poroelastic unsaturated media. International Journal of Analytical and Numerical Methods in Geomechanics. 2009; 33(18): p. 1589-1611.

23. Brooks RH, Corey AT. Properties of porous media affecting fluid flow. Journal of the Irrigation and Drainage Division. 1966;: p. 92(IR2):61-88.

24. Plug WJ, Bruining J. Capillary pressure for the sand–CO2–water system under various pressure conditions. Application to CO2 sequestration. Advances in Water Resources. 2007;: p. 30(11):2339-2353.

25. Flett MGRTI. The function of gas–water relative permeability hysteresis in the sequestration of carbon dioxide in saline formations. In SPE Asia Pacific Oil and Gas Conference and Exhibition; 2004; Perth, Australia.

26. Groot SMP. Non-equilibrium thermodynamics Amesterdam: North Holland; 1962.

27. Stauffer FKXKW. A stochastic model for air injection into saturated porous media. Advances in water resources. 2009;: p. 1180-1186.

28. Wyllie M. Relative permeability. In Petroleum production handbook 2.; 1962. p. 25-1.

29. Wyllie MGG. The generalized Kozeny-Carman equation : Its application to problems of multiphase flow in porous media. World Oil. 1958;: p. 121-126.

30. Scheidegge A. The physics of flow through porous media: University of Toronto Press; 1962.

31. Delshad MLJOMPG. A mixed-wet hysteresis relative permeability and capillary pressure model for reservoir simulations. SPE Reservoir Evaluation and Engineering. 2003;: p. 328-334.

32. Bennion B. The Impact of Interfacial Tension and Pore Size Distribution/Capillary Pressure Character on CO2 Relative Permeability at Reservoir Conditions in CO2-Brine Systems. In SPE Conference; 2006; Tulsa, Oklahoma, USA: Society of Petroleum Engineers.

33. Settari T, Aziz K. Petroleum reservoir simulation London: Applied Science Publishers; 1979.

34. Muskar M. The flow of homogeneous fluids through porous media: Mc-Graw Hill; 1937.

35. Silin DPT. A model of Buoyancy-Driven Two-Phase Countercurrent Fluid Flow. Transport in porous media. 2008;: p. 469-489.

36. Sheldon JFF. The effect of capillary pressure and the gravity on two-phase fluid flow in a porous medium. Transport in porous media. 1959.

37. Buckley SE, Leverett MC. Mechanism of fluid displacement in sands. Trans. AIME. 1942.

38. Ryzhik V. On capillary imbibibtion by water of an oil-saturated reservoir. Soviet academic Izvestia mechanics gas fluid. 1960.

39. Nordabotten JM, Celia MA, Bachu A. Injection and storage of CO2 in deep saline aquifers. Transport in porous media. 2005;: p. 58:339-360.

40. Lake LW. Recovery, Enhanced Oil New Jersey: Prentice Hall Inc.; 1989.

41. Barenblatt G I EVMRVM. Theory of Fluid Flow in Natural Rock: Kluwer Academic Publisher; 1990.

42. Marley MHDWM. The Application of In Situ Air Sparging as an Innovative Soils and Ground Water Remediation Technology. Ground Water Monitoring & Remediation. 1992 May; 12(2): p. 137-145.

43. Bachu SGW. Overview of acid-gas injection operations in western Canada. In Proceedings of the 7th International Conference on Greenhouse Gas Control Technologies.; 2004.

44. Whitaker S. Flow in porous media II: The governing equations for immiscible, two-phase flow. TRANSPORT IN POROUS MEDIA. 1986;: p. Volume 1, Number 2, 105-125.

45. Doughty C, Karsten P. A Similarity Solution for Two-Phase Water, Air, and Heat Flow Near a Linear Heat Source in a Porous Medium. Journal of Geophysical Research. 1992;: p. VOL. 97, NO. B2, PP. 1821-1838.

46. Sander GC, Parlange JY, Lisle IG, Weeks SW. Exact solutions to radially symmetric two-phase flow for an arbitrary diffusivity. Advances in Water Resources. 2005;: p. Volume 28, Issue 10, 1112–1121.

47. Chen Z. Some Invariant Solutions to Two-Phase Fluid Displacement Problems Including Capillary Effect. SPE Reservoir Engineering. 1988;: p. Volume 3, Number 2, Pages 691-700.

48. Hussain FCYBP. A Semi-Analytical Model for Two Phase Immiscible Flow in Porous Media Honouring Capillary Pressure. Transport in porous media. 2012; 92: p. 187-212.

49. Nordbotten J M DHK. Impact of the capillary fringe in vertically integrated models for CO 2 storage. Water Resource Research. 2009;: p. VOL. 47, W02537, 11 PP.

50. Smoller J. Shock Waves and Reaction-Diffusion Equations New York: Springer-Verlag; 1983.

51. Yortsos YC. A theoretical analysis of vertical flow equilibrium. TRANSPORT IN POROUS MEDIA. 1995;: p. Volume 18, Number 2, 107-129.

52. Golding MNJHMHH. Two-phase gravity currents in porous media. Journal of Fluid Mechanics. 2011;: p. vol. 678, pp. 248–270.

53. Plug W J BJ. Capillary pressure for the sand–CO2–water system under various pressure conditions. Application to CO2 sequestration. Advances in Water Resources. 2007;: p. 30(11):2339-2353.

54. Hesse MTACBOF. Gravity currents in horizontal porous layers: transition from early to late selfsimilarity. Journal of fluid mechanics. 2007; 577: p. 363-383.

55. Huppert HE, Woods AW. Gravity-driven flows in porous layers. Journal of Fluid Mechanic. 1995;: p. 292:55-69.

56. Nordbotten M J CMA. Similarity solution for fluid injection into confined aquifers. Journal of Fluid Mechanic. 2006;: p. 561:307-327.

57. Juanes R MCSM. The Footprint of the CO2 Plume during Carbon Dioxide Storage in Saline Aquifers: Storage Efficiency for Capillary Trapping at the Basin Scale. Transport in Porous Media. 2009;: p. 82(1):19-30.

58. Nordbotten JDH. Impact of capillary forces on large-scale. In XVIII International Conference on Water Resources; 2010; Barcelona.

59. Lyle SHHHMBMCA. Axisymmetric gravity currents in a porous medium. Journal of fluid mechancis. 2005; 543: p. 293-302.

60. Golding MJ, Neufeld JA, Hesse MA. Two-phase gravity currents in porous media. Journal of Fluid Mechanics. 2011;: p. vol. 678, pp. 248–270.

61. Nordbotten M J CMABS. Injection and storage of CO2 in deep saline aquifers. Transport in porous media. 2005;: p. 58:339-360.

62. Gasda E S NJMCMA. Vertical equilibrium with sub-scale analytical methods for geological CO2 sequestration. Computational Geoscience. 2009;: p. Volume 13, Number 4, 469-481.

63. Gasda S E NJMCMA. Vertically averaged approaches for CO2 migration with solubility trapping. WATER RESOURCES RESEARCH. 2011;: p. VOL. 47, W05528, 14 PP.

64. Juanes R, MacMinn C, Szulczewski M. The Footprint of the CO2 Plume during Carbon Dioxide Storage in Saline Aquifers: Storage Efficiency for Capillary Trapping at the Basin Scale. Transport in Porous Media. 2009;: p. 82(1):19-30.

65. Taku SJKOF. Storage of CO2 in saline aquifers: Effects of gravity, viscous, and capillary forces on amount and timing of trapping. International journal of greenhouse gas control. 2007; 1(4): p. 481-491.

66. Moortgat JFA. Higher-Order Compositional Modeling with Fickian Diffusion in Unstructured and Anisotropic Media. Advances in Water resources. 2010; 33: p. 951-961.

67. Holden L. On the strict hyperbolicity of the Buckley-Leverett equation for three phase flow in porous media. SIAM Journal of Applied Mathematic. 1990; 50(3)(667-682).

68. Buckley S E LMC. Mechanism of fluid displacement in sands. Trans. AIME. 1942.

69. Blunt M KP. Relative permeabilities from two- and three-dimensional pore-scale network modeling. Transport in Porous Media. 2004;: p. 6(4):407-433.

70. Ghorayeb KFA. Molecular, pressure, and thermal diffusion in nonideal multicomponent mixtures. AlChe Journal. 2000;: p. 883-891.

71. Bird RSWLE. Transport phenomena: Wiley; 1960.

72. Pisani N. Multi-component gas mixture diffusion through porous media: A 1D analytical solution. International journal of heat and mass transfer. 2008;: p. 650-666.

73. Sherwood TPRWC. Mass transfer: Mc-Graw Hill; 1975.

74. Ioannidis MZW. Gas exsolution and flow during supersaturated water injection in porous media: I. Pore network modeling. Advances in Water Resources. 2011;: p. 2-14.

75. Niessner JHM. Mass and heat transfer during two-phase flow in porous meda-Theory and modeling; 2011.

76. Gasda ES, Nordbotten JM, Celia MA. Vertical equilibrium with sub-scale analytical methods for geological CO2 sequestration. Computational Geoscience. 2009;: p. Volume 13, Number 4, 469-481.

77. Blunt M, King P. Relative permeabilities from two- and three-dimensional pore-scale network modeling. Transport in Porous Media. 1991;: p. 6(4):407-433.

78. Jenkinson DS, Adams DE, Wild A. Model estimates of CO2 emissions from soil in response to

global warming. Nature. 1991;: p. 351:304-306.

79. Yin S, Dusseault MB, Rothenburg L. Thermal Reservoir Modeling in Petroleum Geomechanics. International Journal of Analytical and Numerical Methods in Geomechanics. 2009; 33(4): p. 449-485.

80. Yortsos YC. A theoretical analysis of vertical flow equilibrium. TRANSPORT IN POROUS MEDIA. 1995;: p. Volume 18, Number 2, 107-129.

81. Juanes RMC. Upscaling of capillary trapping under gravity override: Application to CO2 sequestration in aquifers. In SPE/DOE Symposium on Improved Oil Recovery, (SPE 113496); 2008; Tulsa, OK.

82. Bennion BBS. Relative permeability charactristics for super critical CO2 displacing water in variety of potential sequestration zone in western Canada sedimentary basin. In ; 2005; Dalas, Texas: Society of Petroleum Engineering.

83. Bachu SAJMKBB. Acid gas injection in the Alberta basin. In 2nd Annual conference of Carbon Dioxide Sequestration ; 2003; Alexandria, VA.

84. Bachu SNJCM. Evaluation of the spread of acid gas plumes in deep saline aquifers in western Canada as an analogue to CO2 injection in contenental sedimentary basin. In 7th International conference of greem house gas technology, vol1; peer reviewed and plenary presentations, IEA. Greenhouse Program ; 2004; Cheltenham, UK.

85. Orr F. Theory of gas injection process: Tie-Line Publications; 2007.

86. Leonenko YKDPDMHH. Accelerating the dissolution of CO2 in aquifer. In International conference on gravitational gas control technologies; 2006; Trondheim, Norway.

87. Chen Z, Haun G. Computational methods for multiphase flows in porous media London: SIAM; 2006.

88. Pruess K SN. ECO2N – A fluid property module for the TOUGH2 code for studies of CO2 storage in saline aquifers. Energy Conversion and Management. 2007;: p. 48(6):1761-1767.

89. Smith JVNHAM. Chemical Engineering Thermodynamics: Mc-Graw Hill; 2004.

90. Juanes RBM. Analytical solutions to multiphase first-contact miscible models with viscous fingering. Transport in porous medua. 2006;: p. 339-373.

91. Bachu S. Sequestration of CO2 in geological media: criteria and approach for site selection in response to climate change. Energy conversion and management. 2000;: p. 953-970.

92. Young LSR. A generalized compositional approach for reservoir simulation. SPE Journal. 1983;: p. 727-742.

93. Haugen KFR. Composition at the interface between multicomponent nonequilibrium fluid phases. Journal of chemical physics. 2009.

94. Brooks AN, Hughes JRT. Streamline upwindin/Petrov-Galerkin formulations for convection dominated flows with particular emohasis on the incompressible Navier-Stokes equations. Computer methods in applied mechanics and engineering. 1982; 32: p. 199-259.

95. Dafermos CM. Hyperbolic Conservation Laws in Continuum Physics Berlin: Springer; 2000.

96. Riaz ATH. Dynamics of vertical displacement in porous media associated with CO2 sequestration. In SPE Journal ; 2008: SPE. p. 305-311.

97. Kaviany M. Principles of Heat Transfer in Porous Media: Springer; 1999.

98. Malekzadeh F A DMB. A solution for the transition zone isosats in two-phase primary drainage in the presence of gravity. Computational in Geoscience. 2012.

99. Malekzadeh FADMB. Saturation distribution during primary drainage of a water-wet formation. Submitted in International Journal of Greenhouse Gas Control. 2012.

Appendix A:

In order to develop a numerical tool to verify the results of the analytical solution, a standard finite element method is applied. The need for a new numerical tool arose because of startling differences noted among various commercial and research numerical models. In conventional reservoir simulators, changing the properties of the component is not trivial and the source code is generally inaccessible. The assumption of incompressibility of the two fluids also has a significant effect on the results, and this assumption should be incorporated into the bench mark numerical model. Finally, the mechanical properties of the fluids should be independent of the composition and the ambient temperature to make the analytical solution and numerical model consistent. Hence, a decision was made to develop a finite element model using an IMPES scheme to give more relevant numerical results. (33)

The numerical scheme is straightforward; detailed descriptions of the method are available in many text books(33) (87). An up-stream weighting scheme is used as it provides reasonable stability to the convective equation. The governing equations are a set of two parabolic non-linear equations, and the unknown vector of the set of equations consists of the heads of the two phases of different density.

$$\bar{u}_w = -\lambda_w \nabla P - \lambda_w \gamma_w \bar{e}_z \qquad A1$$

$$\bar{u}_n = -\lambda_n \left(\nabla P + \nabla P_c\right) - \lambda_n \gamma_n \bar{e}_z \qquad A2$$

Eqs (A1) and (A2) are constitutive equations, and, by introducing the mass conservation equations

$$\nabla . \bar{u}_n = \frac{\partial\left(\varphi(1-S)\right)}{\partial t} + q_n \delta(r - r_o, z - z_o) \qquad A3$$

$$\nabla . \bar{u}_w = \frac{\partial\left(\varphi S\right)}{\partial t} + q_w \delta(r - r_o, z - z_o) \qquad A4$$

Here, q_w and q_n are the rate of injection or production from the point sources, δ is the delta Dirac function and (r_o,z_o) is the position of the point sources. The last equation presented is another constitutive equation.

$$P_c = j(S) \qquad A5$$

Eqs (A3) to (A4) are the governing equations for immiscible and incompressible fluids. By introducing heads for wetting and non-wetting fluids as

$$h_{w/n} = P_{w/n} + \gamma_{w/n} z \qquad A6$$

the set of equations is transformed to

$$\nabla.(-\lambda_w \nabla h_w) = \varphi \frac{\partial S}{\partial t} + q_w \delta(r - r_o, z - z_o) \qquad A7$$

$$\nabla.(-\lambda_w \nabla h_w - \lambda_n \nabla h_n) = q_w \delta(r - r_o, z - z_o) + q_n \delta(r - r_o, z - z_o) \qquad A8$$

Relative permeability functions and Leverett-J functions are the constitutive relationships, by setting the trial function and interpolation functions as a linear isoparametric shape function for triangular elements, the set of governing equations is transformed to

$$\begin{cases} \left(\overline{\overline{K}}_w^n + \overline{\overline{K}}_n^n\right)\overline{P}^n + \left(\overline{\overline{K}}_w^n \gamma_w + \overline{\overline{K}}_n^n \gamma_n\right)\overline{Z} = \overline{q}_w^n + \overline{q}_n^n & A9 \\ \overline{\overline{K}}_w^n \overline{P}^n + \overline{\overline{K}}_w^n \gamma_w = \overline{\overline{M}} \dfrac{\left(S^{n+1} - S^n\right)}{\Delta t} + \overline{q}_w^n & A10 \end{cases}$$

K and M are stiffness and mass tensors, and q is the source vector. Using finite element discretization, the tensors are defined as

$$\overline{\overline{K}}^{n}_{w/n} = -\int_{\Omega_e} \nabla \varpi \lambda^{n}_{w/n} . \nabla \varpi^{T} d\Omega_e \qquad A11$$

$$\overline{\overline{M}}_{w/n} = \int_{\Omega_e} \varpi \otimes \varpi^{T} d\Omega_e \qquad A12$$

$$\overline{q}^{n}_{w/n} = \frac{1}{3} Q_{w/n} [111]^{T} \delta(r - r_o, z - z_o) \qquad A13$$

$Q_{w/n}$ is the rate of source and sink, and $\otimes$ is the symbol of dyadic multiplication. It is apparent that the nature of the saturation equation is dominantly convective, and to restore the stability of the results, a localized up-stream scheme is applied. Assuming the mobility tensors are positive definite and there are no off-diagonal components of the mobility tensor, and also assuming that the heterogeneity of the formation is coaxial with horizontal and vertical directions, one can write the mobility tensor in the local coordinate system as

$$\lambda_{w/n} = \begin{bmatrix} \lambda^{r}_{w/n} & 0 \\ 0 & \lambda^{z}_{w/n} \end{bmatrix} \qquad A14$$

When

$$\begin{cases} \lambda^{r}_{w/n} = \lambda^{r}_{w/n}(\max(S_1, S_2)) \\ \lambda^{r}_{w/n} = \lambda^{r}_{w/n}(\max(S_1, S_3)) \end{cases} \qquad A15$$

Fig (A1): Typical triangular element in the local coordinate system

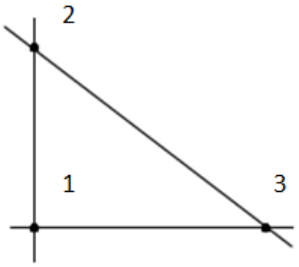

The same scheme is adaptable for 1D and axisymmetric geometries. Despite the fully implicit scheme, the IMPES method is conditionally stable, but the time step size should be smaller than a particular limit(87). This constraint makes the

method slower, but in an IMPES scheme the set of algebraic equation is linear after numerical discretization.